



# **NAVAL POSTGRADUATE SCHOOL**

**MONTEREY, CALIFORNIA**

## **THESIS**

**ENVIRONMENTAL IMPACT ON THE NORTHERN  
PERSIAN GULF: A MINE DRIFT AND CHEMICAL SPILL  
STUDY CENTERED ON IRAQ'S OIL TERMINALS USING  
NAVY'S OCEAN-ATMOSPHERIC PHYSICAL AND  
CHEMICAL MODELS**

by

Charles L. Williams

March 2007

Thesis Advisor:  
Second Reader:

Peter C. Chu  
Steven D. Haeger

Approved for public release; distribution is unlimited.

THIS PAGE INTENTIONALLY LEFT BLANK

<b>REPORT DOCUMENTATION PAGE</b>			<i>Form Approved OMB No. 0704-0188</i>	
Public reporting burden for this collection of information is estimated to average 1 hour per response, including the time for reviewing instruction, searching existing data sources, gathering and maintaining the data needed, and completing and reviewing the collection of information. Send comments regarding this burden estimate or any other aspect of this collection of information, including suggestions for reducing this burden, to Washington headquarters Services, Directorate for Information Operations and Reports, 1215 Jefferson Davis Highway, Suite 1204, Arlington, VA 22202-4302, and to the Office of Management and Budget, Paperwork Reduction Project (0704-0188) Washington DC 20503.				
<b>1. AGENCY USE ONLY (Leave blank)</b>		<b>2. REPORT DATE</b> March 2007	<b>3. REPORT TYPE AND DATES COVERED</b> Master's Thesis	
<b>4. TITLE AND SUBTITLE</b> Environmental Impact on the Northern Persian Gulf: A Mine Drift and Chemical Spill Study Centered on Iraq's Oil Terminals using Navy's Ocean-Atmospheric Physical and Chemical Models			<b>5. FUNDING NUMBERS</b>	
<b>6. AUTHOR(S)</b> Williams, Charles L.				
<b>7. PERFORMING ORGANIZATION NAME(S) AND ADDRESS(ES)</b> Naval Postgraduate School Monterey, CA 93943-5000			<b>8. PERFORMING ORGANIZATION REPORT NUMBER</b>	
<b>9. SPONSORING /MONITORING AGENCY NAME(S) AND ADDRESS(ES)</b> N/A			<b>10. SPONSORING/MONITORING AGENCY REPORT NUMBER</b>	
<b>11. SUPPLEMENTARY NOTES</b> The views expressed in this thesis are those of the author and do not reflect the official policy or position of the Department of Defense or the U.S. Government.				
<b>12a. DISTRIBUTION / AVAILABILITY STATEMENT</b> Approved for public release: distribution is unlimited.			<b>12b. DISTRIBUTION CODE</b> A	
<b>13. ABSTRACT (maximum 200 words)</b> <p>An attack on, or chemical spill near, Iraq's Oil Terminals could have disastrous effects on Iraq's economy. The impacts from a drifting mine or chemical spill are highly dependent upon environmental conditions that can either adversely effect continued operations or hinder the safety of personnel. Operational Planners ability to create legitimate scenarios to train and combat these situations is key to continued safe operation of the terminals.</p> <p>To accomplish this, planners must understand the impacts of using climatology versus near real-time data in the evaluation of the scenarios. The near real-time environmental data were provided by the Navy's ocean-atmospheric operational models. This study examines the benefits of knowing the environment to understand their impacts to operations in the northern Persian Gulf. Three different scenarios were examined to understand the impact to Oil Terminal operations in the event of drifting mines or a chemical spill. The chemical spill was examined from the outlook of a major collision with a barge that spilled either Liquefied Ammonia or Mustard Gas. The Ammonia scenario was further analyzed in the atmosphere. This study demonstrates the impact that near real-time environmental conditions can have over climatological data for Operational Planners.</p>				
<b>14. SUBJECT TERMS</b> Meteorology, Oceanography, SWAFS, currents, COMAPS, surface winds, Mine Warfare, Chemical Spill, Ammonia, Mustard Gas, CHEMMAP™, HPAC, Prediction, Chemical Propagation, Empirical Orthogonal Function (EOF), complex EOF, Iraq, Oil Terminal			<b>15. NUMBER OF PAGES</b> 146	
			<b>16. PRICE CODE</b>	
<b>17. SECURITY CLASSIFICATION OF REPORT</b> Unclassified	<b>18. SECURITY CLASSIFICATION OF THIS PAGE</b> Unclassified	<b>19. SECURITY CLASSIFICATION OF ABSTRACT</b> Unclassified	<b>20. LIMITATION OF ABSTRACT</b> UL	

THIS PAGE INTENTIONALLY LEFT BLANK

**Approved for public release; distribution is unlimited**

**ENVIRONMENTAL IMPACT ON THE NORTHERN PERSIAN GULF: A MINE  
DRIFT AND CHEMICAL SPILL STUDY CENTERED ON IRAQ'S OIL  
TERMINALS USING NAVY'S OCEAN-ATMOSPHERIC PHYSICAL AND  
CHEMICAL MODELS**

Charles L. Williams  
Lieutenant, United States Navy  
B.S., University of Washington, 1999

Submitted in partial fulfillment of the  
requirements for the degree of

**MASTER OF SCIENCE IN METEOROLOGY AND PHYSICAL  
OCEANOGRAPHY**

from the

**NAVAL POSTGRADUATE SCHOOL  
March 2007**

Author: Charles L. Williams

Approved by: Peter C. Chu  
Thesis Advisor

Steven D. Haeger  
Second Reader

Mary L. Batteen  
Chairman, Department of Oceanography

THIS PAGE INTENTIONALLY LEFT BLANK

## **ABSTRACT**

An attack on, or chemical spill near, Iraq's oil terminals could have disastrous effects on Iraq's economy. The impacts from a drifting mine or chemical spill are highly dependent upon environmental conditions that can either adversely effect continued operations or hinder the safety of personnel. Operational Planners' ability to create legitimate scenarios to train and combat these situations is key to continued safe operation of the terminals.

To accomplish this, planners must understand the impacts of using climatology versus near real-time data in the evaluation of the scenarios. The near real-time environmental data were provided by the Navy's ocean-atmospheric operational models. This study examines the benefits of knowing the environment to understand their impacts to operations in the northern Persian Gulf. Three different scenarios were examined to understand the impact to Oil Terminal operations in the event of drifting mines or a chemical spill. The chemical spill was examined from the outlook of a major collision with a barge that spilled either Liquefied Ammonia or Mustard Gas. The Ammonia scenario was further analyzed in the atmosphere. This study demonstrates the impact that near real-time environmental conditions can have over climatological data for Operational Planners.

THIS PAGE INTENTIONALLY LEFT BLANK



# TABLE OF CONTENTS

<b>I.</b>	<b>INTRODUCTION: THE PERSIAN GULF .....</b>	<b>1</b>
A.	OVERVIEW .....	1
B.	ECONOMIC AND POLITICAL CONCERNS .....	3
C.	SCENARIO SELECTION CONCEPT .....	5
<b>II.</b>	<b>ENVIRONMENTAL FACTORS FROM PREVIOUS STUDIES .....</b>	<b>9</b>
A.	CURRENTS.....	9
B.	WINDS .....	10
C.	TIDES.....	13
D.	CURRENTS: TIDAL, WIND-DRIVEN, AND DENSITY DRIVEN.....	14
E.	MIXING PROCESSES AND VERTICAL STRUCTURE.....	15
<b>III.</b>	<b>OCEAN-ATMOSPHERIC PHYSICAL-CHEMICAL MODELS.....</b>	<b>17</b>
A.	COAMPS .....	17
B.	SWAFS.....	22
C.	HPAC AND SECOND-ORDER CLOSURE INTEGRATED PUFF (SCIPUFF) .....	28
1.	Gaussian Moment Definition .....	30
2.	Moment Transport Equations .....	31
3.	Turbulence Closure Diffusion Model.....	31
4.	Concentration Fluctuation Variance.....	33
5.	Numerical Techniques .....	34
6.	Meteorology Specification .....	36
D.	CHEMMAP™ .....	37
1.	CHEMMAP™ Chemical Database.....	37
2.	Chemical Fates Model .....	38
3.	Environmental Data.....	40
4.	Stochastic Model .....	40
<b>IV.</b>	<b>MATHEMATICAL AND STATISTICAL ANALYSIS .....</b>	<b>43</b>
A.	BASIC MATHEMATICS AND STATISTICS .....	43
B.	CONVENTIONAL EOF ANALYSIS .....	45
C.	COMPLEX EOF ANALYSIS.....	47
<b>V.</b>	<b>MINE WARFARE (MIW) .....</b>	<b>49</b>
<b>VI.</b>	<b>CHEMICAL POLLUTANTS .....</b>	<b>51</b>
A.	AMMONIA.....	51
B.	SULFUR MUSTARD / MUSTARD GAS.....	52
<b>VII.</b>	<b>ANALYSIS OF PHYSICAL MODEL OUTPUT .....</b>	<b>55</b>
A.	PHYSICAL MODEL OUTPUT .....	55
1.	Currents .....	55
2.	Winds .....	55
B.	DATA PROCESSING .....	56
C.	WINDS .....	59

1.	Monthly Mean .....	59
2.	Anomalies.....	64
3.	Spatial Examining Raw Data.....	69
D.	CURRENTS FOR THE NORTHERN GULF .....	70
3.	Spatial Examining Raw Data.....	80
E.	EXTRACTING TIMES FOR CHEMICAL MODEL RUNS.....	81
VIII.	CONNECTION BETWEEN PHYSICAL AND CHEMICAL MODELS.....	83
IX.	MIW: IMPACT OF DRIFTING MINES ON OIL PLATFORM OPERATIONS .....	87
A.	CLIMATOLOGICAL .....	89
B.	SCENARIO SPECIFIC.....	91
X.	IMPACT OF A CHEMICAL SPILL TO OPERATIONS: AMMONIA .....	97
A.	ATMOSPHERIC PORTION OF SCENARIO .....	97
1.	Climatological.....	97
2.	Specific Scenario .....	99
B.	OCEANOGRAPHIC PORTION OF SCENARIO.....	101
1.	Climatological Input .....	101
2.	Specific Scenario .....	102
XI.	IMPACT OF A CHEMICAL SPILL TO OPERATIONS: MUSTARD GAS...	105
XII.	SUMMARY .....	109
	APPENDIX.....	113
	LIST OF REFERENCES.....	119
	INITIAL DISTRIBUTION LIST .....	127

## LIST OF FIGURES

Figure 1.	General Topography of region surrounding the Persian (Arabian) Gulf (in meters).....	1
Figure 2.	General Bathymetry of the Persian (Arabian) Gulf (depth is in meters). ....	2
Figure 3.	Plot of Iraqi Oil Terminals ABOT, five –pointed white star, and KAAOT, six-pointed yellow star (depth is in meters). ....	4
Figure 4.	Three Tiers of Battlespace on Demand (From Capt. Dave Titley, USN, 2007). ....	7
Figure 5.	Sketch of surface currents and circulation processes in the Persian Gulf and western Gulf of Oman (From Reynolds, 1993). ....	9
Figure 6.	Frequency of the hourly wind direction and calms (in center) observed at Kuwait International Airport (K) in 2002: (a) January; (b) April; (c) July; (d) October (After Zhu and Atkinson, 2004). ....	11
Figure 7.	Climatological summary of winds at Kuwait International airport. Scale on the right is for peak winds and range between 30 and 70 knots (From AFCCC <a href="https://notus2.afccc.af.mil/SCISPublic/">https://notus2.afccc.af.mil/SCISPublic/</a> , 2007). ....	12
Figure 8.	The $M_2$ , $S_2$ , and $K_1$ tidal constituents in the Gulf (After: Reynolds., 1993). Tide heights are shown in meters. ....	14
Figure 9.	Diagram of Arakawa scheme C (From: Comet Module <a href="http://www.comet.ucar.edu/">http://www.comet.ucar.edu/</a> , 2007). ....	19
Figure 10.	The sigma coordinate system. (From: Mellor, 2004) ....	23
Figure 11.	SWAFS model run cycle. (From: Haeger, S.D., 2006) ....	27
Figure 12.	Time Series of EOF Coefficients for the currents of the Northern Persian Gulf on a semi-log y scale. ....	58
Figure 13.	Mean wind vectors of the entire dataset (Feb – Jul). ....	60
Figure 14.	Mean monthly wind vectors. ....	63
Figure 15.	EOF-1 for entire wind dataset in the Northern Persian Gulf. ....	66
Figure 16.	EOF-1 amplitude (top) and direction (bottom) for entire wind dataset in the Northern Persian Gulf. ....	66
Figure 17.	EOF-2 for entire wind dataset in the Northern Persian Gulf. ....	67
Figure 18.	EOF-2 amplitude (top) and direction (bottom) for entire wind dataset in the Northern Persian Gulf. ....	67
Figure 19.	EOF-3 for entire wind dataset in the Northern Persian Gulf. ....	68
Figure 20.	EOF-3 amplitude (top) and direction (bottom) for entire wind dataset in the Northern Persian Gulf. ....	68
Figure 21.	Time Series of the Magnitude of Winds (in m/s). The red line corresponds to maximum value for the definition of weak winds, while the blue line corresponds to the minimum value for strong winds, in this thesis. ....	69
Figure 22.	Mean current vectors of the entire dataset (Feb – Jul) Arrow shows a 10 cm/s current. ....	71
Figure 23.	Mean monthly current vectors. ....	73
Figure 24.	EOF-1 for entire currents dataset in the Northern Persian Gulf. ....	77

Figure 25.	EOF-1 amplitude (top) and direction (bottom) for entire currents dataset in the Northern Persian Gulf. ....	77
Figure 26.	EOF-2 for entire currents dataset in the Northern Persian Gulf. ....	78
Figure 27.	EOF-2 amplitude (top) and direction (bottom) for entire currents dataset in the Northern Persian Gulf. ....	78
Figure 28.	EOF-3 for entire currents dataset in the Northern Persian Gulf. ....	79
Figure 29.	EOF-3 amplitude (top) and direction (bottom) for entire currents dataset in the Northern Persian Gulf. ....	79
Figure 30.	Time Series of the Magnitude of Currents (in cm/s). The red line corresponds to maximum value for the definition of low currents, while the blue line corresponds to the minimum value for high currents, in this thesis. ....	81
Figure 31.	Comparison of Wind and Currents fields from 14 May at 12Z. ....	82
Figure 32.	Drop-off points utilized during the drift mine scenario model runs. White X's mark mine drop locations, while the two stars represent oil terminal locations. ....	88
Figure 33.	Drifting mine scenario with release from a) climatology and three different release locations (b, c, and d). ....	89
Figure 34.	Results from the climatological MIW scenario, which included cyclic currents and climatological winds over a 5 day period. The panels are for a) initialization, b) day 2, c) day 4 and d) day 5. ....	90
Figure 35.	Results from the drifting mine scenario during a weak current and minimal winds event in February 2006. The panels depict elapsed time of a) 2 days, b) 3 days, c) 4 days and d) 5 days. Pink dots are the current location of the mines, while the black dots illustrate track history. ....	92
Figure 36.	Results from the drifting mine scenario during a weak current and maximum winds event in April 2006. The panels depict elapsed time of a) 1 day, b) 3 days, c) 4 days and d) 5 days. ....	93
Figure 37.	Results from the drifting mine scenario during a weak current and maximum winds event in July 2006. The panels depict elapsed time of a) 1 day, b) 3 days, c) 4 days and d) 5 days. ....	94
Figure 38.	Results from the drifting mine scenario during a strong oscillating current and maximum winds event in June 2006. The panels depict elapsed time of a) 2 days, b) 3 days, c) 4 days and d) 5 days. ....	95
Figure 39.	The upper portion depicts a) 50 minutes and b) 15 hours elapsed of 514 tons of Ammonia for the integrate concentration. The lower portion indicates c) 50 minutes and d) 18 hours elapsed for the duration of Ammonia in the atmosphere. ....	99
Figure 40.	Trajectory of 514 tons of Ammonia at elapsed times of a) 6 hours and b) 15 hours during an onshore winds scenario in March 2006. ....	100
Figure 41.	Trajectory of 514 tons of Ammonia at elapsed times of a) 6 hours, b) 12 hours, c) 18 hours and d) 24 hours during an offshore winds scenario in May 2006. ....	101
Figure 42.	Two panel view depicting a) 24 hours and b) 72 hours elapsed time of Ammonia with climatological forcing. ....	102

Figure 43.	12 hour mass balance graph of Liquefied Ammonia gas within CHEMMAP™.....	103
Figure 44.	Four panel view depicting a) initialization, b) 72 hours elapsed during April 2006, c) 72 hours elapsed time during June 2006 and d) 72 hours elapsed time during July 2006 for the Ammonia spill scenario. The colorbar units are in $mg/m^3$ . The labels are as follows: Tan = 0.01-0.1, Yellow = 0.1-0.5, Light Green = 0.5-1.0, Green = 1-5, Light Blue = 5-10, Blue = 10-50, Light Purple = 50-100, Purple = 100-500, and Orange > 500.....	104
Figure 45.	6 hour mass balance graph of Mustard Gas at 20°C within CHEMMAP™.....	106
Figure 46.	6 hour mass balance graph of Mustard Gas at 30°C within CHEMMAP™.....	106
Figure 47.	6 hour mass balance graph of Mustard Gas at 10°C within CHEMMAP™.....	107
Figure 48.	EOF-1 for winds of the entire Persian Gulf.....	113
Figure 49.	EOF-1 amplitude (top) and direction (bottom) for entire wind dataset in the Persian Gulf.....	113
Figure 50.	EOF-2 for winds of the entire Persian Gulf.....	114
Figure 51.	EOF-2 amplitude (top) and direction (bottom) for entire wind dataset in the Persian Gulf.....	114
Figure 52.	EOF-3 for winds of the entire Persian Gulf.....	115
Figure 53.	EOF-3 amplitude (top) and direction (bottom) for entire wind dataset in the Persian Gulf.....	115
Figure 54.	EOF-1 for currents of the entire Persian Gulf. Vectors are every fourth vector of the ones calculated, which equates to every eighth point.....	116
Figure 55.	EOF-1 amplitude (top) and direction (bottom) for entire current dataset in the Persian Gulf.....	116
Figure 56.	EOF-2 for currents of the entire Persian Gulf. Vectors are every fourth vector of the ones calculated, which equates to every eighth point.....	117
Figure 57.	EOF-1 amplitude (top) and direction (bottom) for entire current dataset in the Persian Gulf.....	117
Figure 58.	EOF-3 for currents of the entire Persian Gulf. Vectors are every fourth vector of the ones calculated, which equates to every eighth point.....	118
Figure 59.	EOF-1 amplitude (top) and direction (bottom) for entire current dataset in the Persian Gulf.....	118

THIS PAGE INTENTIONALLY LEFT BLANK

## LIST OF TABLES

Table 1.	Percent of Variance for the first 5 EOF modes of Wind data.....	64
Table 2.	Percent of Variance for the first 5 EOF modes of Current data.....	74
Table 3.	Example of HPAC file header required to ingest data into HPAC from archived COAMPS fields. ....	83

THIS PAGE INTENTIONALLY LEFT BLANK



## ACKNOWLEDGMENTS

I wish to thank my parents who supported me in all my career decisions and were an inspiration to me while growing up.

I wish to thank Dr. Peter Chu from the Naval Postgraduate School and Mr. Steve Haeger from the Naval Oceanographic Office for offering me the opportunity to delve into a thesis involving both Meteorology and Oceanography. The ability to apply both to an Operational application was a major factor in choosing the thesis. I greatly appreciate the hours of personal assistance they provided me when the data analysis and modeling process presented unexpected challenges.

I would also like to thank Mr. Matt Ward from Applied Science Associates (ASA), Inc. for the outstanding training he provided on CHEMMAP<sup>TM</sup> execution. Mr. Ward had only two days to train me on the software package that normally requires two to three weeks. He was always available via email and over the phone to help resolve any issues that arose. I would also like to thank ASA for their time in assisting getting the data into CHEMMAP<sup>TM</sup>. Without that help, this project would not have been completed on time.

I would also like to thank Kyle Dedrick and the Defense Threat Reduction Agency (DTRA) for the assistance in obtaining HPAC, in learning how to operate HPAC, and in understanding how to format the data.

Lastly, I would like to thank Chen-Wu Fan for his patience and help in the numerous computer problems that came up. His expertise was instrumental in completing my thesis on time.

Funding for this research was provided by the Naval Oceanographic Office, Stennis Space Center, Mississippi.

THIS PAGE INTENTIONALLY LEFT BLANK

# I. INTRODUCTION: THE PERSIAN GULF

## A. OVERVIEW

The Persian Gulf, also known as the Arabian Gulf, is a semienclosed marginal sea connected with the Indian Ocean through the Strait of Hormuz with the major axis tending in the NW-SE direction (Figure 1). The Persian Gulf is approximately 990 km long; the maximum width is about 338 km (Chao et al., 1992). The estimated surface area and volume of the gulf are around  $239,000 \text{ km}^2$  and  $8,630 \text{ km}^3$ , respectively, which correspond to a mean depth of close to 36 m (Chao et al., 1992). The maximum depth is around 100m near the Strait of Hormuz, with the Gulf of Oman being much deeper (Figure 2). The major axis of the basin separates a relatively deeper channel near Iranian coast from the shallow Persian shelf that slopes gently towards the axis (Chao et al., 1992).

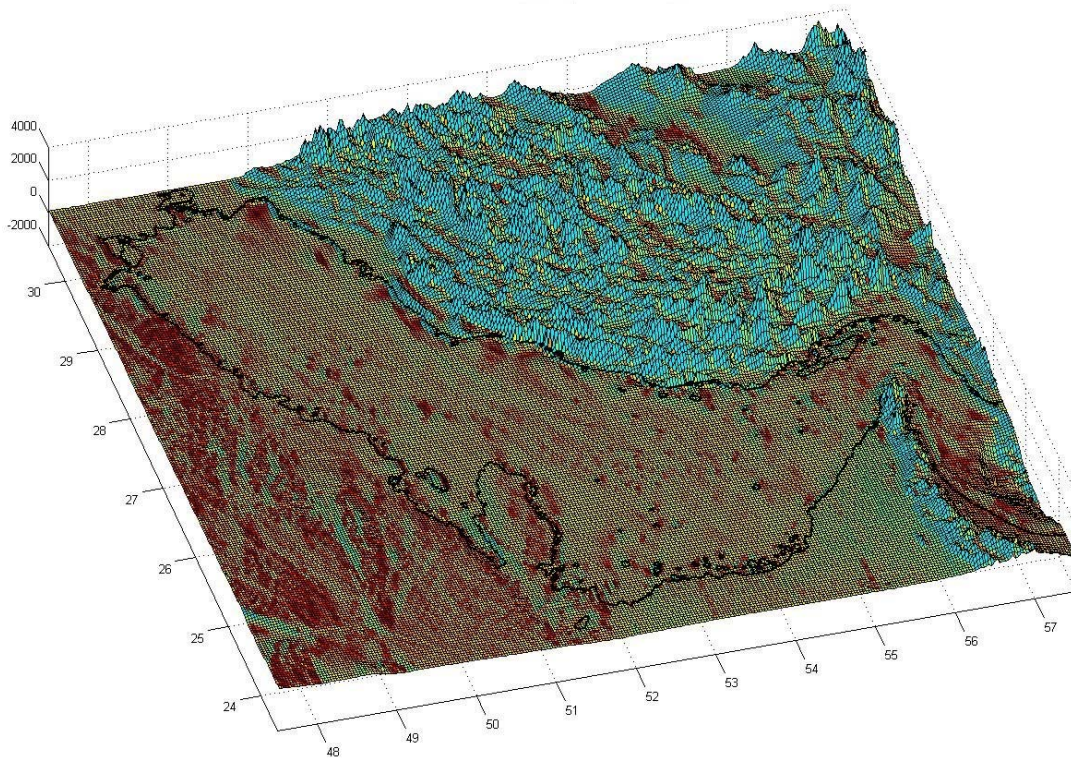


Figure 1. General Topography of region surrounding the Persian (Arabian) Gulf (in meters).

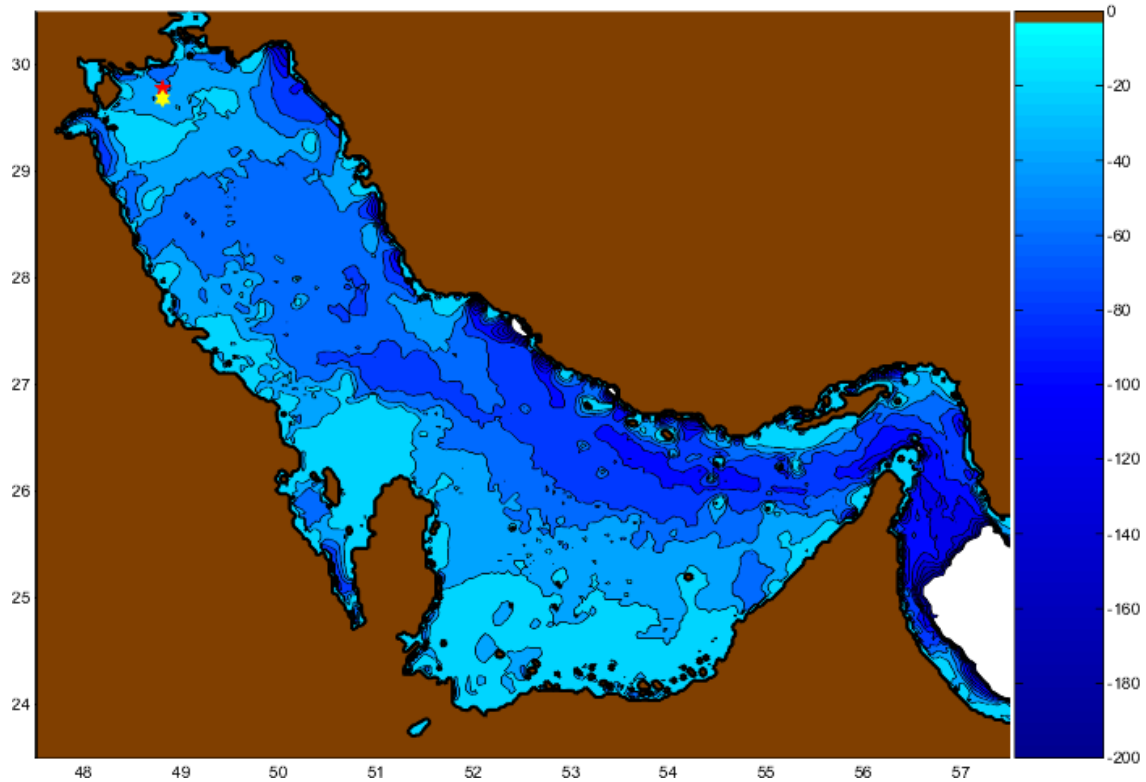


Figure 2. General Bathymetry of the Persian (Arabian) Gulf (depth is in meters).

Orographic influences on the atmospheric circulation are very significant due to the high mountains bordering much of the coastline in this region (Figure 2). The Zagros Mountains of Iran and the Jebel al Akhdar range in northern Oman play an important role in focusing the winds over the region. The Persian Gulf is characterized by northwesterly or westerly winds throughout the year (U.S. Hydrography Office, 1960). The summer winds are mild and continuous. In contrast the winds in winter are often associated with synoptic weather systems, and breaks out suddenly and violently (Reynolds, 1993).

Due to its shallow nature, the Persian Gulf appears to be influenced by winds and surface thermohaline fluxes. The persistent southward wind stress, at least in the northern half of the Gulf, appears to set up coastal current regimes along both the Saudi (downwelling) and Iranian (upwelling) coasts. A persistent thermal front across the Persian Gulf about the latitude of Qatar appears related to the thermohaline exchange through the Hormuz Strait and splits the Persian Gulf into two regimes.

The eastern or southern regime is a dynamic regime. It lies on the border between tropical and extratropical regimes and feels the influences from both. The winds and currents in the Gulf of Oman are influenced by the southwest monsoon. This influence continues through the Straights of Hormuz and into the eastern regime. The northern, or western, regime is characterized by low energy throughout. This includes both currents and winds. The winds are predominantly extratropical in nature, lying on the fringe or extratropical influences. The currents tend to be extremely low. Influences from the eastern regime occasionally reach the northern regime which increases the energy of the northern regime. Otherwise the flow remains low energy.

## **B. ECONOMIC AND POLITICAL CONCERNS**

The Persian Gulf region continues to be of paramount importance to the world community for a variety of economic and political reasons. The immense petroleum resources and their maritime export from the region and the complex evolution and conflict of competing political entities are constantly demanding attention.

There have been, and continue to be, significant territorial disputes between Persian Gulf countries. Two of the major disputes in recent history involve the Iraqi invasion of Kuwait in August 1990 and the Iran-Iraq War from 1980 to 1988. Unlike Europe, the boundaries of the countries were not derived from language or cultural influences. In some cases the boundaries were decided by countries outside the region after World War II. This compounds the problem, creating numerous religious and ethnical backgrounds within each country that do not necessarily want to coexist.

According to the Energy Information Administration *International Energy Outlook 2003* (EIA, 2003) the Persian Gulf countries produced 27% of the world oil, while holding 57% of the world's proven crude oil reserves. Besides oil, the Persian Gulf region also has huge reserves of natural gas, accounting for 45% of the total proven world gas reserves. The Energy Information Administration *International Energy Outlook 2003* predicts the Persian Gulf oil production capacity would increase to 33% of the world total by 2020.

With close to a third of the world petroleum coming from the Persian Gulf countries, the vast majority of it is exported via tanker through the Strait of Hormuz. According to Energy Information Administration *International Energy Outlook 2003* (EIA, 2003), the amount transiting through this strait was close to 90% of all oil coming from the region. Of primary importance to this study is Iraq's contribution.

Iraq's economy is dominated by the oil sector, which has traditionally provided about 95% of foreign exchange earnings. In the Persian Gulf, Iraq has three tanker terminals: Bakr Al Basrah (ABOT), Khor al-Amaya (KAAOT), and Khor az-Zubair (which mainly handle dry goods and minimal oil volumes). ABOT, formerly known as Mina al, is Iraq's largest oil terminal, with two pipelines (48-inch and 41-inch), plus four 400,000-bbl/d capacity berths capable of handling very large crude carriers (EIA, 2006). ABOT is located on the northern tip of the Persian Gulf, at approximately  $29.75^{\circ}N$   $48.83^{\circ}E$ , with KAAOT located just to the northwest, at approximately  $29.79^{\circ}N$   $48.80^{\circ}E$  (BP Port List, 2007). The locations of the oil terminals are plotted in Figure 3.

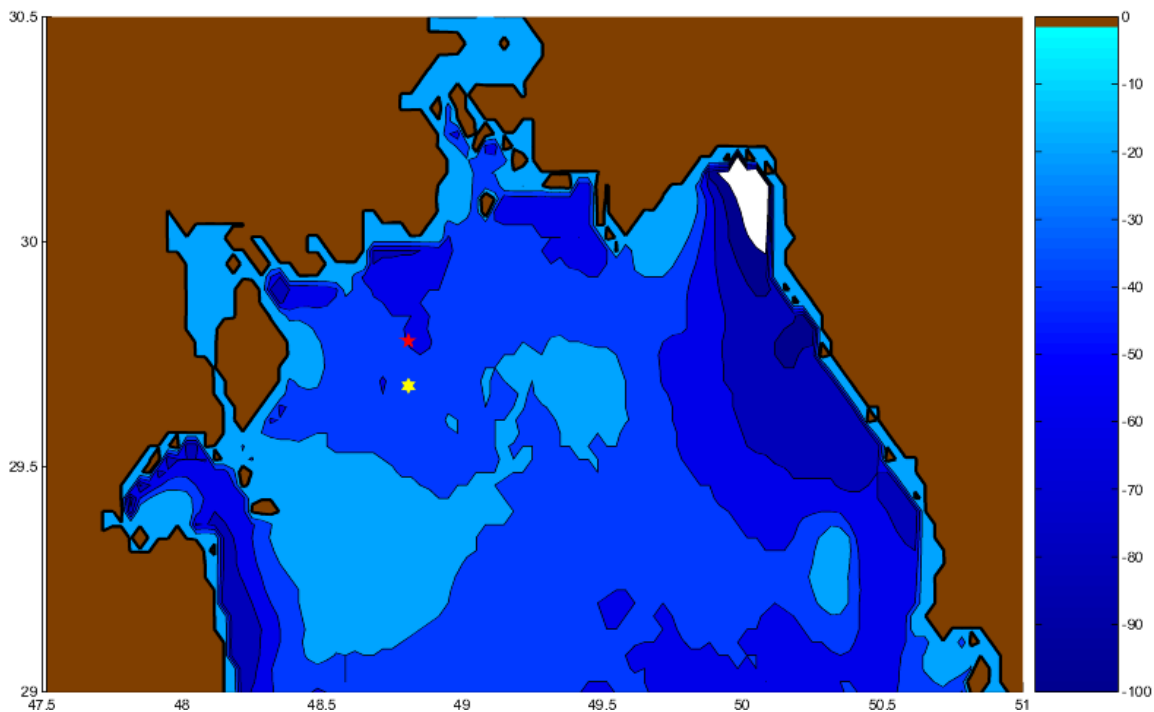


Figure 3. Plot of Iraqi Oil Terminals ABOT, five –pointed white star, and KAAOT, six-pointed yellow star (depth is in meters).

### **C. SCENARIO SELECTION CONCEPT**

The execution of any naval operation can be hindered by numerous environmental factors. Proper planning for these operations includes forecasting the environment of the area of operations. Where drifting mines or chemical spills are concerned the environment plays an important role in determining spill extent or mine avoidance/placement.

As the warfare environment continues to shift from the open ocean to littoral, environmental prediction and modeling efforts of the shallow water surroundings need to be understood and utilized in order to support these operations. The difference between climatological data and observations can be dramatic. Knowledge of the environment and the ability to predict it can determine the success of an operation in many instances. The scenarios considered in this thesis are chosen to emphasize the importance of knowing, and predicting, environmental factors to maximize the operation's success rate.

High resolution full physical models are needed to forecast the surface winds and currents. After the high-resolution winds and currents are obtained, the transport models and chemical models are utilized to forecast the mine drift and chemical spill. Two physical and two chemical models were utilized for this thesis. The two physical models, (1) the Coupled Ocean/Atmosphere Mesoscale Prediction (COAMPS), and (2) the Shallow Water Assimilation Forecast System (SWAFS), are used to get the physical environment such as the surface winds and surface currents, respectively. The outputs of the physical models are then used as inputs into the two chemical models: (1) the Hazard Prediction and Assessment Capability (HPAC) for the atmosphere and (2) CHEMMAP<sup>TM</sup> for the ocean. The outputs were then analyzed and applied to one of several possible naval operations.

Statistics and complex Empirical Orthogonal Function (EOF) analyses are used to classify the physical environment from the COAMPS and SWAFS such as the winds and currents in the Persian Gulf during the period from the beginning of February through the end of July, 2006. The purpose is to examine the extreme environmental effects on

different possible scenarios in the northern section of the Persian Gulf. The scenarios include a drift scenario and different chemical spills, either accidental or planned.

The drifting mine scenario looks at the possibility of floating mines affecting oil terminal operations. This scenario includes a generic one meter diameter mine with a density of  $1.0\text{ g/cm}^3$ . This equates to each mine weighing approximately one ton. This generic mine will then be set adrift in various spatial and temporal locations throughout the northern Persian Gulf. The scenario will also examine the ability to utilize climatology as a valid first guess.

The other portion of the study includes two different chemical spills located near the oil terminals. These scenarios will be run during times that meet certain criteria. This will in turn ensure worst case scenarios are examined. The criteria will include: (1) low winds and weak currents, (2) low winds and strong currents, (3) high winds and weak currents, (4) strong winds and strong currents, and (5) specific events such as frontal passage. These events will be compared to climatological data to determine how much value can be added over climatology.

All of these scenarios will be examined through the concept of what and how much value can be added by near real-time data versus climatological or no data. This concept is an underlying concept behind 'Battlespace on Demand'. The purpose of 'Battlespace on Demand' is to effectively supply combatant commanders with information superiority over the entire area of operation. This concept is then broken down into three tiers, which include: (1) Environment Layer, (2) Performance Layer, and (3) Decision Layer. Figure 4 illustrates the Three Tiers of Battlespace on Demand. This thesis utilized this concept in the analysis of the data with respect to the scenarios. The ability to add value by using real-time or climatological data was of interest when analyzing the scenarios.



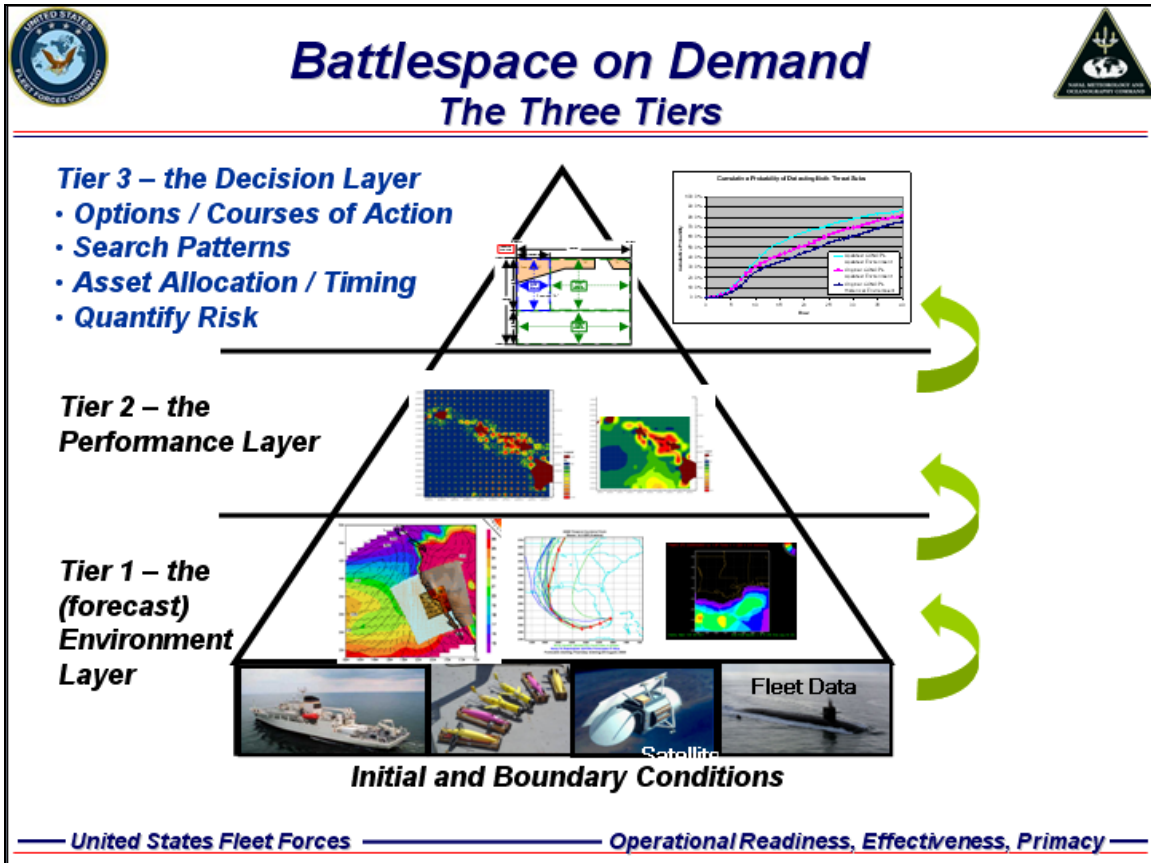


Figure 4. Three Tiers of Battlespace on Demand (From Capt. Dave Titley, USN, 2007).

THIS PAGE INTENTIONALLY LEFT BLANK

## II. ENVIRONMENTAL FACTORS FROM PREVIOUS STUDIES

### A. CURRENTS

The basic features of the Persian Gulf can be divided into a northern and southern or eastern regime (Figure 5). The primary focus of this research is the northern regime. The northern regime is dominated by wind forcing to the south along the axis of the Gulf and the riverine input at the Gulf's head. The wind-driven response of the Gulf appears to be the typical adjustment of the pressure field such as to produce a down-wind flow, i.e., there is downwelling on the western coast and upwelling on the coast of Iran, and evidence for a southeastward flowing coastal current along both the northern and southern coasts (Reynolds, 1993).

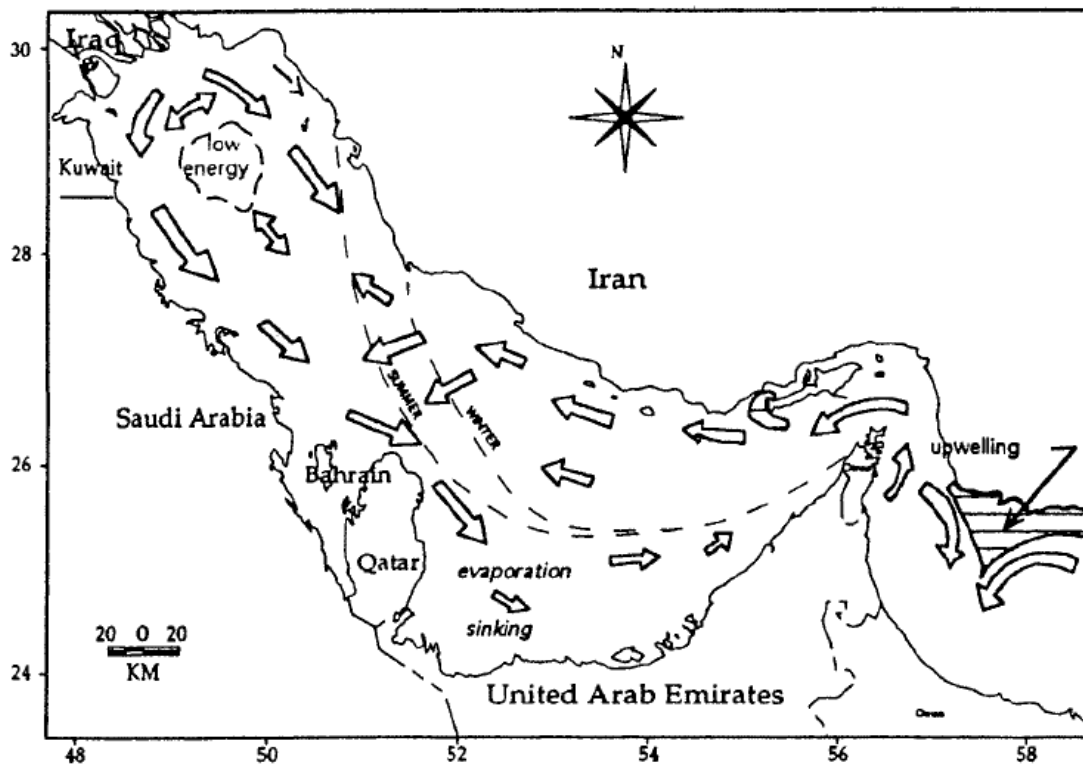


Figure 5. Sketch of surface currents and circulation processes in the Persian Gulf and western Gulf of Oman (From Reynolds, 1993).

The flow along the Kuwait and Saudi coast is augmented by the freshwater input from the north which forms a riverine plume. The river inflows are approximately split

between the flow out of the Shalat Ariabi (Tigris and Euphrates) and rivers flowing out of the highland of Iran (the Hendijan, Hilleh, and Mand). Today the flow of the Shalat Ariabi is much smaller than it once was because of massive dam projects in Turkey. It is not yet clear what changes this decline in freshwater input has made. The center of the northern Gulf appears to be fairly stagnant (Reynolds, 1993). The southern end of this regime corresponds roughly to the longitude of Qatar and Bahrain, although the termination of the northern circulation is poorly understood. The flow along the Iran coast seems to continue into the southeastern basin as a tightly trapped coastal current extending perhaps as far as the Strait of Hormuz.

The northern Persian Gulf is separated from the southern regime by a front off Qatar (Figure 5), which is most intense in summer and weakest, at least in sea surface temperature, in the late winter and spring (Reynolds, 1993). The location of this front appears in both climatological hydrographic data and remotely sensed SST to be tied to the penetration of fresh inflow into the Gulf from the Strait of Hormuz.

## **B. WINDS**

The Gulf is located between latitudes  $24^{\circ}N$  and  $30^{\circ}N$ , in which are located most of the Earth's deserts. This region marks the boundary between tropical circulations (Hadley Cell) and the synoptic weather systems of mid-latitudes. Descending dry air in these latitudes produces clear skies and arid conditions.

In the north, the local climate is influenced by orography. The Taurus and Pontic mountains of Turkey, and the Zagros Mountains of Iran together with the Tigris-Euphrates Valley, form a northwest-southeast axis that strongly influences the tracks of extra-tropical storms to a southeast direction. As part of an analysis from 1978 to 1998 of mean synoptic conditions, it was found that winds in the northern region predominantly follow the major axis of the Persian Gulf. This is clearly illustrated in Kuwait International Airport (K) portion of Figure 6 (Zhu and Atkinson, 2004). Figure 7 illustrates the same concept; however the mean and peak speeds are also shown. From Figure 7, the climatological mean can be seen to vary from 10 to 15 knots, or around 5 to 8 m/s.

The most well-known, and notorious, weather phenomenon in the Gulf is the *Shamal*, a NW wind which occurs year round (Perrone, 1979). *Shamal* is an Arabic word meaning north. The Winter *Shamal* is a wind that sets in with great abruptness and force, and is related to synoptic weather systems to the NW. It seldom exceeds 10 m/s (<5% frequency) but lasts several days (Reynolds, 1993). The summer *Shamal* is practically continuous from early June through July. It is associated with the relative strengths of the Indian and Arabian Peninsula thermal lows.

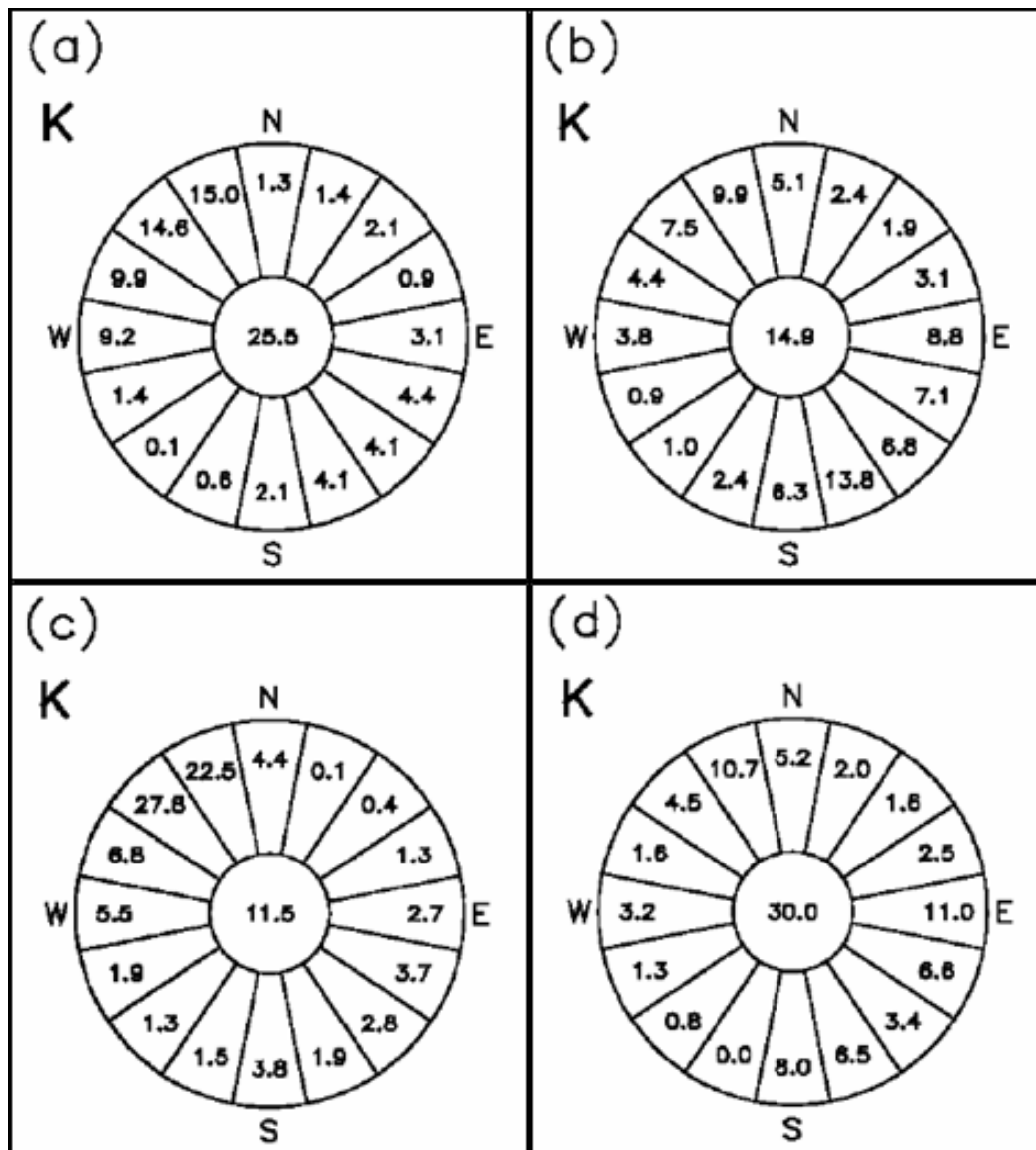


Figure 6. Frequency of the hourly wind direction and calms (in center) observed at Kuwait International Airport (K) in 2002: (a) January; (b) April; (c) July; (d) October (After Zhu and Atkinson, 2004).

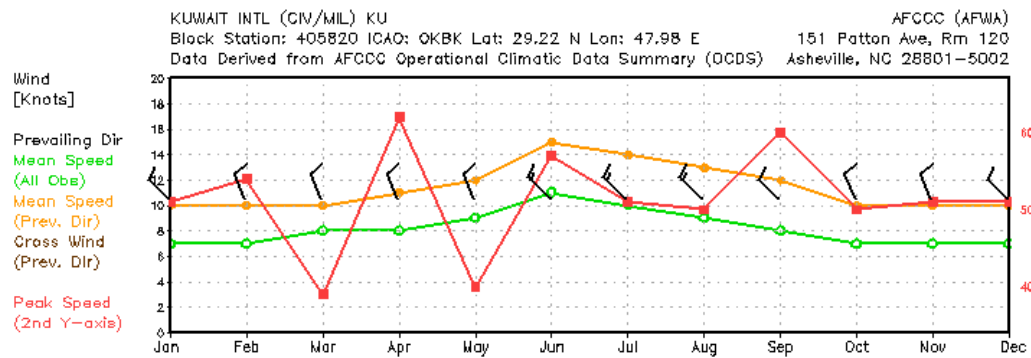


Figure 7. Climatological summary of winds at Kuwait International airport. Scale on the right is for peak winds and range between 30 and 70 knots (From AFCCC <https://notus2.afccc.af.mil/SCISPublic/>, 2007).

The winter *Shamal* brings some of the strongest winds and highest seas of the season to the Gulf region (Reynolds, 1993). Winds in the area ahead of an approaching cold front blow from the southeast. These winds, called *Kaus* in Arabic or *Shakki* in Arabian, slowly increase in intensity as the front approaches. Winds may reach gale force before the passage of the front and the onset of the *Shamal*. Due to the channeling of the low-level air flow by the Zagros Mountains of western Iran, the strongest of the southerly winds occur on the eastern seaboard. The *Shamal* usually occurs first in the northwest and then spreads south.

Zhu and Atkinson (2004) completed a study of observed and modeled climatology in the Persian Gulf. Part of that study included Kuwait International Airport (KWI), located at  $29.23^{\circ}N$   $48.97^{\circ}E$ . In January (Figure 6a), wind direction at KWI was predominantly northwesterly. In April (Figure 6b), at KWI, southeasterly and easterly directions were now of significant frequency. In July (Figure 6c), northwesterly and northerly directions again dominated the area near KWI. By October (Figure 6d), easterly and southeasterly directions were more evident at KWI. Northwesterly flow was dominant for most of the year over the entire Gulf, except the eastern area near Bandar Abbas. Over the west coast of the Gulf the picture was not clear cut. At KWI in January the direction of the mean wind was clearly from the northwest, but on some occasions the

wind blew from the east between 1400 LT (1100 UTC) and 2000 LT (1700 UTC). In April, the direction of the daytime mean wind was from the east and southeast, i.e. from the sea. In July, the mean direction was again from the northwest throughout the day. The October pattern was rather similar to that in April.

A strong sea breeze occurs along the entire coastline, especially along the Arabian Peninsula. Driven by the intense temperature difference between the land and water surfaces, the sea breeze circulation adds a landward component to all winds. The effect of these winds is to drive surface pollutants (oil and others) to the beach much faster than they would move otherwise. Examples of on- or off-shore winds as high as 15 m/s are evident in coastal meteorological stations (Reynolds, 1993).

### **C. TIDES**

The tides in the Gulf co-oscillate with those in the narrow Strait of Hormuz, which opens into the deep Gulf of Oman (Figure 8). The tides in the Gulf are complex standing waves and the dominant pattern varies from being primarily semi-diurnal to diurnal. The tidal range is large, with values greater than 1.0 m everywhere (Reynolds, 1993). The dimensions of the Gulf are such that resonance amplification of the tides can occur and the result is that the semi-diurnal constituents have two amphidromic points, in the northwest and southeast ends, and the diurnal constituents have a single amphidromic point in the center near Bahrain.

Tides are important for stirring and mixing waters vertically and on a horizontal scale of 10 km, but tides are not an important contribution to the residual circulation of the Gulf (Reynolds, 1993). Tidal current (averaging longer than a day) has negligible residual energy, and as a result, basin-scale advection from tides is not considered by most oil trajectory models or general circulation models. Tides are important on smaller scales of horizontal length ( $< 10$  km) and time ( $< 24$  hr).

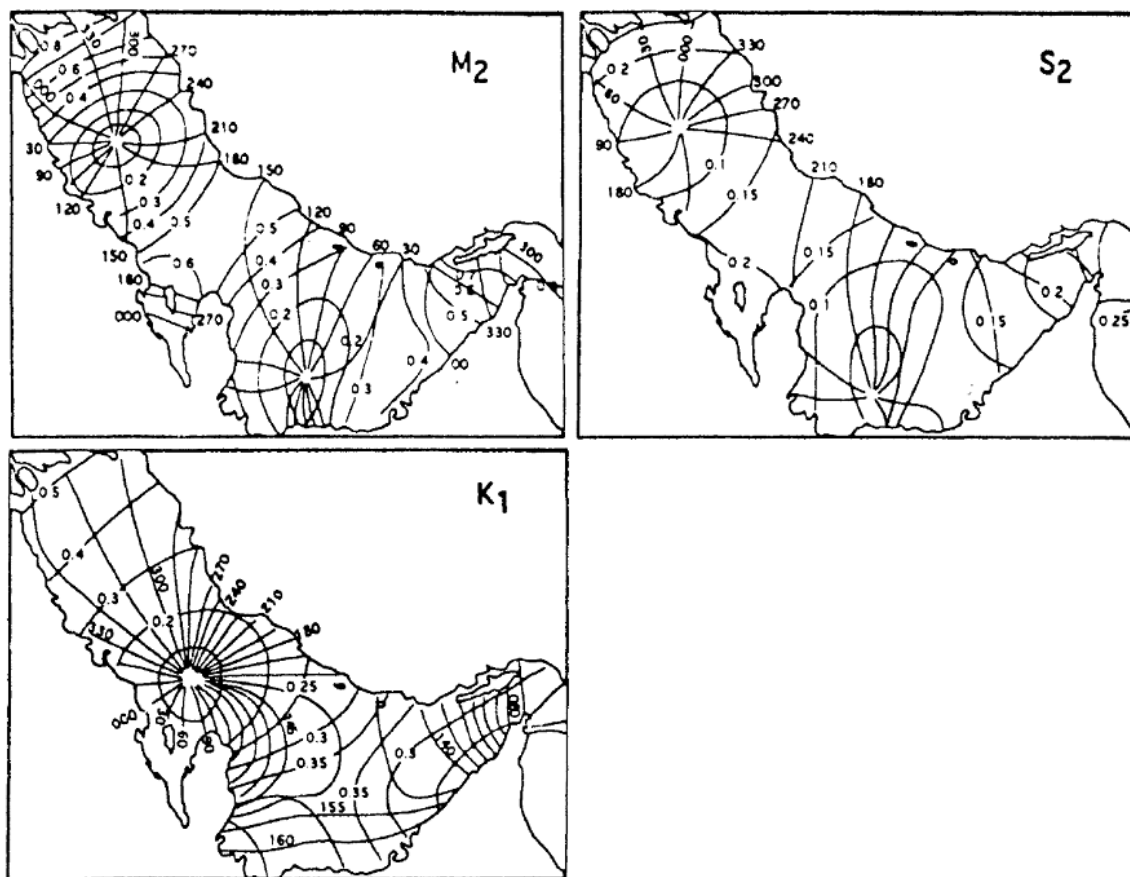


Figure 8. The  $M_2$ ,  $S_2$ , and  $K_1$  tidal constituents in the Gulf (After: Reynolds., 1993). Tide heights are shown in meters.

#### D. CURRENTS: TIDAL, WIND-DRIVEN, AND DENSITY DRIVEN

The energy in the water motion can be related to three forcing processes: tidal forces, wind forces, and density differences. The kinetic energy of the water velocity can be partitioned among the three terms approximately as 100, 10, and 1 respectively (Reynolds, 1993). Each of the different currents has a different scaling time: tides vary over a few hours at diurnal or semi-diurnal periods, wind-driven currents develop and subside over a few days; and density-driven currents take weeks to change in response to seasonal forcing. These three current components can be extracted from measurements, but the selection of averaging times and filter types affects the computed proportions considerably and must be used with care. Because of their consistent direction, density currents are important in the distribution and removal of pollutants from the Gulf region.



The main features of the residual circulation in the Gulf are (Hunter, 1983): (1) high- and low-salinity water exchange in the Strait of Hormuz; (2) density-dominated circulation in the central and southern regions; (3) frictional-balanced, wind-dominated circulation in the NW region; and (4) evaporation-induced bottom flow. The actual pattern of circulation is complex.

An important, secondary current in the Gulf is a coastal, reverse circulation along the Iranian coast. Driven by the density differences that result from river runoff, the coastal currents along the Iranian coast are southerly, against the inflow water. The reverse currents are evident in shuttle photographs and Advance Very High Resolution Radiometer (AVHRR) images (Reynolds, 1993). The interface between the two currents is a region of horizontal current shear which often shows evidence of wavelike shear instability.

#### **E. MIXING PROCESSES AND VERTICAL STRUCTURE.**

There are three, primary contributors to mixing to the water column: (1) tides, (2) winds and waves, and (3) evaporation. Internal waves at density interfaces, and topographic features such as islands also contribute to mixing, but their contribution is unknown and probably small (Reynolds, 1993). The strong tidal currents create a bottom, mechanical, turbulent friction layer. The enhanced turbulent mixing homogenizes the water column from the bottom up, and a bottom mixed layer is evident in all hydrographic sections. The other two mechanical mixing processes are strongest at the surface. Wind friction creates a surface shear layer and also creates surface wave fields, both of which form a surface mixed layer. Evaporation of fresh water enhances mixing by increasing the salinity and density of the surface water, thus reducing surface stability. In the winter, combined cooling and evaporation increase the density sufficiently to overturn the water column and, north of Qatar, create a well-mixed water column.

Mixing processes are opposed by the stabilizing effects of surface warming. As the temperature increases, the water density decreases. Countering this stabilization, evaporation increases surface salinity, which increases density and creates an unstable overturn to some lower depth. The resulting surface mixed layer and lower thermocline reach about 20 m depth (Reynolds, 1993).

THIS PAGE INTENTIONALLY LEFT BLANK

### III. OCEAN-ATMOSPHERIC PHYSICAL-CHEMICAL MODELS

This thesis utilizes two physical models and two chemical models. Among them, COAMPS and HPAC are the physical and chemical models for the atmosphere; and SWAFS and CHEMMAP<sup>TM</sup> (developed by the Applied Science Associates (ASA), Inc) are the physical and chemical models for the ocean. The model output of COAMPS such as the winds is the input for the atmospheric chemical model (HPAC) and the oceanic physical and chemical models: SWAFS and CHEMMAP. To solely study the effects of atmospheric dispersion HPAC was utilized. To understand the impacts of surface currents and winds on mine drifting and chemical spill, the Lagrangian drift model and CHEMMAP were employed. The following section will describe the model characteristics and uses.

#### A. COAMPS

The following overview of COAMPS is taken directly from Chen et al. (2003). The atmospheric component of COAMPS, the portion used for this analysis, can be used for real-data applications. For these applications, the COAMPS analysis can use global fields from the Navy Operational Global Atmospheric Prediction System (NOGAPS) forecast as the first-guess. Observations from aircraft, rawinsondes, ships, and satellites are blended with the first-guess fields to generate the current analysis. The atmospheric model uses nested grids to achieve high resolution for a given area; it contains parameterizations for subgrid scale mixing, cumulus parameterization, radiation, and explicit moist physics.

The atmospheric portion of the COAMPS models is comprised of the nonhydrostatic, fully compressible equations of motion following Klemp and Wilhelmson (1978). The adiabatic equations are developed using the equation of state:

$$p = \rho R_d T_v, \quad (3.1)$$

where  $p$  is the pressure,  $\rho$  is the density,  $R_d$  is the dry gas constant, the virtual temperature,  $T_v$  is

$$T_v = T(1.0 + 0.608q_v), \quad (3.2)$$

where  $T$  is the temperature and  $q_v$  is the specific humidity, and the Exner function,

$$\pi = \left( \frac{p}{p_{00}} \right)^{R_d/c_p}, \quad (3.3)$$

where  $c_p$  is the specific heat at constant pressure, and  $p_{00}$  the reference pressure.

The transformation of the vertical coordinate following Gal-Chen and Somerville (1975) is applied to map the lowest coordinate surface to an irregular lower boundary

$$\sigma = z_{top} \left( \frac{z - z_{sfc}}{z_{top} - z_{sfc}} \right), \quad (3.4)$$

where  $z_{top}$  is the depth of the model domain and  $z_{sfc}$  is the height of the topography.

Both the horizontal and vertical grids in the forecast model are staggered. The horizontal grid uses the Arakawa and Lamb (1977) scheme C staggering depicted in the Figure 9. The scalar variables (denoted  $\pi$ ) are defined in the center of the model grid box:

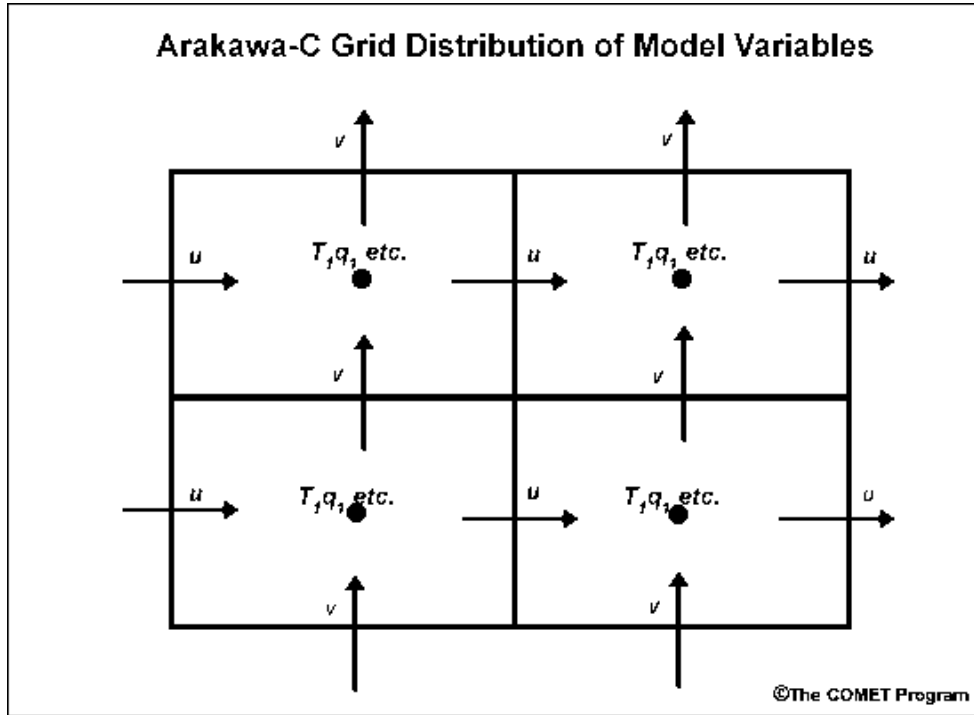


Figure 9. Diagram of Arakawa scheme C (From: Comet Module <http://www.comet.ucar.edu/>, 2007).

The computational grid features: (1) the  $u$ -component are one-half grid intervals between the mass points in the  $x$  direction, (2) the  $v$ -component are one-half grid intervals between the mass points in the  $y$  direction, and (3) the  $w$ -component, are coincident with the mass variables. In general, all derivatives are computed to second-order accuracy. Exceptions are the horizontal diffusion and an option for fourth-order accurate horizontal advection. By using fourth order accurate horizontal diffusion, the damping is much more specific to the removal of high-frequency modes.

Solving the fully compressible, nonhydrostatic equations explicitly is extremely computational expensive because of the presence of sound waves that severely limit the time step required to maintain computational stability. One approach for addressing this problem is to treat the sound wave modes separately on a small time step following Klemp and Wilhelmson (1978) and Skamarock and Klemp (1992).

The equations are solved using the centered-in-time or leapfrog scheme (Haltiner and Williams 1980). Typically, the time splitting due to the leapfrog scheme is not problematic (e.g., Klemp and Wilhelmson 1978). However, a Robert (1966) time smoother is applied to assure that any tendencies that may tend to decouple the odd and even time steps are stable. For any variable  $\phi$ , the Robert time filter is applied as

$$\left. \begin{aligned} \phi^{*t+\Delta t} &= \phi^{t-\Delta t} + 2\Delta t \phi^{*t} \\ \phi^t &= \phi^{*t} + \alpha \left( \phi^{*t+\Delta t} - 2\phi^{*t} + \phi^{t-\Delta t} \right) \end{aligned} \right\} . \quad (3.5)$$

The first equation corresponds to the leapfrog step for

$$\frac{\partial \phi}{\partial t} = F ,$$

with the asterisk corresponding to provisional terms that have not yet been smoothed through application of the second step. The net effect is to produce strong damping of the computational mode, while the physical mode is generally not affected (Asselin 1972). For typical COAMPS applications,  $\alpha$  is 0.2.

COAMPS uses a level 2.5 scheme (Mellor and Yamada 1982) that solves both a prognostic equation for turbulent kinetic energy (TKE) and diagnostic equations for second-moment quantities such as primarily fluxes of heat, moisture, and momentum. Schemes that feature a prognostic equation for TKE and diagnostic equations for other quantities are referred to as “1.5 order closure.” Thus, COAMPS contains a 1.5 order closure, level 2.5 scheme.

The 1.5 order closure, level 2.5 scheme computes all of the fields necessary for solving the TKE equation, including boundary layer depth, turbulent mixing length, flux, Richardson number, and eddy coefficients. In addition, the scheme incorporates the influence of boundary layer cloudiness.

The surface layer parameterization follows the Louis (1979) scheme, which uses polynomial functions of the bulk Richardson number to directly compute surface sensible heat flux, surface latent heat flux, and surface drag. The bulk Richardson number is defined as

$$Ri_B = \frac{gz\Delta\theta}{u^2\Theta}, \quad (3.6)$$

where  $g$  is the acceleration due to gravity,  $z$  is the reference elevation (equal to 10 m in COAMPS),  $\Delta\theta$  is the air-sea temperature difference,  $u$  is the wind speed at the reference elevation, and  $\Theta$  is the mean potential temperature over the depth of the surface layer.

Surface roughness (Fairall et al. 1996) is obtained by

$$z_0 = c_0 \frac{u_*^2}{g} + c_v \frac{\nu}{u_*}, \quad (3.7)$$

where  $c_0$  is the Charnock constant,  $u^*$  is the friction velocity,  $g$  is the acceleration due to gravity,  $c_v$  is a constant, and  $\nu$  is the molecular viscosity. The first term is the Charnock relation that accounts for high wind (aerodynamically rough conditions), while the second term accounts for low wind (aerodynamically smooth conditions).

Although the equations are solved on a staggered, scheme C grid, the COAMPS analysis is performed on the Arakawa-Lamb scheme A grid (i.e., no grid staggering). The bicubic spline interpolation is used to interpolate the analyzed fields to the C grid within the forecast model code.

The COAMPS analysis is based on the multivariate optimum interpolation (MVOI) analysis scheme described in Goerss and Phoebus (1992) and Barker (1992). The MVOI technique uses observational data to compute increments for the first-guess fields. If computed over a statistically significant number of cases, it minimizes the mean squared error of the analysis. The analysis variables for the MVOI are geopotential height, and the  $u$  and  $v$  wind components. Finally, the first-guess fields are adjusted based on observational data via a MVOI analysis. Observational data include the following data types: (1) Radiosonde, (2) Pibal, (3) Surface land, (4) Surface marine, (5) Aircraft, (6) Satellites (including SSM/I, Scatterometer, Sea Surface Temperature, and QUIKScat), and (7) Synthetic observations from NOGAPS. The cutoff for data used is  $\pm 3:00$  hours from the analysis time. Conventional data are subjected to quality control (Baker, 1992 and 1994) including gross check error checking and complex quality control of radiosonde observations (Gandin, 1988). Quality control of aircraft data includes sophisticated flight track checking and characteristic error detection (Pauley 2001). Within the MVOI itself, both satellite and conventional data are further checked for quality and for consistency with neighboring observations and the model short-term forecast, which is used as a "first guess" for the analysis.

After going through quality control, the time/space adjusted model forecast variables are compared to the observations to determine differences to be input into the analysis program. The differences are then weighted by a factor based on the reliability of the observations (instrument error characteristics, for example) relative to that of the first guess. A mathematical procedure is then employed to minimize the analysis error, based on the assumed observation and model forecast error characteristics. The resulting analysis increments are then applied to the first guess, resulting in a new analysis.

## B. SWAFS

SWAFS is a coastal ocean forecast system in operational use at the Naval Oceanographic Office (Clifford, et al., 1994). The modeling system is built based on the Princeton Ocean Model (POM) with the main differences in data assimilation.

The following overview of POM is taken directly from Mellor (2004). The principal attributes of the model are as follows: (1) It contains an imbedded second moment turbulence closure sub-model to provide vertical mixing coefficients, (2) It is a sigma coordinate model in that the vertical coordinate is scaled on the water column depth, (3) The horizontal grid uses curvilinear orthogonal coordinates and an "Arakawa C" differencing scheme, (4) The horizontal time differencing is explicit whereas the vertical differencing is implicit. The latter eliminates time constraints for the vertical coordinate and permits the use of fine vertical resolution in the surface and bottom boundary layers. (5) Complete thermodynamics have been implemented.

The turbulence closure sub-model is one that Mellor and then was significantly advanced in collaboration with Tetsuji Yamada (Mellor and Yamada, 1974; Mellor and Yamada, 1982). Here, the Level 2.5 model is used together with a prognostic equation for the turbulence macroscale.

By and large, the turbulence model seems to do a fair job simulating mixed layer dynamics although there have been indications that calculated mixed layer depths are a bit too shallow (Martin, 1985). Also, wind forcing may be spatially and temporally smoothed. It is known that the latter process will reduce mixed layer thicknesses (Klein, 1980).

The basic equations have been cast in a bottom following, sigma coordinate system which is illustrated in Figure 10. The reader is referred to Phillips (1957), and Blumberg and Mellor (1980, 1987) for a derivation of the sigma coordinate equations which are based on the transformation,

$$x^* = x, y^* = y, \sigma = \frac{z - \eta}{H + \eta}, t^* = t \quad (3.8)$$



where  $x, y, z$  are the conventional Cartesian coordinates; where  $H(x, y)$  is the bottom topography and  $\eta(x, y, t)$  is the surface elevation. Thus,  $\sigma$  ranges from  $\sigma = 0$  at  $z = \eta$  to  $\sigma = -1$  at  $z = H$ . The sigma coordinate system is probably a necessary attribute in dealing with significant topographical variability such as that encountered in estuaries or over continental shelf breaks and slopes.

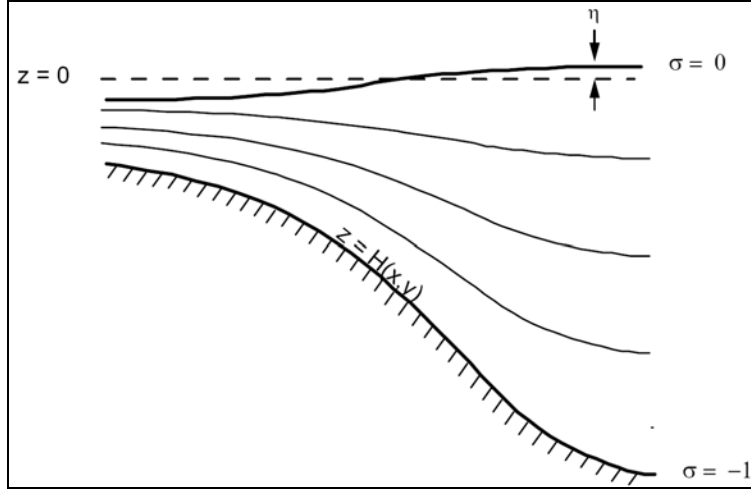


Figure 10. The sigma coordinate system. (From: Mellor, 2004)

Let  $(U, V)$  be the horizontal velocity components;  $\rho$  be the density; ( $K_M, K_H$ ) be the eddy viscosity and thermal diffusivity. After conversion to sigma coordinates and deletion of the asterisks, the continuity equation is given by

$$\frac{\delta DU}{\delta x} + \frac{\delta DV}{\delta y} + \frac{\delta \omega}{\delta \sigma} + \frac{\delta \eta}{\delta t} = 0. \quad (3.9)$$

Note that  $\omega$  is the vertical velocity component in the sigma coordinate system. The horizontal momentum equations are given by

$$\begin{aligned} \frac{\partial UD}{\partial t} + \frac{\partial U^2 D}{\partial x} + \frac{\partial UVD}{\partial y} + \frac{\partial U \omega}{\partial \sigma} - fVD + gD \frac{\partial \eta}{\partial x} + \frac{gD^2}{\rho_0} \int_{\sigma}^0 \left[ \frac{\partial \rho'}{\partial x} - \frac{\sigma'}{D} \frac{\partial D}{\partial x} \frac{\partial \rho'}{\partial \sigma'} \right] d\sigma' \\ = \frac{\partial}{\partial \sigma} \left[ \frac{K_M}{D} \frac{\partial U}{\partial \sigma} \right] + F_x \end{aligned} \quad (3.10)$$

$$\begin{aligned} \frac{\partial VD}{\partial t} + \frac{\partial UVD}{\partial x} + \frac{\partial V^2 D}{\partial y} + \frac{\partial V \omega}{\partial \sigma} + fUD + gD \frac{\partial \eta}{\partial y} + \frac{gD^2}{\rho_0} \int_{\sigma}^0 \left[ \frac{\partial \rho'}{\partial y} - \frac{\sigma'}{D} \frac{\partial D}{\partial y} \frac{\partial \rho'}{\partial \sigma'} \right] d\sigma' \\ = \frac{\partial}{\partial \sigma} \left[ \frac{K_M}{D} \frac{\partial V}{\partial \sigma} \right] + F_y \end{aligned} \quad (3.11)$$

The heat and salt equations are represented by

$$\frac{\partial TD}{\partial t} + \frac{\partial TUD}{\partial x} + \frac{\partial TVD}{\partial y} + \frac{\partial T \omega}{\partial \sigma} = \frac{\partial}{\partial \sigma} \left[ \frac{K_H}{D} \frac{\partial T}{\partial \sigma} \right] + F_T - \frac{\partial R}{\partial z} \quad (3.12)$$

$$\frac{\partial SD}{\partial t} + \frac{\partial SUD}{\partial x} + \frac{\partial SVD}{\partial y} + \frac{\partial S \omega}{\partial \sigma} = \frac{\partial}{\partial \sigma} \left[ \frac{K_H}{D} \frac{\partial S}{\partial \sigma} \right] + F_S. \quad (3.13)$$

The eddy viscosity  $K_M$  and thermal diffusivity  $K_H$  are expressed by

$$K_M = lqS_M, \quad K_H = lqS_H$$

where  $l$  is the mixing length,  $q$  is the turbulent speed, and  $S_M$  and  $S_H$  are stability functions which are analytical derived, algebraic relation functionally dependent upon  $\partial U / \partial z$ ,  $\partial V / \partial z$ ,  $\partial \rho / \partial z$ ,  $q$ , and  $l$ . The level-2 turbulent closure scheme is used:

$$\begin{aligned} \frac{\partial q^2 D}{\partial t} + \frac{\partial Uq^2 D}{\partial x} + \frac{\partial Vq^2 D}{\partial y} + \frac{\partial \omega q^2}{\partial \sigma} \\ = \frac{\partial}{\partial \sigma} \left[ \frac{K_q}{D} \frac{\partial q^2}{\partial \sigma} \right] + \frac{2K_M}{D} \left[ \left( \frac{\partial U}{\partial \sigma} \right)^2 + \left( \frac{\partial V}{\partial \sigma} \right)^2 \right] + \frac{2g}{\rho_0} K_H \frac{\partial \tilde{\rho}}{\partial \sigma} - \frac{2Dq^3}{B_1 \ell} + F_q \end{aligned} \quad (3.14)$$

$$\begin{aligned} \frac{\partial q^2 \ell}{\partial t} + \frac{\partial Uq^2 \ell}{\partial x} + \frac{\partial Vq^2 \ell D}{\partial y} + \frac{\partial \omega q^2 \ell}{\partial \sigma} = \frac{\partial}{\partial \sigma} \left[ \frac{K_q}{D} \frac{\partial q^2 \ell}{\partial \sigma} \right] \\ + E_1 \ell \left( \frac{K_M}{D} \left[ \left( \frac{\partial U}{\partial \sigma} \right)^2 + \left( \frac{\partial V}{\partial \sigma} \right)^2 \right] + E_3 \frac{g}{\rho_0} K_H \frac{\partial \tilde{\rho}}{\partial \sigma} \right) - \frac{Dq^3}{B_1} \tilde{W} + F_\ell \end{aligned} \quad (3.15)$$

The transformation to the Cartesian vertical velocity is given by

$$W = \omega + U \left( \sigma \frac{\partial D}{\partial x} + \frac{\partial \eta}{\partial x} \right) + V \left( \sigma \frac{\partial D}{\partial y} + \frac{\partial \eta}{\partial y} \right) + \sigma \frac{\partial D}{\partial t} + \frac{\partial \eta}{\partial t}, \quad (3.16)$$

which satisfies the no-flow boundary conditions at the surface and the bottom.

In (3.10) and (3.11),  $\rho_{MEAN}$  should be subtracted from  $\rho$  to form  $\rho'$  before the integration.  $\rho_{MEAN}$  is generally the initial density field which is area averaged on z-levels

and then transferred to sigma coordinates in the exact same way as the initial density field. This procedure should reduce the truncation errors associated with the calculation of the pressure gradient term in sigma coordinate over steep topography (see Mellor et al., 1994 and Mellor et al. 1998 for evaluation of this error in POM).

POM generally uses the Smagorinsky diffusivity for horizontal diffusion although a constant or biharmonic diffusion can and has been used instead. The Smagorinsky formula is

$$A_M = C\Delta x\Delta y \frac{1}{2} \left| \nabla V + (\nabla V)^T \right|, \quad (3.17)$$

where

$$\left| \nabla V + (\nabla V)^T \right| = \left[ \left( \partial u / \partial x \right)^2 + \left( \partial v / \partial x + \partial u / \partial y \right)^2 + \left( \partial v / \partial y \right)^2 \right]^{1/2}.$$

Values of C (the HORCON parameter) in the range, 0.10 to 0.20 seem to work well, but, if the grid spacing is small enough (Oey et al, 1985a, b), C can be nil. An advantage of the Smagorinsky relation is that C is non-dimensional; related advantages are that  $A_M$  decreases as resolution improves and that  $A_M$  is small if velocity gradients are small.

The equations, governing the dynamics of coastal circulation, contain fast moving external gravity waves and slow moving internal gravity waves. It is desirable in terms of computer economy to separate the vertically integrated equations (external mode) from the vertical structure equations (internal mode). This technique, known as mode splitting (Simons, 1974; Madala and Piacsek, 1977) permits the calculation of the free surface elevation with little sacrifice in computational time by solving the velocity transport separately from the three-dimensional calculation of the velocity and the thermodynamic properties.

The velocity external mode equations are obtained by integrating the internal mode equations over the depth, thereby eliminating all vertical structure. Thus, by integrating Equation (3.9) from  $\sigma = -1$  to  $\sigma = 0$  and using the boundary conditions, an equation for the surface elevation can be written as

$$\frac{\delta\eta}{\delta t} + \frac{\delta\bar{U}D}{\delta x} + \frac{\delta\bar{V}D}{\delta y} = 0 \quad (3.18)$$

The Courant-Friedrichs-Levy (CFL) computational stability condition on the vertically integrated, external mode, transport equations limits the time step according to

$$\Delta t_E \leq \frac{1}{C_t} \left| \frac{1}{\delta x^2} + \frac{1}{\delta y^2} \right|^{-1/2} \quad (3.19)$$

where  $C_t = 2(gH)^{1/2} + U_{\max}$ ;  $U_{\max}$  is the expected, maximum velocity. There are other restrictions but in practice the CFL limit is the most stringent. The model time step is usually 90% of this limit. The internal mode has a much less stringent time step since the fast moving external mode effects have been removed. For typical coastal ocean conditions the ratio of the time steps,  $\Delta t_I / \Delta t_E$ , is often a factor of 30-80 or larger. For more information on the sensitivity of POM to time steps (Ezer et al., 2002). In SWAFS, the horizontal resolution is 2 km and the time step is 50 s.

Together with the turbulence sub-model, the model produces realistic bottom boundary layers which are important in coastal waters (Mellor, 1985) and in tidally driven estuaries (Oey et al., 1985a, b) which the model can simulate since it does have a free surface.

SWAFS is run using a 24 hour hindcast and 48 hour forecast (Figure 11). The hindcast is utilized to incorporate ‘real-time’ data. Unlike atmospheric models, observations come in slower and are not as spatially diversified. There are areas within the ocean that very few observations of the subsurface are ever recorded.

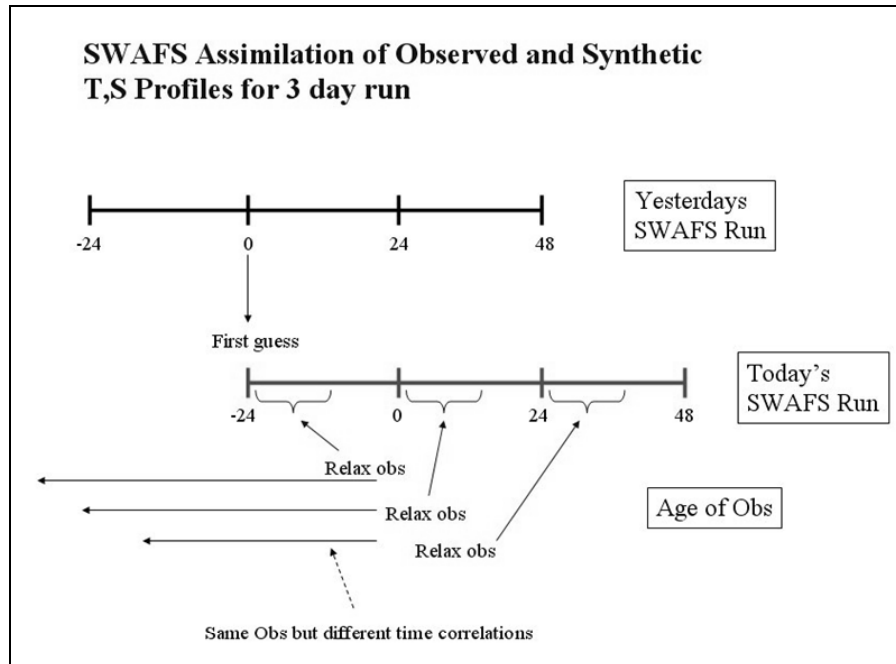


Figure 11. SWAFS model run cycle. (From: Haeger, S.D., 2006)

The data incorporated into the hindcast originates from a variety of sources. These sources can be generalized as falling into one of the following categories: (1) sub-surface assimilation, (2) near-surface assimilation, (3) lateral boundary conditions, (4) meteorological fluxes, and (5) tides. Each of these categories has a different path to get data into SWAFS. Data assimilation for sub-surface assimilation starts with near real-time altimetry, Sea Surface Temperature (SST) and a database of climatological data being ingested into the Modular Ocean Data Assimilation System (MODAS). MODAS then creates synthetic Conductivity/Temperature/Depth (CTD) profiles, which are then added to the spotty real CTD's and Bathythermograph (BT) data. These profiles are then used to create temperature profiles and, indirectly, salinity profiles through optimum interpolation (OI). This data is then spatially 'relaxed', or decorrelated, to prevent 'bullseyes' from appearing in the output. Near-surface data assimilation has a much shorter path, which primarily consists of other multichannel SSTs (MCSSTs) that are incorporated in via OI. This data is decorrelated in much the same way as discussed previously. Tides can be utilized by enabling coastal stations. This is done if it is determined that the region benefits from tidal information. This is not the case for all regions, especially the open ocean. Meteorological Fluxes are incorporated by taking a

NOGAPS-COAMPS blend into the model. As SWAFS goes through a daily run, a 24 hour hindcast is run with the previously mentioned data getting assimilated. As the forecast portion of the model run begins, the same data will be incorporated in again with less spatial dependence. As seen in Figure 11, this is done again at the 24 hour forecast mark. The reason this is done is that through experimentation by the modelers, this method has been determined to give the best results. Several of the features discussed previously can be utilized or turned off depending on the region that SWAFS is being run. In the confidence level assessment of MODAS (CLAM) study, models are tested in a given region to determine which features work best (Fox, 2000). Once the best configuration has been determined, SWAFS will be run as discussed previously.

### **C. HPAC AND SECOND-ORDER CLOSURE INTEGRATED PUFF (SCIPUFF)**

The following overview is taken directly from Sykes et al (2000). It is used to accurately predict the effects of hazardous material releases into the atmosphere and its impact on civilian and military populations. The system uses integrated source terms, high-resolution weather forecasts and particulate transport analyses to model hazard areas produced by military or terrorist incidents and industrial accidents. The HPAC system can also help answer the question, “How good is the prediction?” by providing probabilistic calculations. The hazard area feature estimates the weather uncertainty and turbulence effects on possible plume trajectories and calculates the areas of hazard impact and the degree of confidence of the prediction.

This is where the HPAC model is unique because it can provide a hazard prediction with a corresponding estimate of confidence. It bases this confidence on estimates of the uncertainty inherent in the forecast or observed weather data. These estimates are calculated using real time probabilistic methods or via empirical models embedded within the software. The SCIPUFF model is the atmospheric transport empirical model used in HPAC.

Transport of contaminants in the turbulent atmosphere has an intrinsic stochastic character. Typical deterministic predictive models provide an ensemble mean concentration value, but are not able to predict the exact path and diffusion due to

unpredictable turbulent motions of the atmosphere. A probabilistic transport model predicts both ensemble means and variances, and has a unique role in that it can provide rational uncertainty bounds on prediction of contaminant concentrations and dosages.

SCIPUFF model is the atmospheric transport engine currently used in HPAC. SCIPUFF is a Lagrangian transport and diffusion model for atmospheric dispersion applications. SCIPUFF describes two basic aspects of the model. First, the numerical technique employed to solve the dispersion model equations is the Gaussian puff method (Bass, 1980) in which a collection of three-dimensional puffs is used to represent an arbitrary time-dependent concentration field. Second, the turbulent diffusion parameterization used in SCIPUFF is based on the second-order turbulence closure theories of Donaldson (1973) and Lewellen (1977), providing a direct connection between measurable velocity statistics and the predicted dispersion rates.

The Lagrangian puff methodology affords a number of advantages for atmospheric dispersion applications from localized sources. The Lagrangian scheme avoids the artificial diffusion problems inherent in any Eulerian advection scheme, and allows an accurate treatment of the wide range of length scales as a plume or cloud grows from a small source size and spreads onto larger atmospheric scales. This range may extend from a few meters up to continental or global scales of thousands of kilometers. In addition, the puff method provides a very robust prediction under coarse resolution conditions, giving a flexible model for rapid assessment when detailed results are not required. The model is highly efficient for multiscale dispersion problems, since puffs can be merged as they grow and resolution is therefore adapted to each stage of the diffusion process.

The efficiency of SCIPUFF has been improved by the implementation of adaptive time stepping and output grids. Each puff uses a time step appropriate for resolving its local evolution rate, so that the multiscale range can be accurately described in the time domain without using a small step for the entire calculation. The output spatial fields are also computed on an adaptive grid, avoiding the need for the user to specify grid information and providing a complete description of the concentration field within the computational constraints under most conditions.

The generality of the turbulence closure relations provides a dispersion representation for arbitrary conditions. Empirical models based on specific dispersion data are limited in their range of application, but the fundamental relationship between the turbulent diffusion and the velocity fluctuation statistics is applicable for a much wider range. Understanding of the daytime planetary boundary layer velocity fluctuations provides reliable input for the second-order closure description of dispersion for these conditions. The closure model has been applied on local scales up to 50 km range (Sykes et al., 1988) and also on continental scales up to 3000 km range (Sykes et al., 1993).

The second-order closure model also provides the probabilistic feature of SCIPUFF through the prediction of the concentration fluctuation variance. In addition to giving a mean value for the concentration field, SCIPUFF provides a quantitative value for the random variation in the concentration value due to the stochastic nature of the turbulent diffusion process. This uncertainty estimate is used to provide a probabilistic description of the dispersion result, and gives a quantitative characterization of the reliability of the prediction. For many dispersion calculations, the prediction is inherently uncertain due to a lack of detailed knowledge of the wind field and a probabilistic description is the only meaningful approach.

### 1. Gaussian Moment Definition

SCIPUFF uses a Gaussian puff representation for the concentration field of a dispersing contaminant. A three-dimensional Gaussian is completely described by its spatial integral moments up to second-order, and can be written in the form

$$c(x) = \frac{Q}{(2\pi)^{3/2} (Det(\sigma))^{1/2}} \exp \left[ -\frac{1}{2} \sigma_{ij}^{-1} (x_i - \bar{x}_i) (x_j - \bar{x}_j) \right] \quad (3.21)$$

For atmospheric dispersion problems, one must also consider the effects of the ground surface and the capping inversion at the top of the planetary boundary layer, which are usually represented as reflective surfaces. The specific Gaussian variation (3.21) applies to an individual puff, but in general the local concentration field will be composed of a sum of contributions from a number of such puffs.



## 2. Moment Transport Equations

The advection-diffusion equation for a scalar quantity in an incompressible flow field can be written as

$$\frac{\delta c}{\delta t} + \frac{\delta}{\delta x_i} (u_i c) = k \nabla^2 c + S \quad (3.22)$$

where  $u_i(x, t)$  is the turbulent velocity field,  $k$  is the molecular diffusivity, and  $S$  represents the source terms.

The atmospheric velocity field is generally turbulent; therefore the Reynolds averaging technique is used to define a mean and a turbulent fluctuation value. Denoting the mean by an overbar and the fluctuation by a prime, one gets  $u = \bar{u} + u'$ , and a similar decomposition can be applied to the concentration,  $c$ . The Reynolds averaged conservation equation for the mean scalar concentration is thus

$$\frac{\delta \bar{c}}{\delta t} + \frac{\delta}{\delta x_i} (\bar{u}_i \bar{c}) = - \frac{\delta}{\delta x_i} (\overline{u'_i c'}) + k \nabla^2 \bar{c} + \bar{S} \quad (3.23)$$

where  $\overline{-u'_i c'}$  is the turbulent concentration flux.

## 3. Turbulence Closure Diffusion Model

The diffusion model in SCIPUFF is based on second-order turbulence closure, which provides a transport equation for the second order fluctuation terms. First-order closure prescribes the turbulent fluxes in terms of the local mean gradients using an empirical turbulent diffusivity, but a more general relation can be obtained from a higher-order closure. It is not the intention to review turbulence closure theory here, only provide the basic model description is provided; the interested reader can find detailed discussions in the literature, e.g., Mellor and Herring (1973), Launder et al. (1975), Lewellen (1977).

The equations for the puff moments involve the turbulent flux of concentration, and a rigorous conservation equation can be derived for this quantity from the scalar and momentum equations. Neglecting the molecular diffusion terms, the flux transport equation can be written in the form

$$\frac{\delta}{\delta t} \overline{u'_i c'} + \overline{u_j} \frac{\delta}{\delta x_j} \overline{u'_i c'} = \overline{u'_i u'_j} \frac{\delta \bar{c}}{\delta x_j} - \overline{u'_j c'} \frac{\delta \bar{u}_i}{\delta x_j} - \frac{\delta}{\delta x_j} \overline{u'_i u'_j c'} - \overline{c'} \frac{\delta \bar{p}'}{\delta x_i} + \frac{g_i}{T_0} \overline{c' \theta'} \quad (3.24)$$

This equation involves higher-order terms, such as the triple correlation and the pressure correlation, which must be modeled empirically. The model of Lewellen (1977) is used to form a closed equation for the turbulent flux, giving

$$\begin{aligned} \frac{\delta}{\delta t} \overline{u'_i c'} + \overline{u_j} \frac{\delta}{\delta x_j} \overline{u'_i c'} &= \overline{u'_i u'_j} \frac{\delta \bar{c}}{\delta x_j} - \overline{u'_j c'} \frac{\delta \bar{u}_i}{\delta x_j} + \frac{\delta}{\delta x_j} \left( v_c q \Lambda \frac{\delta}{\delta x_j} \overline{u'_i c'} \right) \\ &- A \frac{q}{\Lambda} \overline{u'_i c'} + \frac{g_i}{T_0} \overline{c' \theta'} \end{aligned} \quad (3.25)$$

where  $A = 0.75$  and  $v_c = 0.3$  are empirical model constants. The turbulent velocity scale,  $q$ , is defined as  $q^2 = \overline{u'_i u'_i}$ , and  $\Lambda$  is the turbulent length scale; these quantities will be discussed more fully below. The buoyancy term uses the Boussinesq approximation, and  $g_i = (0, 0, g)$  is the gravitational acceleration,  $T_0$  is the reference temperature, and  $\theta'$  is the potential temperature fluctuation.

The general equation (3.25) for the turbulent fluxes can be integrated spatially to provide transport equations for the flux moments. However, the multiple tensor indices give a large number of correlations to consider in the general case. Therefore, some restrictions are introduced for the atmospheric dispersion cases that allow this study to neglect many of the correlations. First, only consider the vertical component of the turbulent drift,  $\left\langle \overline{u'_i c'} \right\rangle$ , since advection by the mean wind will generally dominate in the horizontal directions. Second, the only off-diagonal component of the flux moment tensor,  $\left\langle x'_i \overline{u'_i c'} \right\rangle$ , to be considered will be the symmetric horizontal term:

$$X_{12} = \left\langle x_1' \overline{u_2' c'} \right\rangle + \left\langle x_2' \overline{u_1' c'} \right\rangle \quad (3.26)$$

In general, the off-diagonal terms represent puff distortions due to velocity covariances.

#### 4. Concentration Fluctuation Variance

The probabilistic aspect of the SCIPUFF dispersion prediction is based on the second-order closure model for the concentration fluctuation variance. The dispersion of any species in a turbulent velocity field is a random process since the turbulent fluctuations are effectively chaotic and cannot be measured or predicted in detail. The scalar concentration is therefore a stochastic quantity, with a probability distribution that depends on the distribution of velocity fluctuations. Traditional deterministic estimates of atmospheric dispersion only provide a single concentration value as a function of space and time, and this corresponds to the mean value,  $c$ , for some definition of the statistical ensemble. The mean value is the first moment of the probability distribution, and contains no information about the statistical variability in the prediction. Higher moments are required to give a quantitative description of the variability. The probabilistic aspect of the SCIPUFF dispersion prediction is based on a transport equation for the statistical variance in the concentration value that is the second moment of the probability distribution. The mean and the variance are then used to provide a probabilistic prediction using a parameterized probability density function.

The key aspect of the scalar variance prediction is the dissipation timescale. Proper characterization of the dissipation timescale allows an accurate prediction of the concentration fluctuation variance, as has been demonstrated in comparison with laboratory data (Sykes, Lewellen, and Parker, 1986) and also with large-scale atmospheric dispersion observations (Sykes et al., 1993). The second-order closure model for the dissipation rate was originally developed by Sykes et al. (1984) using the laboratory data of Fackrell and Robins (1982). A fundamental discovery in that study was that the scalar dissipation scales were an internal property of the scalar field itself, rather than being determined exclusively by the velocity fluctuations. Essentially, velocity eddies with scales larger than the scalar plume or cloud will meander the entire scalar distribution but not cause any nonlinear cascade of scalar fluctuation variance onto

smaller scales. The turbulent cascade process is only driven by eddies with scales similar to the instantaneous plume size. This is not the case for persistent mean wind shear, which can distort a cloud by means of the continued stretching.

The scalar variance dissipation model introduced by Sykes et al. (1984, 1986) uses a single estimate of the velocity and length scales to define the dissipation. This is appropriate for the case of plume dispersion in two dimensions with near-isotropic turbulence. Under the more general conditions of larger scale horizontal dispersion and arbitrary sources, characterization of the different dissipation rates associated with each direction are required. The vertical direction must be distinguished; two horizontal scales are also needed. The horizontal information is needed to distinguish between plume-type sources, where the diffusion occurs in two spatial dimensions, and puff-type sources, which diffuse in all three dimensions. As part of the concentration fluctuation prediction, therefore three length scales in addition to the fluctuation variance are required.

## 5. Numerical Techniques

The puff moment evolution equations given in Section C.1 generally increase the size of the puff through turbulent diffusion and elongation along the direction of the wind shear. As the puff grows, the local representation of the turbulence and velocity fields using the puff centroid location becomes increasingly inaccurate. When the meteorological fields are inhomogeneous, the accuracy of the calculation can only be maintained by splitting puffs into smaller components that can sample the variations in the meteorology explicitly. A grid-based method for splitting puffs was presented by Sykes and Henn (1992), where the moment method of Egan and Mahoney (1972) was extended to include some shear effects. In this scheme, grid cells can be thought of as each containing a Lagrangian puff. As the puffs move and spread into neighboring grid cells in a time step, the masses are redistributed so as to maintain a single puff within each cell. To avoid any numerical grid in the current method the redistribution cannot be based on the rectangular grid cells.

The three diagonal moments,  $\sigma_{\alpha\alpha}$ , give the effective length of the puff along each coordinate direction, and then the puff is split in the  $x$ -direction, for example, when

$\sigma_{11} > \Delta H^2$ . Here  $\Delta H$  represents the limit for the horizontal spread and should be chosen so that the linearization of the velocity and turbulence fields is valid for a Gaussian with smaller spread. Similar splitting criteria apply for the other two coordinate directions, using  $\Delta H$  in the  $y$ -direction and  $\Delta V$  in the  $z$ -direction.

To represent the original Gaussian puff with split in the  $x$ -direction as several smaller, overlapping puffs that conserve all the puff moments and only change local concentration values by a small amount, the original puff is replaced by two smaller puffs in the following manner. The new centroid locations are displaced by a fraction,  $r$ , of the puff spread in the  $x$ -direction, and by a distance proportional to the off-diagonal moment in the other two coordinate directions. Thus

$$\bar{x}_1^{(\alpha)} = \bar{x}_1 \pm r\sqrt{\sigma_{11}} \quad (3.27)$$

$$\bar{x}_2^{(\alpha)} = \bar{x}_2 \pm r \frac{\sigma_{12}}{\sqrt{\sigma_{11}}} \quad (3.28)$$

$$\bar{x}_3^{(\alpha)} = \bar{x}_3 \pm r \frac{\sigma_{13}}{\sqrt{\sigma_{11}}} \quad (3.29)$$

where  $\alpha = \{1, 2\}$  corresponds to the plus and minus sign, respectively. The diagonal moments for the new puffs are obtained using the following relations

$$\sigma_{11}^{(\alpha)} = \sigma_{11} (1 - r^2) \quad (3.30)$$

$$\sigma_{22}^{(\alpha)} = \sigma_{22} \left( 1 - \frac{r^2 \sigma_{12}^2}{\sigma_{11} \sigma_{22}} \right) \quad (3.31)$$

$$\sigma_{33}^{(\alpha)} = \sigma_{33} \left( 1 - \frac{r^2 \sigma_{13}^2}{\sigma_{11} \sigma_{33}} \right) \quad (3.32)$$

and the new off-diagonal moments are

$$\sigma_{12}^{(\alpha)} = \sigma_{12} (1 - r^2) \quad (3.33)$$

$$\sigma_{13}^{(\alpha)} = \sigma_{13} (1 - r^2) \quad (3.34)$$

$$\sigma_{23}^{(\alpha)} = \sigma_{23} - \frac{r^2 \sigma_{12} \sigma_{13}}{\sigma_{11}} \quad (3.35)$$

Conservation of all puff moments is ensured by this procedure, and the moments of the new puffs are all reduced and are also realizable. The realizability constraints involve the Schwartz inequality between the diagonal and off-diagonal moments. These properties can be verified directly from the above relations.

The generalized puff description contains other information in addition to the moments discussed above. The additional variables fall into two categories, either a conserved puff integral property (similar to the puff mass) or a puff value property (such as turbulence length scale). Integral properties are simply divided equally between the two new puffs, and the value properties are assigned equally to both.

## 6. Meteorology Specification

To make accurate calculations and predictions, hazard assessment planning and response tools must have access to three general types of weather data: (1) historical weather (climatology); (2) forecast weather (numerical weather predictions); and (3) current weather (observations). The type of weather data required depends upon the needs of the user. To plan scenarios that are either notional or seven days previous to an examined event, historical weather or climatology data is most suitable.

To plan or anticipate events within a seven-day period, forecast weather products are the data of choice. For a post-event or real-time response, the user usually requires access to current observations. Forecast and current weather data is available to the

Hazard Prediction and Assessment Capability program via the Defense Threat Reduction Agency (DTRA) Meteorological Data Servers (MDS), while historical data is included as part of the tool installation.

The meteorological data utilized for this research was twofold. For the climatological part of the scenario, the climatology inherent in HPAC was used. For the “real-time” scenarios, data collected from COAMPS forecasts was used.

#### **D. CHEMMAP™**

The following overview is taken directly from McCay (2001). Chemical spill modeling provides a powerful quantitative tool for estimating fate and potential impacts of chemical releases. Applied Science Associates (ASA) has been developed a chemical spill model, CHEMMAP™, to predict the trajectory and fate of a wide variety of chemical products, including floating, sinking, soluble and insoluble chemicals and product mixtures. CHEMMAP™ simulated a number of processes including: (1) slick spreading, transport, and entrainment of floating materials, (2) transport of dissolved and particulate materials in three dimensions, (3) evaporation and volatilization, (4) dissolution and adsorption, (5) sedimentation and resuspension, (6) and degradation. The model uses physical-chemical properties to predict the fate of a chemical spill. These include density, vapor pressure, water solubility, environmental degradation rates, adsorbed/dissolved partitioning coefficients ( $K_{ow}$ ,  $K_{oc}$ ), viscosity, and surface tension.

##### **1. CHEMMAP™ Chemical Database**

The CHEMMAP™ chemical database contains all the physical-chemical properties required by the model to simulate the transport and fate of the spilled material. The database includes a variety of text and numeric descriptors (names, synonyms, registry numbers, etc.), with which the user may identify and characterize the spilled chemical or mixture. The model is capable of simulating spills of pure chemicals, chemicals in aqueous or hydrophobic solutions, or chemicals in emulsions (i.e., mixtures of particulate material suspended in an aqueous base). Thus, the database also includes characteristics that define these mixtures and solutions. CHEMMAP™ uses either the Chemical Abstract System (CAS) registry number or the UN number to index the chemical. In addition, two other codes uniquely define the chemical state and formulation to be simulated: (1) State under spill conditions, (2) Formulation number (to allow multiple database entries for different concentrations of the same chemical and state code).

The chemical database is contained in a Microsoft Access table. The data may be viewed and edited from the user interface. The initial database of approximately 470 chemicals was taken from French et al. (1996). These data will continue to be updated as

new information becomes available. At present, the database has been increased to approximately 900 chemical substances, including those commonly transported in bulk and most likely to be spilled.

Several properties vary with temperature. Thus, the database values are for a standardized temperature of 25°C. The model corrects these parameters to the ambient temperature for the spill incident. The algorithms for changing viscosity and vapor pressure to ambient temperature are taken from French et al. (1996). For pure chemical processes, the increase per 10°C is assumed 2.

## **2. Chemical Fates Model**

The chemical fates model estimates the distribution of chemical (as mass and concentrations) on the water surface, on shorelines, in the water column and in the sediments. The model is three-dimensional, separately tracking surface slicks, entrained droplets or particles of pure chemical, chemical adsorbed to suspended particulates, and dissolved chemical. Processes that are simulated include spreading, transport, dispersion, evaporation-volatilization, entrainment, dissolution, partitioning, sedimentation, and degradation.

The model initializes the spilled mass at the location and depth of the release, in a state dependant upon the physical-chemical properties of the material. The state code and solubility are the primary determining factors for the initialization algorithm. If the chemical is highly soluble in water, and is either a pure chemical or dissolved in water (before it is spilled), the chemical mass is initialized in the water column in the dissolved state.

If the chemical is an insoluble liquid or a gas, the following initialization is used. If the density is less than or equal to that of water and the release is at or above the water surface, the model initializes the material in surface slicks. Otherwise, the spilled mass is initialized in the water column at the release depth in a plume volume defined as for the soluble chemicals. Once dissolution has occurred, chemical in the water column is treated as partially adsorbed to suspended sediment particles and partially dissolved. Partitioning



between these states is assumed to be in constant proportions (based on linear equilibrium theory, using  $K_{oc}$  from the chemical database).

Solids, which are spilled in a particulate form, dissolve and then are partitioned in the water column between dissolved and particulate using equilibrium partitioning theory. This process allows for a stochastic approach to a Mine Drift Scenario.

Chemical mass is transported in three-dimensional space and time, by surface wind drift, other currents, and vertical movement in accordance with buoyancy and dispersion. The model simulates adsorption onto suspended sediment, resulting in sedimentation of material. Stokes Law is used to compute the vertical velocity of pure chemical particles or suspended sediment with adsorbed chemical.

Wind-driven current (drift) is calculated within the fates model, based on hourly wind speed and direction data. Surface wind drift of oil has been observed in the field to be 1-6% of wind speed in directions within 0-30 degrees to the right (in the northern hemisphere) of the down-wind direction (Youssef and Spaulding, 1993).

The horizontal turbulent diffusion (randomized mixing) coefficient normally ranges from 1-10  $m^2/sec$  in coastal and marine waters. The vertical turbulent diffusion (randomized mixing) coefficient is typically 0.0001-0.001  $m^2/sec$ . These are reasonable values based on Okubo (1971).

For surface slicks, the model estimates surface spreading, slick transport, entrainment into the water column, and evaporation, to determine trajectory and fate at the surface. Spreading is simulated using the algorithm of Fay (1971). Entrainment is modeled as for oil, using data in Delvigne and Sweeney (1988). Surface slicks interact with shorelines, depositing and releasing material according to whether the material is sticky and to shoreline type. The algorithms used are those developed for oil spills, as described in French et al. (1999).

Volatilization from the water column is calculated from the chemical's vapor pressure and is a strong function of temperature. Degradation is estimated assuming a

constant rate of "decay" specific to the environment where the mass exists (i.e., atmosphere, water column or sediment).

The fates model computes, in space and time, the following: (1) area covered by surface slicks, (2) radius and thickness of surface slicks, (3) total concentration in the water column, (4) dissolved concentration in the water column, (5) area and length of shorelines contaminated, (6) mass per unit area on the shorelines. These model output data are mapped by the user interface in an animated display.

### **3. Environmental Data**

A geographical database supplies data for water depth, shoreline type, sediment type, habitat type, and ice cover throughout the domain. The geographical area around the spill site is gridded using the shoreline location to define land and water cells.

The user supplies an hourly wind time series specific to the time and location of the spill. For this research, 10m (surface) winds from COAMPS were utilized. This data is important for insoluble floating chemicals, but has little influence on dissolved contaminants.

The chemical transport model is designed so that it may accept current (hydrodynamic) data from a variety of sources. For this research, surface currents from SWAFS were utilized.

### **4. Stochastic Model**

The probability of impact from a chemical discharge is quantified using ASA's three-dimensional stochastic model in CHEMMAP<sup>TM</sup>. In the stochastic model, many runs are made for each release scenario and location. Using a historical wind and current record for a location, the model randomizes spill date, and thus the wind and current conditions selected for the run. In this way, historically observed environmental conditions are sampled. The spill volume may also be randomized. An effects endpoint is selected based on toxicity data, which provides a threshold above which probabilities and expected concentrations are reported.

Model output includes maps of chemical: (1) mass or volume on the water surface, (2) mass or volume on shorelines, and (3) particulate concentration in the water, (4) dissolved concentration in the water.

Five statistics are produced for each location (cell) in the model grid. These are displayed in contour maps, which may be overlaid on maps of receptors of concern. Statistics on all model runs may be viewed in total (as probabilities or maximum exposures) or individually. The outputs are: (1) probability of (any) amount exceeding the threshold passing that location, (2) time when amount first exceeds the threshold at the location, (3) mean expected maximum mass or concentration at the location (i.e., peak exposure in time and for mean environmental conditions), (4) worst-case (maximum possible) amount that could hit a location (i.e., peak exposure in time and maximum of all runs under all environmental conditions), and (5) start date and time for run producing the worst case at the location.

An assessment of potential operational risks may be based on these modeling results. The mean expected and worst-case exposure concentrations can be compared to effects endpoints of interest. The worst-case spill for any given location may be evaluated in more detail. The stochastic model identifies the conditions that constitute a worst case. That scenario may then be run with the (single scenario) chemical fates model to obtain animated displays of concentrations over time. These fates results may be input to the biological effects model to quantitatively estimate impacts.

THIS PAGE INTENTIONALLY LEFT BLANK

## IV. MATHEMATICAL AND STATISTICAL ANALYSIS

Before one can talk about analyzing the data, the methods involved to analyze the data must be described. Both outputs of SWAFS and COAMPS had to be evaluated separately. Simple statistical methods, such as mean and variance, are utilized to characterize overall properties of the Northern Persian Gulf; however, to get an idea of the general flow and predominant features a more complex method had to be used. An Empirical Orthogonal Function (EOF) method is used to find temporal-spatial variability. This method is similar to Principal Component Analysis (PCA) in statistics. The following sections will describe these methods and will break down how these methods are calculated.

### A. BASIC MATHEMATICS AND STATISTICS

One of the most basic statistical methods is to calculate the arithmetic mean, which is often simply called the mean or average. The mean is the sum of all the values divided by the total number of values, as in the following equation:

$$\bar{x} = \frac{(x_1 + x_2 + x_3 + \dots + x_n)}{n} = \frac{\sum_{i=1}^n x_i}{n} \quad (4.1)$$

There two main methods of using the mean that were used in this research. One was to use the mean to calculate the perturbation, or ‘prime’ values. This is done by applying  $u = \bar{u} + u'$ . This method will be used when calculating the EOFs. The other method was used to get a general idea of flows in the Northern Persian Gulf. The scale of the flow and general character of the flow was examined using this method.

In addition to the mean and average, discussed early, two statistical methods are utilized. These methods include standard deviation and covariance. Standard deviation of a probability distribution is defined as a measure of the spread of those values. It is also the square root of variance. Mathematically, standard deviation is defined as

$$s = \sqrt{\frac{\sum_{i=1}^n (X_i - \bar{X})^2}{(n-1)}} \quad (4.2)$$

Standard deviation is the most common measure of statistical dispersion, measuring how widely spread the values in a data set. If the data points are close to the mean, then the standard deviation is close to zero. As the data points move farther away from the mean, the standard deviation moves farther from zero. The other statistical method, covariance, is the measure of how much two variables vary together. This is different from variance, mentioned early, which measures how much a single variable varies.

Covariance is computed by

$$\text{cov} = \frac{\sum_{i=1}^n (X_i - \bar{X})(Y_i - \bar{Y})}{(n-1)} \quad (4.3)$$

for two variables  $X$  and  $Y$ . If two variables tend to vary together then the covariance between the two variables will be positive. On the other hand, if when one of them is above its expected value, the other variable tends to be below its expected value, then the covariance between the two variables will be negative. If the variables vary independent from each other, the covariance will be zero. Conversely, if the covariance is zero, the variables need not be independent.

Another important mathematical method involves matrix algebra. Specifically the covariance matrix and eigenvectors/eigenvalues of a given matrix will be discussed. If the data set has more than 2 dimensions, there is more than one covariance measurement that can be calculated. A useful way to account for the additional variances associated with each dimension is to create a covariance matrix. This matrix is composed of the covariances between elements of a vector. A covariance matrix of three dimensions would look like

$$C = \begin{pmatrix} \text{cov}(x, x) & \text{cov}(x, y) & \text{cov}(x, z) \\ \text{cov}(y, x) & \text{cov}(y, y) & \text{cov}(y, z) \\ \text{cov}(z, x) & \text{cov}(z, y) & \text{cov}(z, z) \end{pmatrix} \quad (4.4)$$

Some points to note: Down the main diagonal, the covariance value is between the same dimensions. These values are the variances for the given dimension. The other point is that since  $\text{cov}(a,b) = \text{cov}(b,a)$ , the matrix is symmetrical about the main diagonal.

Eigenvectors are a special case of multiplying two matrices together. There are two key properties of all eigenvectors. First, all eigenvectors multiplied by a scalar are equal, since all the scalar does is make the vector longer but not change its direction. Secondly, all eigenvectors of a matrix are perpendicular, i.e. at right angles to each other, no matter how many dimensions one has. Mathematically another term for perpendicular is orthogonal. This is important because it means the data can be expressed in terms of these perpendicular eigenvectors, instead of expressing them in terms of the x and y axes. Another important thing to know is that when eigenvectors are found it is common to find those whose length is exactly one. This is because the length of a vector does not affect whether it is an eigenvector or not, whereas direction does. So, in order to keep eigenvectors standard, whenever an eigenvector is found it is scaled to have a length of 1, so that all eigenvectors have the same length. Eigenvalues are closely related to eigenvectors. Eigenvectors and eigenvalues always come in pairs. Eigenvalues are the multiple used to get the eigenvector back to the original length it was before being converted to a length of one.

## B. CONVENTIONAL EOF ANALYSIS

Let a temporally and spatially varying scalar variable  $\psi$  be represented by  $\psi(x_i, y_j, \chi_k, \tau_l)$  with  $(x_i, y_j)$  the horizontal grids,  $\chi_k$  the time sequence in months,  $\tau_l = 1, 2, \dots$ , the time sequence in a month. Let  $\bar{\psi}(x_i, y_j, \chi_k)$  be the monthly mean of the scalar. The synoptic anomalies

$$\psi'(x_i, y_j, \chi_k, \tau_l) = \psi(x_i, y_j, \chi_k, \tau_l) - \bar{\psi}(x_i, y_j, \chi_k), \quad (4.5)$$

are re-arranged into a  $N \times P$  matrix,  $\psi'(\mathbf{r}_n, t_p)$ ,  $n = 1, 2, \dots, N$ ; and  $p = 1, 2, \dots, P$ . Here  $N$  is the total number of the horizontal grid points and  $P$  is the total number of time points used for computing the covariance matrix. The EOF analysis widely used in

oceanographic and meteorological research (e.g., Weare et al., 1976; Richman, 1986; Chu et al., 1997 a, b) is the same as the principal component (PC) analysis (Hotelling, 1933) in the statistics community. PCs are the amplitudes, which are functions of time, of their corresponding EOFs. These EOFs can be found by calculating the unitary eigenvectors of the covariance matrix associated with the sample data field. EOF analysis separates the data sets into eigenmodes. Generally speaking, each mode has an associated variance, dimensional spatial pattern, and non-dimensional time series. The  $N \times N$  spatial covariance matrix is calculated by

$$\mathbf{R} = \begin{bmatrix} R_{11} & R_{12} & \dots & R_{1N} \\ R_{21} & R_{22} & \dots & R_{2N} \\ & & \dots & \\ R_{N1} & R_{N2} & \dots & R_{NN} \end{bmatrix}, \quad R_{nm} = \frac{1}{P-1} \sum_{p=1}^P \psi'(r_n, t_p) \psi'(r_m, t_p), \quad (4.6)$$

where  $n$  and  $m$  (1, 2, ...,  $N$ ) denote the grid locations. The diagonal elements of the covariance matrix  $\{R_{nn}\}$  are the variance at location  $\mathbf{r}_n$ . The off-diagonal elements are the covariance with spatial lag equal to the difference between the row and column indices. This symmetric matrix has  $N$  real eigenvalues  $\lambda_\alpha$ , and eigenvectors  $\phi_\alpha(\mathbf{r}_n)$ , such that

$$\sum_{j=1}^N R_{ij} \phi_\alpha(\mathbf{r}_j) = \lambda_\alpha \phi_\alpha(\mathbf{r}_i), \quad i = 1, 2, \dots, N. \quad (4.7)$$

The eigenvectors  $\phi_1(\mathbf{r}_i)$ ,  $\phi_2(\mathbf{r}_i)$ , ...,  $\phi_N(\mathbf{r}_i)$  are called EOFs. Each of them is an  $N$ -point field showing anomaly pattern. The eigenvalues,  $\lambda_\alpha$  ( $\alpha = 1, 2, \dots, N$ ), are all positive and the summation of them,  $\sum_{\alpha} \lambda_\alpha$ , equals the total variance. Therefore,  $\lambda_\alpha$  is considered as the portion of total variance ‘explained’ by the EOF  $\phi_\alpha(\mathbf{r}_n)$ . It is convenient to label the eigenfunctions  $\phi_\alpha(\mathbf{r}_n)$  so that the eigenvalues are in descending

$$\lambda_1 > \lambda_2 > \dots > \lambda_N \quad (4.8)$$

The data matrix,  $\psi'(\mathbf{r}_n, t_p)$ , is thus approximately written by



$$\psi'(\mathbf{r}_n, t_p) = \sum_{\alpha} PC_{\alpha}(t_p) \phi_{\alpha}(\mathbf{r}_n), \quad (4.9)$$

where  $PC_{\alpha}(t_p)$  is the principal component with the same unit as the scalar  $\psi$  and a size of  $P$ , representing the temporal variation of the associated spatial pattern described by EOF  $\phi_{\alpha}(\mathbf{r}_n)$ .

### C. COMPLEX EOF ANALYSIS

Consider a two-component variable such as the horizontal velocity vector  $(u, v)$ . A complex field can be constructed by

$$w = u + iv, \quad i = \sqrt{-1}. \quad (4.10)$$

Similar to the previous section, let a temporally and spatially varying complex field  $w$  be represented by  $w(x_i, y_j, \chi_k, \tau_l)$  with  $(x_i, y_j)$  the horizontal grids,  $\chi_k$  the time sequence in months,  $\tau_l = 1, 2, \dots, n$ , the time sequence in a month. Let  $\bar{w}(x_i, y_j, \chi_k)$  be the monthly mean of the scalar. The synoptic anomalies

$$w'(x_i, y_j, \chi_k, \tau_l) = w(x_i, y_j, \chi_k, \tau_l) - \bar{w}(x_i, y_j, \chi_k), \quad (4.11)$$

are re-arranged into a  $N \times P$  matrix,  $w'(\mathbf{r}_n, t_p)$ ,  $n = 1, 2, \dots, N$ ; and  $p = 1, 2, \dots, P$ . Here  $N$  is the total number of the horizontal grid points and  $P$  is the total number of time points used for computing the covariance matrix.  $N \times N$  spatial covariance matrix is calculated by

$$\mathbf{R} = \begin{bmatrix} R_{11} & R_{12} & \dots & R_{1N} \\ R_{21} & R_{22} & \dots & R_{2N} \\ & & \dots & \\ R_{N1} & R_{N2} & \dots & R_{NN} \end{bmatrix}, \quad R_{nm} = \frac{1}{P-1} \sum_{p=1}^P w'^*(r_n, t_p) w'(r_m, t_p), \quad (4.12)$$

where the superscript ‘\*’ denotes the transpose. The diagonal elements of the covariance matrix  $\{R_{nn}\}$  are the variance at location  $\mathbf{r}_n$ . The covariance matrix  $\mathbf{R}$  is a Hermitian, so the eigenvalues  $\{\lambda_{\alpha}\}$  are positive real numbers whereas the EOFs  $\{\phi_{\alpha}(\mathbf{r}_n)\}$  are complex,

$$\sum_{j=1}^N R_{ij} \phi_{\alpha}(\mathbf{r}_j) = \lambda_{\alpha} \phi_{\alpha}(\mathbf{r}_i), \quad i = 1, 2, \dots, N. \quad (4.13)$$

Each of the complex EOFs  $\phi_1(\mathbf{r}_i)$ ,  $\phi_2(\mathbf{r}_i)$ , ...,  $\phi_N(\mathbf{r}_i)$  them is an  $N$ -point field showing anomaly velocity vector pattern. The eigenvalues,  $\lambda_\alpha$  ( $\alpha=1,2,...,N$ ), are all positive and the summation of them,  $\sum_\alpha \lambda_\alpha$ , equals the total variance. Therefore,  $\lambda_\alpha$  is considered as the portion of total variance ‘explained’ by the EOF  $\phi_\alpha(\mathbf{r}_n)$ . It is convenient to label the eigenfunctions  $\phi_\alpha(\mathbf{r}_n)$  so that the eigenvalues are in descending

$$\lambda_1 > \lambda_2 > \dots > \lambda_N. \quad (4.14)$$

The data matrix,  $w'(\mathbf{r}_n, t_p)$ , is thus approximately written by

$$w'(\mathbf{r}_n, t_p) = \sum_\alpha r_\alpha(t_p) \exp[i\theta_\alpha(t_p)] \phi_\alpha(\mathbf{r}_n), \quad (4.15)$$

where  $[r_\alpha(t_p), \theta_\alpha(t_p)]$  are the temporally varying amplitude (positive) and phase (between  $-180^\circ$  and  $180^\circ$ ) associated spatial pattern described by EOF  $\phi_\alpha(\mathbf{r}_n)$ .

## **V. MINE WARFARE (MIW)**

Sea mines have been important in naval warfare throughout history and continue to be so today. Originally called a torpedo, mines have caused major damage to naval forces, slowed or stopped naval actions and commercial shipping, and forced the alteration of strategic and tactical plans. The threat posed by sea mines continues, and is increasing, in today's world of inexpensive advanced electronics, nanotechnology, and multiple potential enemies, some of which are difficult to identify. The largely unregulated sale of sea mines by allies and third parties is contributing directly to this growing threat.

Because of the low cost and wide availability of modern sea mines, the importance as a threat to shipping and naval force operations is growing rapidly. The threat continues to increase as the U.S. naval forces operate increasingly in the world's littorals. The Navy is responsible for protecting all maritime forces, including logistics transport and Marine Corps units, against the mine threat wherever it may be encountered, from the sea lanes, to logistics unloading areas, to the high-water mark on the landing beaches.

Naval mines can be used strategically, channeling or denying passage through restricted waters and in and out of ports needed for sustenance by littoral nations. Mines can shape the naval battlespace, the approaches to it, and routes of commerce, thus setting the conditions of a campaign. Used tactically, they can slow or stop movement to and through narrow straits and to landing zones on beaches, and in so doing can also make a slowed or stopped force more vulnerable.

The breakup of the Soviet Union, with its enormous stockpile estimated at nearly half a million sea mines, has resulted in the potential widespread availability of mines. A vintage World War I mine was able to inflict \$96 million worth of damage to the USS Samuel B. Roberts (FFG 58) in the Persian Gulf (Zwolski, 1998). There were several other instances in the late 1980's of drifting mines being deployed around shipping lanes in the Persian Gulf region. In fact 75 percent of damage to U.S. Navy capital ships from

1988 to 1998 came from mines, two of which were World War I technology (Zwolski, 1998). Subsequently, mines have gained the reputation as the least expensive, yet most effective, offensive and defensive weapon of war. The threat is still there today.

In the current threat environment, a mine attack on the economic lifeline of Iraq is anything but impossible. Since the thesis is unclassified, it is not permitted to use elements, which would be used in the case of an actual attack; however using a simple drifter can give a good impression of the vulnerabilities to a drifting mine attack.

## VI. CHEMICAL POLLUTANTS

In the current threat environment, a chemical attack on the economic lifeline of Iraq is anything but impossible. Since the thesis is unclassified, the chemicals were chosen due to abundance in the region and do not necessarily have any elements which would be used in the case of an actual weapon with mass destruction (WMD) attack. These chemicals were also chosen because of their high toxic elements. For this reason, the choices are Ammonia and sulfur mustard.

### A. AMMONIA

Ammonia,  $\text{NH}_3$  or  $\text{NH}_4^+$ , is prepared commercially in vast quantities, with major uses of Ammonia and its compounds being fertilizer and refrigerant and in the production of other chemicals. With the rise in natural gas prices, fertilizer production has shifted to areas with cheaper natural gas prices. One of these areas is the Persian Gulf region. As fertilizer production increases in the Persian Gulf so too must the shipment of ammonia. Even in the best case scenario, increase the amount that is shipped increases the chances of an Ammonia spill within the Persian Gulf region.

Ammonia is a clear colorless gas with a strong odor. Although Ammonia gas is lighter than air, vapors from a leak initially hug the ground (ASA's Database). It is shipped as a liquid under its own vapor pressure. Its density in the liquid form is  $12.8825 \text{ kg/m}^3$ . Contact with the unconfined liquid can cause frostbite. Gas generally regarded as nonflammable but does burn within certain vapor concentration limits and with strong ignition. Fire hazard increases in the presence of oil or other combustible materials.

It is extremely soluble in water; one volume of water dissolves about 1,200 volumes of the gas at  $0^\circ\text{C}$  (90 grams of Ammonia in 100 cc of water), but only about 700 volumes at room temperature and still less at higher temperatures (Ammonia, 2007). Ammonia can be tasted in water at levels above about 35 mg/liter. Odor thresholds have been variously reported according to the definition used and technique of measurement. Most people can identify Ammonia in air at about  $35 \text{ mg/m}^3$  and can detect it at about one-tenth of this level.

Ammonia is a floater, highly volatile, highly soluble and slightly absorbable to particles, and reacts exothermically with all acids. Violent reactions are possible. It also readily combines with silver oxide or mercury to form compounds that explode on contact with halogens. When in contact with chlorates, it forms explosive ammonium.

As for toxicity, Ammonia is immediately dangerous to life or health indicator (IDLH) is relatively small (300 ppm), its short term exposure limit (STEL) is 35 ppm and its odor threshold is 0.019 ppm. Its degradation rate is 0.1586 in both air and water. Contact with Ammonia could cause skin and eye burns and inhalation some burning sensation, cough, shortness of breath and sore throat. For the ecosystem, its slight toxicity can be lethal to shrimp, prawns, salmon, trout and catfish.

## **B. SULFUR MUSTARD / MUSTARD GAS**

Sulphur mustards, of which Mustard Gas is a member, were first used as a chemical warfare agent effectively World War I by the German army against Canadian soldiers in 1917 (Sidell, et al, 1998). Mustard Gas is chemically called beta-chloroethyl sulphide ( $C_4H_8Cl_2S$ ) and has the ability to form large blisters on exposed skin. The affect of blistering puts Mustard Gas in a subcategory of chemical agents called blister agents. This blister agent is very popular and has since been used repeatedly over the years. This includes: Iraq against Iran in 1981 and 1983-1988, Iraq against Iraq in 1987-1988 and Iraq against Kurd in 1988 (CBWInfo.com Factsheets, 2007). The use of poison gas, including Mustard Gas, during warfare was prohibited by the Geneva Protocol of 1925 and the subsequent Chemical Weapons Convention of 1993, which also prohibited the development, production and stockpiling of such weapons (CBWInfo.com Factsheets, 2007).

Despite the existence of more highly effective chemical warfare agents that are more toxic, Mustard Gas has not lost its usefulness because of its special characteristics. It is very toxic and difficult to treat, versatile, persistent, cheap, easy to produce, and difficult to protect against. Furthermore, sulfur mustard is toxic as droplets, liquid and vapor. Due to the simple and inexpensive synthesis, as well as physical properties, it has the potential of being one of the leading threats from both terrorist and military sources (Vidan, 2002).

Pure sulfur mustard is a colorless, viscous liquid with a slight odor of castrol oil at room temperature, whereas when used as a chemical agent it is typically a dark yellow-brown liquid with an odor typically described as mustard, horseradish or garlic (Vidan, 2002). Sulfur mustard is barely soluble in water, 0.07% at 10°C, and very soluble in organic solvents, fuels and lubricants (Vidan, 2002). In aqueous solutions, mustard agent decomposes into non-poisonous products by means of hydrolysis. This reaction is catalyzed by alkali. However, only dissolved mustard agent reacts, which means that the decomposition proceeds very slowly.

Sulfur mustard is a potent alkylating agent, readily penetrating the skin, mucus membranes and the eyes, which are the most sensitive (Vidan, 2002). Most victims sustain non-fatal but disabling injuries, mostly to the eyes, respiratory tract and skin. Ocular injuries appear in 75±90% of all Mustard Gas casualties, with reports of delayed ocular morbidity appearing years later (Vidan, 2002). Since Mustard Gas primarily disables, vice kills, for every individual affected, on average, another must be utilized to tend to the affected individual. This will further reduce the number of personnel available to complete a given mission, making it a very effective chemical agent.

Since density of sulfur mustard is greater than water. Therefore, in an aquatic environment the primary delivery of pure sulfur mustard will be from the air. To use it as a chemical agent, sulfur mustard will be disseminated using aerial sprays or munitions and will be initially in the form of droplets. These droplets would be subject to gravitational settling. Sulfur mustard vapor from resulting deposits may reenter the atmosphere by evaporation. In the atmosphere, sulfur mustard vapor will degrade primarily by reaction with photochemically produced hydroxyl radicals; the resulting half life being estimated as 1.4 days (Spectrum Fact Sheet, 2007).

When sulfur mustard is introduced into water at very low concentrations so that it is dissolved, it will rapidly hydrolyze. At 25°C, the estimated half-live of sulfur mustard when dissolved in large amounts of water are 4 minutes (Spectrum Fact Sheet, 2007). Volatilization will be slow by comparison. Hydrolysis in seawater will be a factor of 2.5 slower because of the common-ion effect exerted by the chloride ion (Spectrum Fact

Sheet, 2007). Despite its high rate of hydrolysis, sulfur mustard that has not dissolved may persist for longer periods of time because its rate of solution is slow.

When sulfur mustard is introduced into seawater in higher concentrations, three zones with different behavior are observed (Spectrum Fact Sheet, 2007). A small amount of sulfur mustard will remain on the surface in a surface film where it will be destroyed by hydrolysis and to some extent volatilization; this surface film may last from one to several days. Bulk sulfur mustard, or droplets formed by wind action on the surface film, will sink to the bottom of the water because sulfur mustard is heavier than water. This sulfur mustard will be degraded by hydrolysis; however, the hydrolysis rate will essentially be the rate of dissolution. The rate of dissolution will depend on the exposed surface, the amount of agitation, and the temperature. In the water column of a body of seawater, dissolved sulfur mustard will be lost by hydrolysis with its half-life being around 15 min at 25°C (Spectrum Fact Sheet, 2007).

Disposal by sea burial might result in releases of large quantities of sulfur mustard. When bulk quantities of sulfur mustard are disposed of at sea, some of it will form a surface film that will disappear as a result of hydrolysis and volatilization within several days (Spectrum Fact Sheet, 2007). Most of the sulfur mustard will sink to the bottom of the water because it is heavier than water. This sulfur mustard will be degraded by hydrolysis; however, the hydrolysis will be limited by the rate of dissolution. The rate of dissolution will depend on the exposed surface, the amount of agitation, and the temperature.



## **VII. ANALYSIS OF PHYSICAL MODEL OUTPUT**

Datasets were collected via two different operational models, COAMPS and SWAFS. The following discussion will examine: (1) where the data came from, (2) how it was collected, (3) what methods were used to process it, both spatially and temporally, and (4) how the two datasets compared to each other at a specific geographical reference.

### **A. PHYSICAL MODEL OUTPUT**

#### **1. Currents**

The currents dataset was retrieved from the Operational run of SWAFS. This model is run once daily at Navy Oceanographic Office (NAVO) located at Stennis Space Center near Bay St. Louis Mississippi. The model is run with a 24 hour hindcast and a 48 hour forecast. Personnel at the NAVO removed data every hour from the first day of the forecast portion of the model and stitched these Tau's together into month long datasets. The data for currents was split into monthly intervals due to the size of the data involved. On average, one month worth of currents equaled 450 mb of data. If the data had been collected in one long dataset it would have been several gigabytes in size. This in turn would have created issues with transferring it to the Naval Postgraduate School and in analyzing the data. The area is from 23.5°N to 30.5° N and 47.5°E to 57.5°E. The horizontal resolution of the operational model was 2 km. The data was retrieved in hourly intervals from February through July 2006. Each hour field contained both *U* and *V* components of 0.5 m deep currents, referred to hereafter as currents. There were a few days that the data was either not collected or was erroneous. This data was removed during the data analysis process and replaced with the mean calculated from the rest of the dataset.

#### **2. Winds**

The wind dataset was retrieved from the Operational run of COAMPS. This model is run operationally with incremental updates throughout each day from Fleet Numerical Meteorology and Oceanography Center (FNMOC) in Monterey California. The model is run with a 24 hour hindcast and a 48 hour forecast. Personnel at the NAVO removed data every 6 hours from the first day of the run and stitched these Tau's together

into a six month long dataset. The area is from 23.5°N to 30.5° N and 47.5°E to 57.5°E. The horizontal resolution of the operational model was 27 km. The data was retrieved in six hour intervals from February through July 2006. Each six hour field contained both  $U$  and  $V$  components of 10 m winds, commonly referred to as surface winds and hereafter as just winds. There were a few days that this could not be accomplished or the data collected was bad. This data was removed during the data analysis process and replaced with the mean calculated from the rest of the dataset.

The maximum wind speed observed during the entire period near the oil terminals was 10 m/s. Based on climatology, and Figure 7, this value appears to be low. During Shamal events winds can reach up to 50 kts, or 25 m/s. Since several Shamals are likely to have occurred over a six month period it is extremely unlikely that these events never created winds in excess of 10 m/s. The fact that the models do not include wind gusts is likely a factor. However, this would only remove the more extreme events and winds of greater than 10 m/s are likely to have occurred. The reason values greater than 10 m/s are still not observed can be explained by the temporal resolution. The wind fields are extracted every six hours, so events that occur between these periods are not observed in model outputs. This limiting factor must be taken into account during operational planning and the examination of the model data in this thesis.

## **B. DATA PROCESSING**

Once the data had been collected and formatted for transfer, it was sent to the Naval Postgraduate School for analysis and the currents were also sent to ASA. Once ASA received the currents data, they formatted them to be compatible with ChemMap<sup>TM</sup> and sent the formatted data on to Naval Postgraduate School for use in the thesis. Once the datasets were received, analysis and processing began. The primary method of analyzing the data was using different methods available within MATrix LABoratory (MATLAB). MATLAB is a mathematical software package developed by Mathworks.

The mathematical and statistical analysis explained earlier will be made in this section. Of note, EOF calculations become increasingly computationally expensive as the dimensions of the variables get larger. Beyond very small matrixes computers are required to calculate EOFs. As with the data in this study, the computer sometimes

becomes the limiting factor. Subsequently, sometimes the dimensions of the dataset, either spatially, temporally or both, had to be decreased in order to complete the calculation. Since the data provided for currents was the larger and therefore more difficult dataset to analyze, most of this section will focus on currents. The wind dataset was analyzed with few differences from that of currents. The differences between winds and currents will be discussed after all methods for analyzing currents have been mentioned.

Since the current fields included both data in the water and place holders for land, the first step in the analysis was to determine which data was associated with land and which data was associated with water, and therefore currents. Once this was accomplished the data associated with land could be converted to a variable that would not interfere with calculations. This was done via two methods. The first method was to assign the land data a value of 'NaN', short for 'Not a Number'. By doing this step when a spatial plot was required no values would be placed on land. The other method utilized was to create an index matrix of all data associated with currents. By doing this, the data associated with currents could be extracted and analyzed without land values interfering.

After the land data was removed, the monthly data sets were combined to form one time series. Due to the amount and size of data collected, the dimensions of the data set had to be reduced. The first dimension that was reduced was the overall spatial dimension. Since the area that was being analyzed was determined to be a low energy area from Reynolds (1993), the dataset dimensions were decreased to a box with dimensions:  $27.5^{\circ} N$  to  $30.5^{\circ} N$  ;  $47.5^{\circ} E$  to  $51^{\circ} E$  . This box was entirely in the low energy area thereby allowing for the study of this regime.

Focusing solely on the Northern Persian Gulf greatly reduced the size of the data; however to complete the EOF calculations the dataset had to be reduced further. Instead of analyzing every data point spatially, it was determined that retrieving every other data point still provided much greater resolution than the wind data that it would eventually be compared to, yet still was able to be processed by the available computers. This spacing remained fine enough to detect most eddies or other phenomena that might occur. The

dataset was also reduced temporally. Having hourly data helps when studying tides, however reducing the dataset to every third hour was necessary to be able to compute the EOFs. This reduction in the dataset was primarily used for the EOF calculations. For example, when the time series calculations were done on a location near Iraq's Oil Terminals, the time series included all of the hourly datapoints.

The next step was to see if there was any data that was obviously corrupted. This was accomplished while computations of EOFs were being run. While analyzing the EOFs there was a period, illustrated in Figure 12, which shows extremely different than the rest of the data. This data, corresponding to 18 May, was determined to be erroneous and subsequently replaced by the mean of the remaining data. The mean was used due to the fact that in the EOF calculations the mean would be removed and therefore the data would essentially be zero. It was also noted by NAVO scientists that the data associated with 23 June was missing due to computer problems on that day. The mean of the data was inserted into this date for the reasons discussed earlier. These two periods were removed from consideration when examining times to run the chemical models.

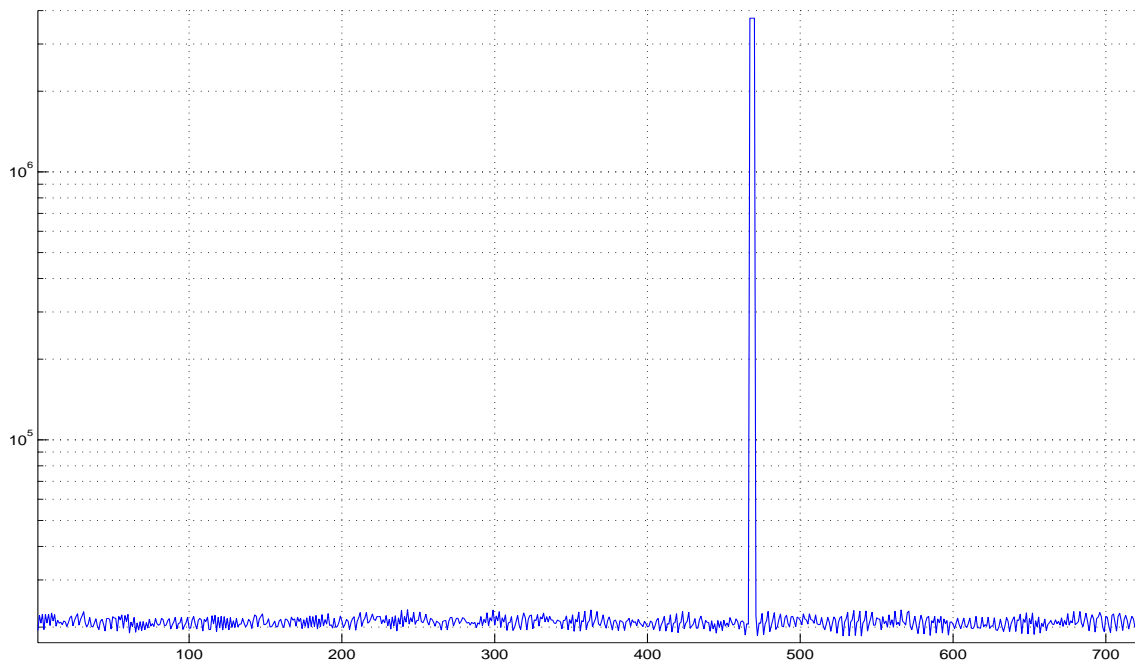


Figure 12. Time Series of EOF Coefficients for the currents of the Northern Persian Gulf on a semi-log y scale.

Once the dataset had been converted into a form that was able to be examined and all days were filled with either actual data or replaced with the mean, analysis of the data could begin. Several goals associated with the analysis includes: (1) examine a time series of a point near the oil terminals to extract times for the model runs, (2) determine how many EOF modes were required to capture the majority of the Northern Persian Gulfs characteristics, and (3) examine the data in a spatial environment to get a feel for primary the amplitudes and directions of currents.

## **C. WINDS**

### **1. Monthly Mean**

Analysis of the wind began with examining the mean wind over the entire time and entire Persian Gulf and progressed to a more detailed analysis of each month's characteristics. The mean wind for the entire time, Figure 13, showed a distinct flow along the major axis. The predominantly northwesterly flow resembles the Shamal (Perrone, 1979). As the flow approached the Straits of Hormuz, it veered towards Iran's coastline. Flow in the Gulf of Oman also tends towards Iran's coast. A likely cause for the flow to turn north in both instances is the al-Hajar mountain range along the Musandam Peninsula. This mountain range would tend to obstruct flow and direct it along the mountain range. The mean flow in Iran tends to flow along the Zagros Mountains. Mean flow to the southwest of the Persian Gulf is weak, with a general direction to the south. As seen in Figure 13, the mean wind speed is less than 5 m/s throughout the Persian Gulf. Near Iraq's oil terminals, the mean wind speed is even weaker, around 2 -3 m/s.

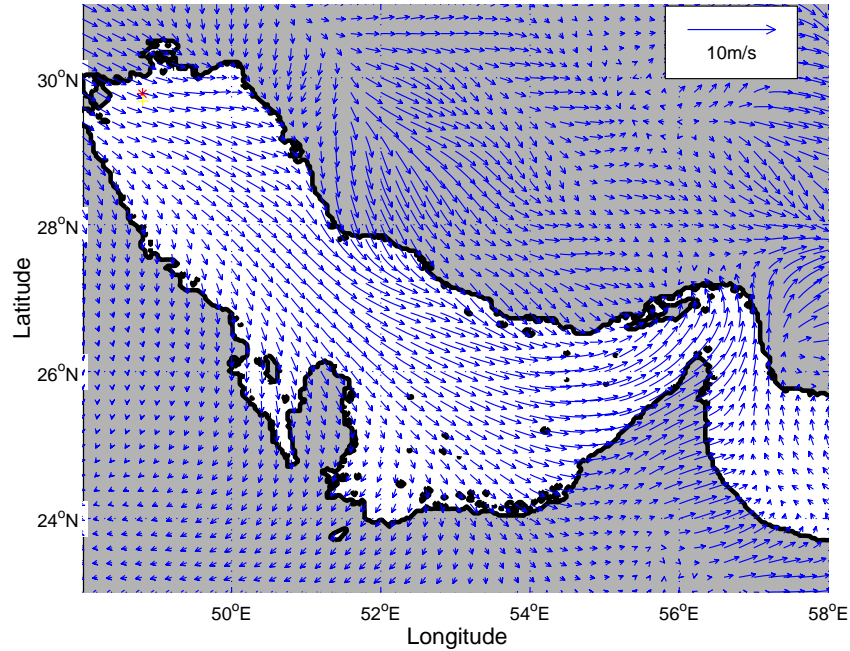


Figure 13. Mean wind vectors of the entire dataset (Feb – Jul).

When looking at the months individually it became clear that the characteristics and magnitudes changed, sometimes drastically, from month to month. From examining February's mean wind field, it is easy to see there is a line that starts near  $28^{\circ}N$   $50^{\circ}E$  and extends along the major axis until it reaches the shore (Figure 14a). This is a line of bifurcation between flow turning towards the Arabian Peninsula and the Asian Continent. There is also distinct area of weak winds surrounding Iraq's oil terminals. As the winds progress down the major axis of the Persian Gulf, their magnitudes tend to increase. This increase may be due to the decreased friction resulting from the winds traveling from land to water and enhancement downslope flow off the Zagros Mountains to the east. Relatively same magnitudes were seen in March; however the flow was slightly different. The region of weak winds near the oil terminals has increased in size, and the primary direction of those winds are now across the major axis (Figure 14b). The line of bifurcation has also migrated. It now extends from the northern tip of Qatar along the major axis to the shore. Flow north of Qatar is predominantly along the major axis with only small deviations away from this continuity.

By April the area near the oil terminals has increased further to the south and an anti-cyclonic pattern is clearly visible (Figure 14c). Besides the increase in the area to the north, the winds over the Persian Gulf showed remarkably little change from March to April. However, this relatively constant regime disappeared in May. As illustrated in Figure 14 d, the magnitudes throughout the region increased significantly, although the pattern only changed in the north. There was no longer an area of weak winds surrounding the oil terminals. The winds predominantly flowed along the major axis and either over the Musandam Peninsula or into the Straits of Hormuz. If the winds traveled into the straits, they ended up drastically decreasing once they encountered the Zagros Mountains. Effects from the Zagros Mountains are also felt throughout the eastern side of the Persian Gulf. It is evident that along this side the Zagros Mountains due to two things. First, they could block the flow and subsequently direct it along the east coast of the Persian Gulf. The other effect is flow coming off the Zagros Mountains. This flow converges with the flow in the Persian Gulf thus enhancing the already stronger flow.

By June, the presence of the Southwest Monsoon in the Arabian Sea is felt in the Gulf of Oman. Flow is no longer away from the Musandam Peninsula, but in from the Arabian Sea (Figure 14e). This flow is not the only significant change. In the region around the oil terminals, which previously was an area of weak winds, there is moderate flow down the major axis. The line of bifurcation no longer exists south of Qatar, being replaced by a new area of weak winds. Flow on the eastern edge of the Persian Gulf shows a strong area of convergence. The coastline now marks where downslope flows from the Zagros Mountains oppose moderate flow from the northern Persian Gulf. With nowhere to go, this area of convergence is also an area of upward vertical motion.

The majority of flow in July is similar to that seen in June. The Gulf of Oman still feels the influence of the Southwest Monsoon and the flow in the northern Persian Gulf is still moderate (Figure 14f). What differs is the area of weak flow just south of Qatar and the direction of flow in the north. The region of weak flow has become virtually nonexistent with the majority of flow now moving towards the Arabian Peninsula. The direction of flow to the north is no longer along the major axis, instead, it has a distinct

across axis portion. This equates to flow reaching the east coast while still in the northern region. Thus the fetch is markedly reduced and there is less time for the magnitude to build.



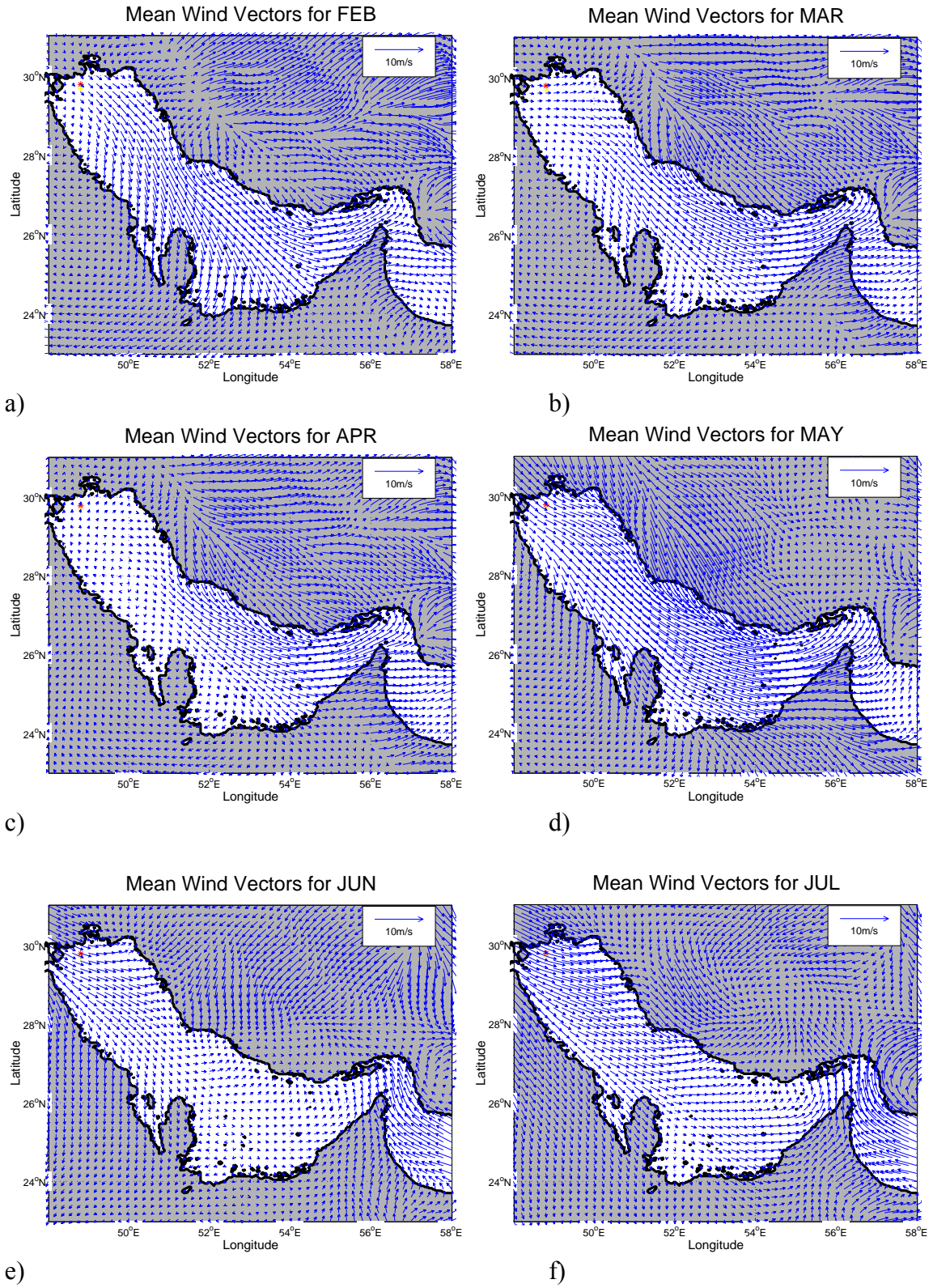


Figure 14. Mean monthly wind vectors.

## 2. Anomalies

Anomalies were primarily examined over the entire record length and in the form of analyzing the first three EOF modes. As mentioned earlier, to get a better picture of the low energy environment examined in this thesis, EOFs were conducted only in the northern Persian Gulf. If the variance calculated during the EOF process is summed up and then each variance is divided by that sum, a percent of total variance is obtained.

$$\% \text{ var}_n = \frac{\text{var}_n}{\sum_{i=1}^n \text{var}_i} \quad (7.1)$$

Since the variance was obtained from computer based EOF calculations, there were a finite number of modes that could be derived from the data. The wind data allowed for a total of 300. From these calculations it was determined, as illustrated in Table 1 below, that the first 3 modes encompassed 88 % of the variance. By the fourth mode the percent of the total variance has decreased drastically and had less significance.

EOF mode	Percent of Total Variance	Cumulative Percent
First Mode	61.1860	61.1860
Second Mode	20.1800	81.3660
Third Mode	6.6906	88.0566
Fourth Mode	3.2760	91.3326
Fifth Mode	1.9524	93.2850

Table 1. Percent of Variance for the first 5 EOF modes of Wind data

Based on the percent variance, the first three EOF modes were analyzed to determine likely forcing. Although these modes were examined, the wind field depicted in them is significantly less than what was examined in the mean wind vector discussion. This is due to the fact that EOFs looked at the perturbations. To get an idea of how large of winds the EOFs produce, take the representative vector from Figure 15 and multiply it by the magnitude scale in Figure 16. When this is done for EOF Modes 1, 2, and 3, the scales are shown to be around 2 m/s, 0.8 m/s, and 0.8 m/s, respectively.

EOF-1 has a relatively strong uniform eastward flow (Figure 15). The angle that this EOF is multiplied by is predominantly close to either 0 degrees or close to 180 degrees (Figure 16). This indicates the primary flow other than the mean is across the gulf. When the angle is close to 0 degrees the flow is like in Figure 15, for 180 degrees the flow is in the reverse direction. This flow likely corresponds to passage of fronts that would allow for higher winds across the gulf. The winds flowing down the gulf are already accounted for in the mean. This conclusion makes more sense when the magnitudes of the winds are also examined. During the winter, February into March, there are higher magnitudes, occurring every few days. The magnitudes then decrease until the next event. This timeframe is consistent with the findings of Perrone, 1979.

The next mode, EOF-2, has a cyclone centered near  $30^{\circ}N$   $48.75^{\circ}E$ . A cull is located at the edge of the area,  $27^{\circ}N$   $50.5^{\circ}E$  (Figure 17). The Magnitude and direction of the coefficients are harder to utilize to determine the rationale behind the circulation. This is because the magnitude does not vary in set intervals and does not vary between only two main directions (Figure 18). The magnitudes have no set interval and cycle between larger and smaller magnitude repeatedly followed by period of small magnitudes. The direction tends to continually change. Based on both the previously mentioned features and the fact that the pattern is cyclonic in nature, this likely the period intensification of a thermal low just landward of the oil terminals. Thermal Lows are known events throughout the region, with the strongest Thermal Lows found in Saudi Arabia and in Iraq (Ackerman and Cox, 1982). The Thermal Lows normally occur onshore, but near the water. This is due to the increased pressure difference created by the heating of the land while the water remains relatively constant.

In EOF-3 there is a line of bifurcation across the Persian Gulf, splitting flow curving to the north and flow curving to the south (Figure 19). When looking at the amplitudes and directions for EOF-3, Figure 20, the primary directions are near 0 degrees and near 270 degrees. Magnitudes are relatively small with the times of large magnitudes correspond to the same periods as those of EOF-1. These times also correspond to migratory lows. Since EOF-3's magnitudes are close to half that of EOF-1, EOF-3 would correspond to residual influences of transiting low pressure systems.

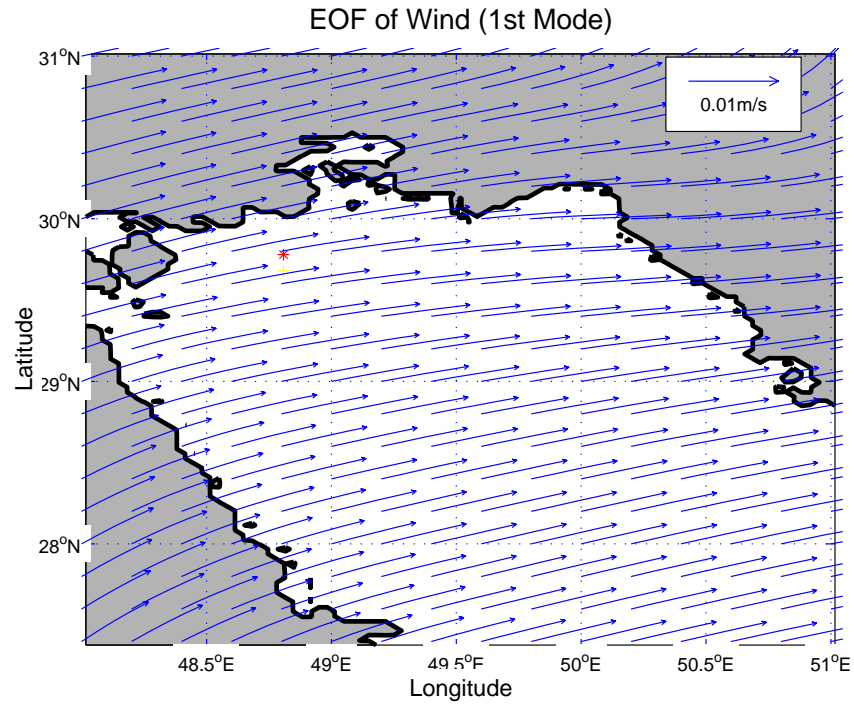


Figure 15. EOF-1 for entire wind dataset in the Northern Persian Gulf.

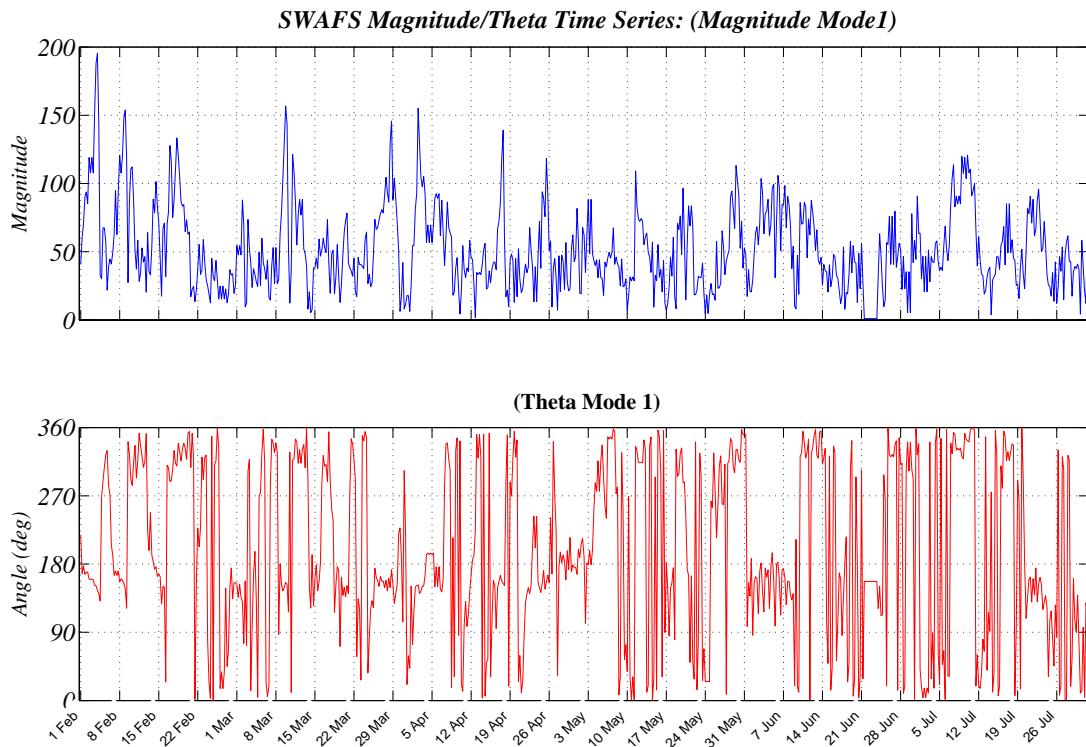


Figure 16. EOF-1 amplitude (top) and direction (bottom) for entire wind dataset in the Northern Persian Gulf.

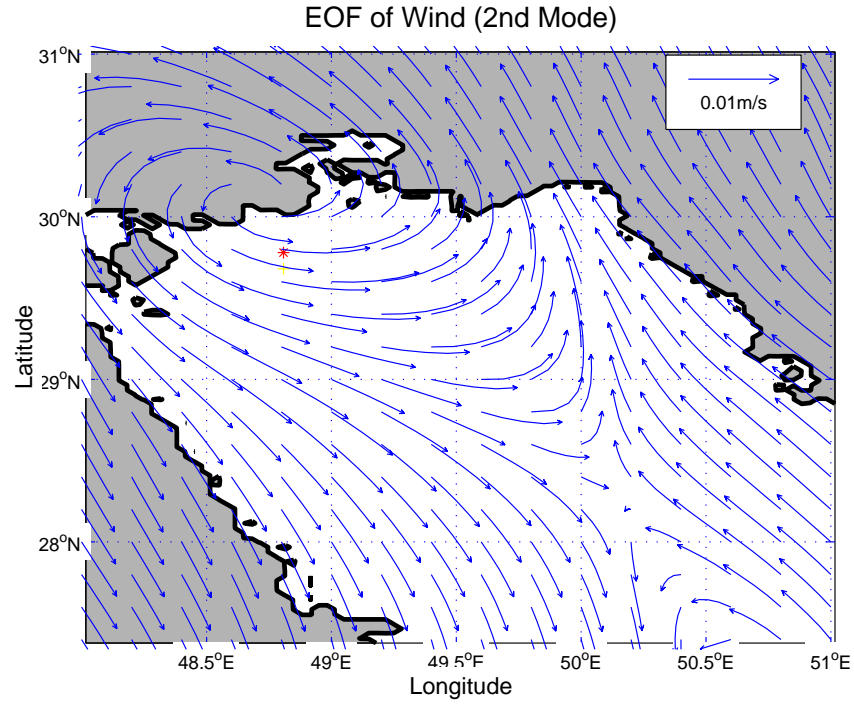


Figure 17. EOF-2 for entire wind dataset in the Northern Persian Gulf.

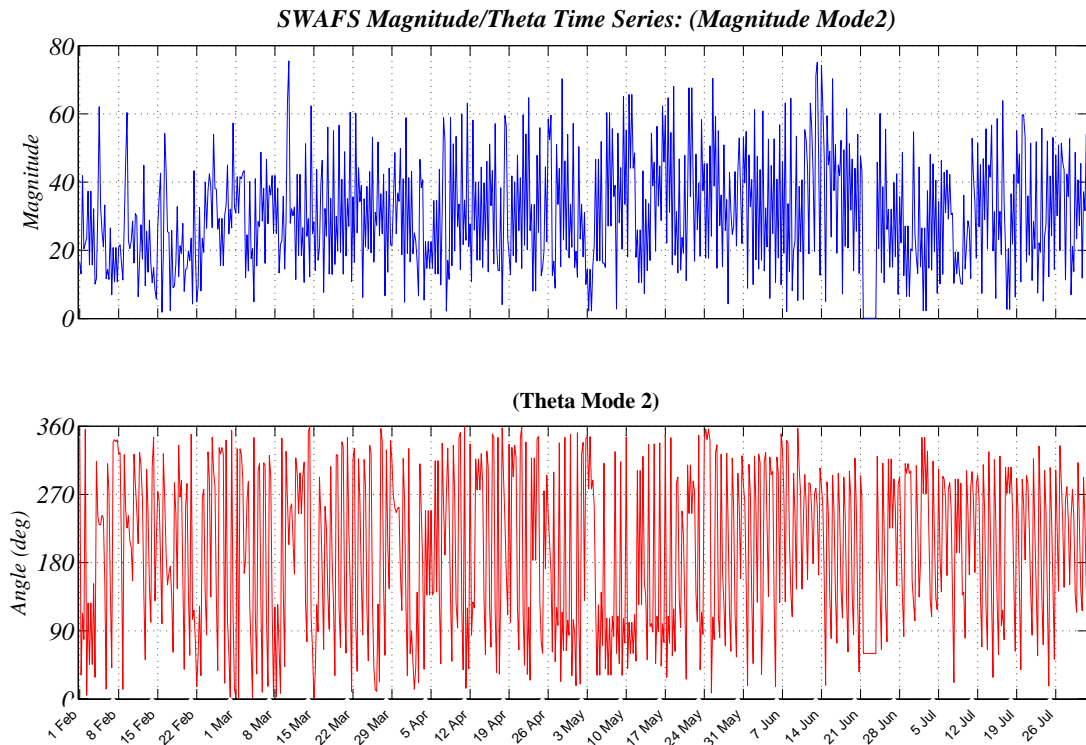


Figure 18. EOF-2 amplitude (top) and direction (bottom) for entire wind dataset in the Northern Persian Gulf.

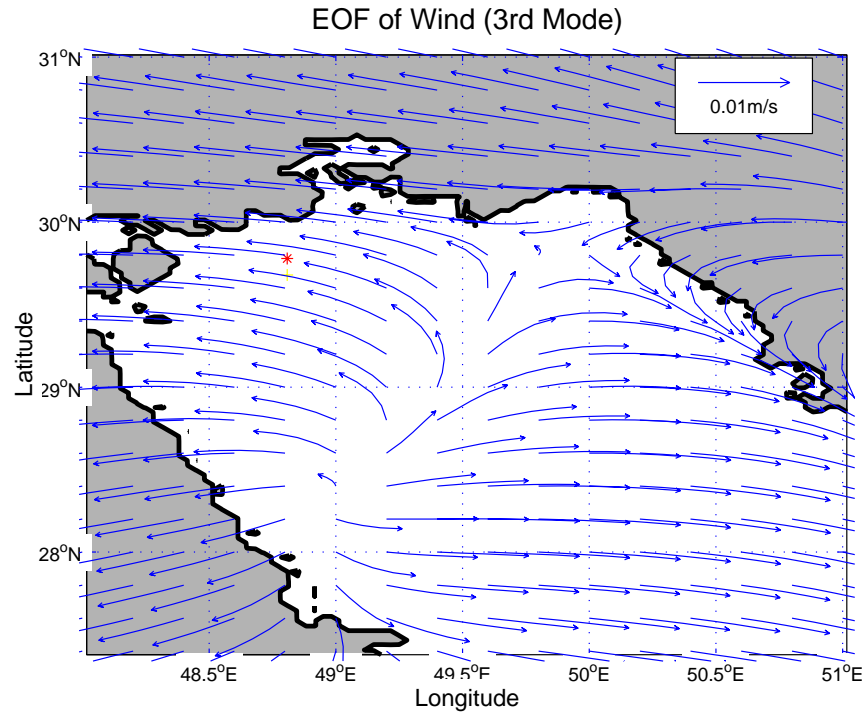


Figure 19. EOF-3 for entire wind dataset in the Northern Persian Gulf.

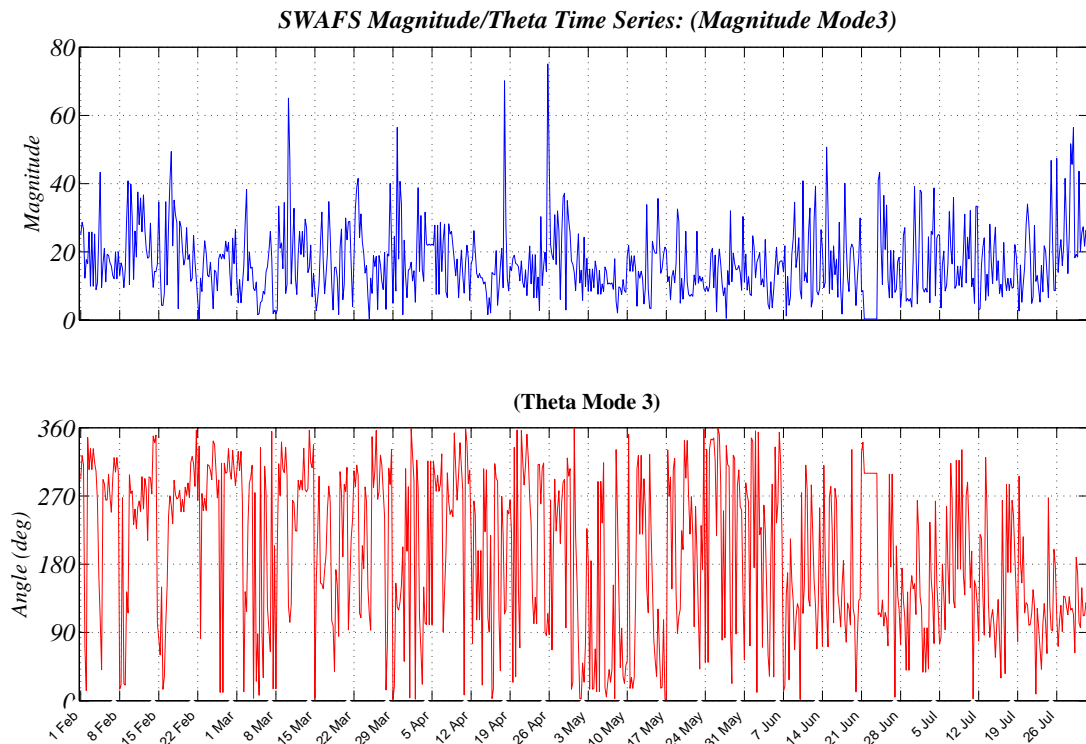


Figure 20. EOF-3 amplitude (top) and direction (bottom) for entire wind dataset in the Northern Persian Gulf.

### 3. Spatial Examining Raw Data

While the mean is widely used, when examining a possible oscillating pattern to determine appropriate times to run the models, the mean gives only a partial view. Maxima at either end of the spectrum are not shown. Therefore, to visually examine the data and focus the research on important periods the mean was not used. To accomplish this, looking at the raw data in time series format was beneficial. This was done in two steps. The first step also accomplished goal two. Specifically, the  $U$  and  $V$  components were converted to polar coordinates. This allowed the magnitudes and directions to be analyzed separately. The magnitudes were a significant factor when determining model run times. Some of the criteria for the scenarios included having a: (1) minimal wind and weak current event, (2) maximum wind and weak current event, (3) maximum wind and maximum current event and (4) looking for some period that a weather phenomena occurred. It could easily be seen when the wind criteria was met by looking at a time series of the magnitude of winds (Figure 21).

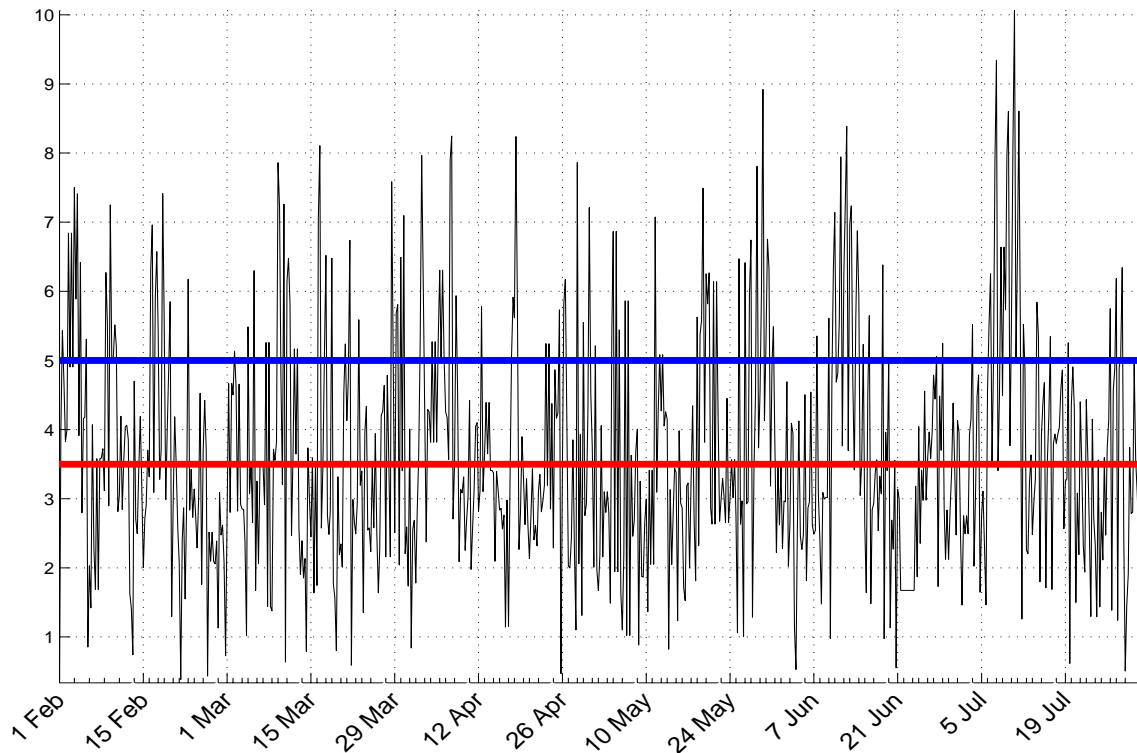


Figure 21. Time Series of the Magnitude of Winds (in m/s). The red line corresponds to maximum value for the definition of weak winds, while the blue line corresponds to the minimum value for strong winds, in this thesis.



Although when the term maximum wind event are used gale force or greater winds are thought of, in the low energy region of the northern Persian Gulf this is not the case. An extreme high wind event was defined, for the purpose of this study, as any time period that consistently exceed 5 m/s. On the opposite spectrum, a low wind event was defined as any time period that consistently was below 3.5 m/s. Maximum wind events occurred primarily later in the time period, with the strongest event occurring in early July. Weak wind events happened less frequently, with the primary event occurring in late February.

#### **D. CURRENTS FOR THE NORTHERN GULF**

The same concept utilized for the wind analysis was applied to the low energy currents regime of interest, the northern Persian Gulf. Although the results from mean currents calculations were the same when calculating the entire gulf or just the northern Persian Gulf, examining the northern region allowed for a better spatial resolution to be displayed.

The mean vector over the entire time period and the monthly mean vector plots appear to show a turbulent flow throughout the northern region (Figures 22 and 23). Keeping in mind that the flow in this region is primarily tidally driven, it could be expected that the mean should be zero, or no flow. Indeed the mean flow is actually very small in magnitude. Notice the reference arrow is 10 cm/s and most of the flows are less than the reference. The mean flow shows preferred paths of flow and not what happens at any one time throughout the given period.

The mean currents for the entire time, Figure 22, show flow north along the Iranian coast, across the gulf and down along the Arabian Peninsula and central gulf. This pattern extends up to  $29.5^{\circ} N$ . North of  $29.5^{\circ} N$  was a region of primarily slow southward flow.



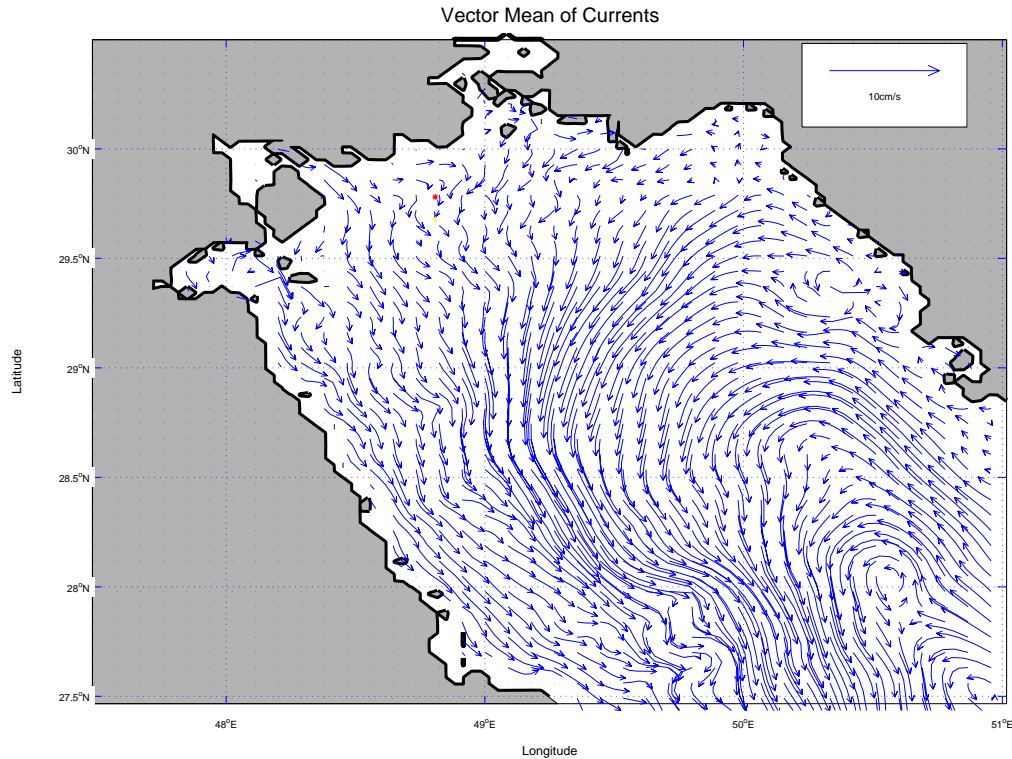


Figure 22. Mean current vectors of the entire dataset (Feb – Jul) Arrow shows a 10 cm/s current.

When looking at the months individually it became clear that the characteristics and magnitudes changed drastically from the first few months to the last months collected. However, every month contained a current running southward near the major axis of the gulf.

From examining February's mean current field, the flow throughout the region is weak and less organized than the mean for the entire time span (Figure 23a). There is a weak flow up the Arabian Peninsula. This flow then turns towards the central region and combines with flow coming from the north and east. This combined flow forms the strongest current for February. This combined flow is the characteristic southward flow observed in every month down the major axis. Flow north of 29°N tends to be very weak, less than 2.5 cm/s.

Approximately the same magnitude was seen in March; while the character of the flow has changed some (Figure 23b). The characteristic southward flow observed in

every month down the major axis begins a little further north. The flow up the Arabian Peninsula has dissipated being replaced by weak southward flow originating in the extreme northwest. There is a commencement of flow up the Iranian coast seen in the mean flow for the entire period; although it is not yet well organized. Flow north of  $29^{\circ}N$  remains weak, but is becoming more organized. Flow across the gulf is commencing in the northern region. The flow near the oil terminals remains weak and southward. The mean flow in April, Figure 23c, sees a continuation of the same trends seen in March. Flows along the Arabian Peninsula and up the Iranian coast have intensified. The intensification and general flow of April makes it the most similar to the mean flow. The main difference between April and the entire mean flow is the central region. In April this region is still unorganized and several eddy-like formations are observed; whereas in the mean flow for the entire period, the central region is well defined and flow primarily along the major axis to the south.

By May, the overall magnitudes of the mean flow has increased significantly (Figure 23d). Although the characteristic southward flow is still observed in May, it is partially hidden by the fact that most of the flow south of  $29.5^{\circ}N$  is in the same general direction and has the same magnitude. It is evident there is still flow up the Iranian coast; however, this flow is now masked by the predominant southerly and across gulf flows.

The mean flow in June is similar to the entire periods mean flow (Figure 23e). The major difference is in the relative strength of the flow. There is a predominant flow up the Iranian coast, across the gulf, and back down along the Arabian Peninsula. Although the magnitude for the entire time period tends to be less than 10 cm/s, the mean for June tends to be at or above that. Flow in the extreme northern region, near the oil terminals, remains low. When examining the mean flow for July, Figure 23f, a predominant flow to the south is observed. A few eddy-like features near the Iranian coast are also observed, but the primary change is in the extreme north. It is here that the flow has started to increase. No longer is there just a weak flow, the currents are now to the south at around 5 cm/s. This is a major change from the near no flow in the previous months.

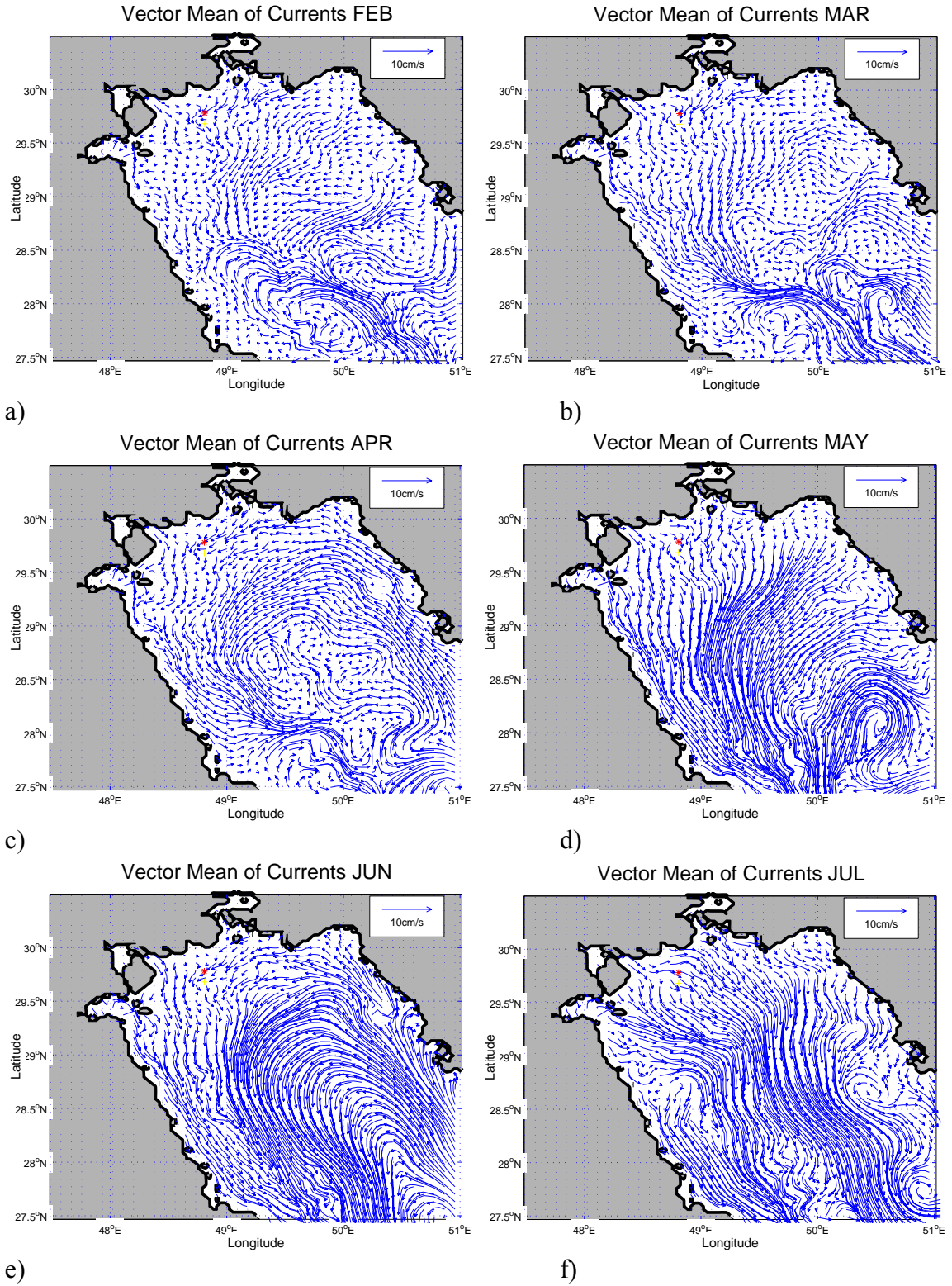


Figure 23. Mean monthly current vectors.

Anomalies were examined over the entire record length and in the form of analyzing the first three EOF modes. As mentioned earlier, to get a better picture of the low energy environment examined in this thesis, EOFs were conducted only in the northern Persian Gulf.

The same method used to calculate percent variance for winds, as illustrated in equation (7.1), was applied to currents. Since the variance was obtained based EOF calculations, there were a finite number of modes that could be derived from the data. The currents data allowed for a total of over 500 modes. The reason for more modes in currents than winds is due to the higher spatial and temporal resolution of the currents. The modes for currents were truncated at 500 for several reasons. The primary reason was at mode500 the percent of the mode one variance was less than one ten thousandth of a percent, and therefore all values thereafter would be negligible. Another less significant reason was processing time. From these calculations it was determined, as illustrated in Table 2 below, that the first 3 modes encompassed 91 % of the variance. By the fourth mode the percent of the total variance has decreased drastically and had less significance.

EOF mode	Percent of Total Variance	Cumulative Percent
First Mode	69.3650	69.3650
Second Mode	16.4190	85.7840
Third Mode	5.3307	91.1147
Fourth Mode	1.6572	92.7719
Fifth Mode	1.1662	93.9381

Table 2. Percent of Variance for the first 5 EOF modes of Current data

Based on the percent variance, the first three EOF modes were analyzed to determine likely forcing. Although these modes were examined, the current field depicted in them is significantly less than what was examined in the mean wind vector discussion. This is due to the fact that EOFs looked at the perturbations. To get an idea of how large of currents the EOFs produce, take the representative vector from Figure 24 and multiply it by the magnitude scale in Figure 25. When this is done for EOF Modes 1, 2, and 3, the scales are shown to be around 100 cm/s, 50 cm/s, and 25 cm/s, respectively.

After examining the magnitudes and directions of EOF-1 (Figure 25), EOF-2 (Figure 27) and EOF-3 (Figure 29), it is apparent that tidal influences are evident throughout the first three modes. Although the magnitudes were of different scales, each have peaks and lulls at approximately the same time periods. On a shorter scale, the maximums are always immediately followed by a minimum. The direction of the first two modes changed primarily by 180 degrees. The two distinct periods found in the magnitudes of the first three EOFs and the directional shift in the first two EOFs indicates there is a strong tidal influence in these modes. Further examination was done to try and determine the other primary influence within the EOFs. If no other major stimulus is observed, further examination of the tidal influences will be discussed. While the tidal influences were readily apparent in all three modes, there is a possible amphidrome located within the area of low energy, Figure 8, which would make it impossible to filter out the tidal influences from the EOFs. An attempt to isolate the tidal influences was made using a low pass filter; however, the influences were still apparent.

EOF-1 has predominantly southwesterly flow (Figure 24). After comparing the magnitudes to the mean wind magnitudes, it was determined that the flow corresponding to EOF-1 has a strong wind-driven component. The direction of flow, Figure 25, was predominantly near 0 degrees and near 180 degrees. When the angle was near 180 degrees, it would slowly decrease from where it started for a period of time, normally decreasing approximately 45 degrees. When comparing the magnitudes and spatial picture of EOF-1 from currents, Figures 24 and 25, to the wind magnitude time series and mean wind vector fields, Figures 21 and 22, as direction correlation can easily be established. When wind magnitudes increase so do the EOF-1 magnitudes. Although the direction is deceiving, the fact that EOF-1 tend to be at 180 degrees when the corresponding magnitudes are maximum, reverses the direction of interest and corresponds to wind-driven currents. The gradual shift of the direction in EOF-1 corresponds to the time lag in the direction due to wind forcing

The mechanism behind EOF-2 is much more apparent (Figures 26 and 27). The period from one angle back to the same angle is around 14 days. It actually varies between 13 and 16 days. The direction cycles between just under 90 degrees to just under

270 degrees. The amplitude has a cyclic maximum on the same time scale as the angle, where a maximum corresponds to a corresponding large angle. When looking at the vector plot of EOF-2, there is a distinct cyclonic flow. All of the previously mentioned factors point towards EOF-2 being tidally driven. As mentioned previously all the modes had a tidal influence; however, EOF-2 appeared to have no other dominating influences.

EOF-3 shows influences from several different factors (Figures 28 and 29). The magnitudes cycle on the same time scale as spring and neap tides. The Direction, however, does not illustrate a dominant tidal influence. In fact there is no dominant cycle established within the direction time series. The vector plot of EOF-3 also does not have a strong tidal influence. However, there are two main areas in this EOF, one on each side of the gulf. The eastern side has a line of convergence running along the Iranian coast; while the western side has a parallel line of divergence. The cause of the convergence and divergence is unknown. However, with the percent variance of EOF-3 equal to around 5% and the magnitude corresponding to a maximum of 25 cm/s this mode has little significance compared to modes 1 and 2. The fact that there is not a single dominating factor and the factors that can be distinguished are accounted for in the previous EOFs and the mean current, further diminish the relevance of this mode. In the end, 85% of the variance was accounted for in the first two modes and some of the influences were established for EOF-3, but determining all of the possible influences for EOF-3 was left for future consideration.

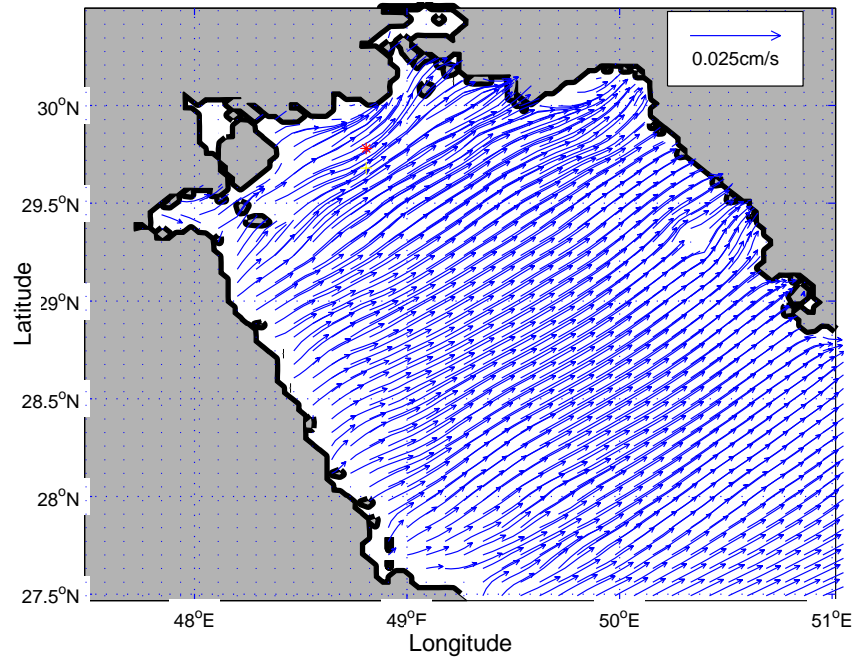


Figure 24. EOF-1 for entire currents dataset in the Northern Persian Gulf.

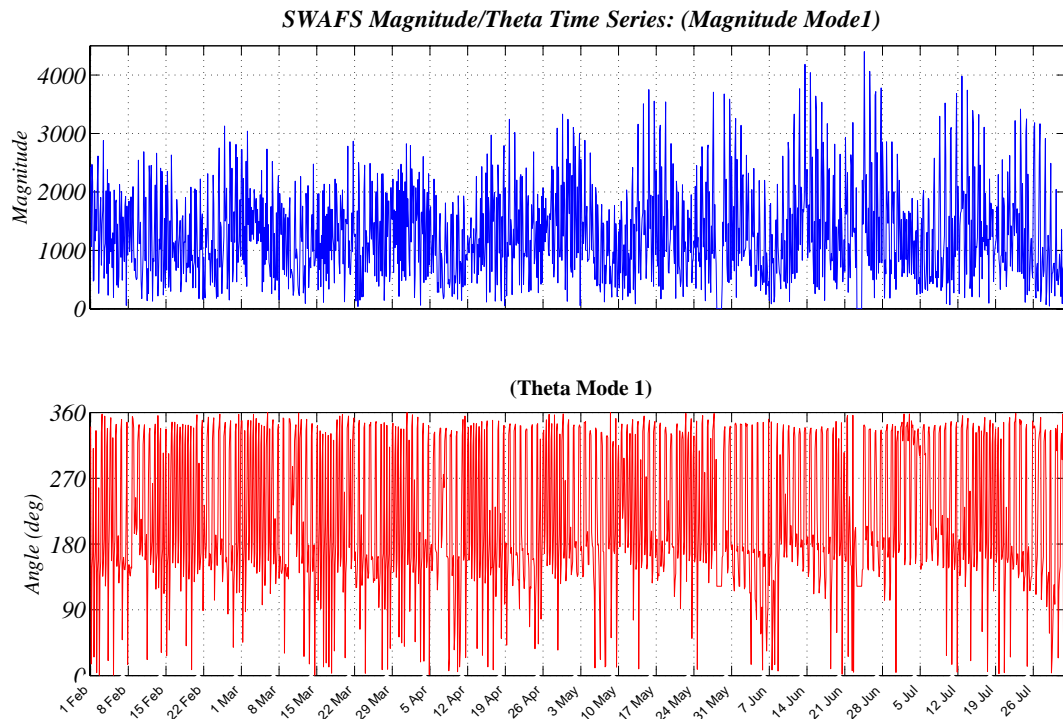


Figure 25. EOF-1 amplitude (top) and direction (bottom) for entire currents dataset in the Northern Persian Gulf.

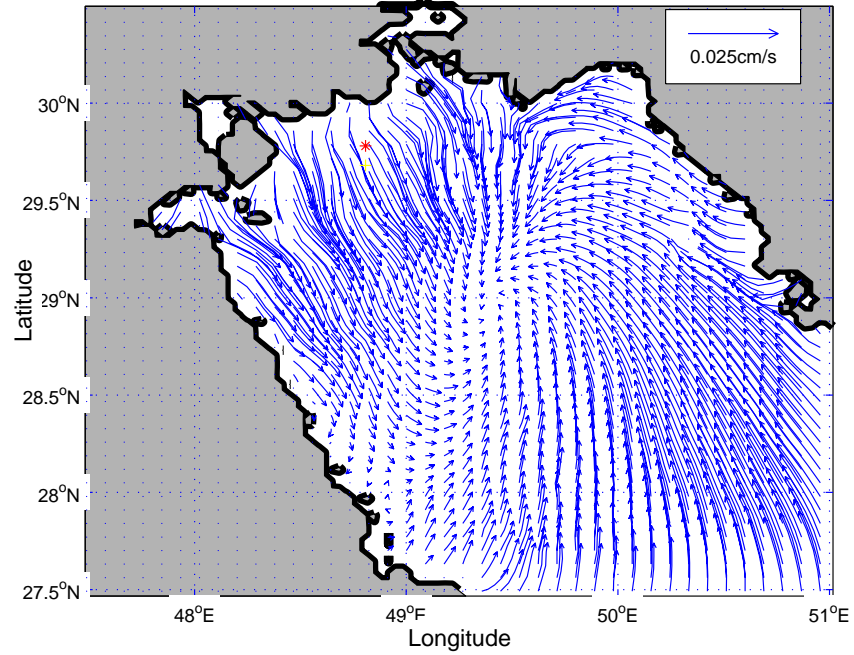


Figure 26. EOF-2 for entire currents dataset in the Northern Persian Gulf.

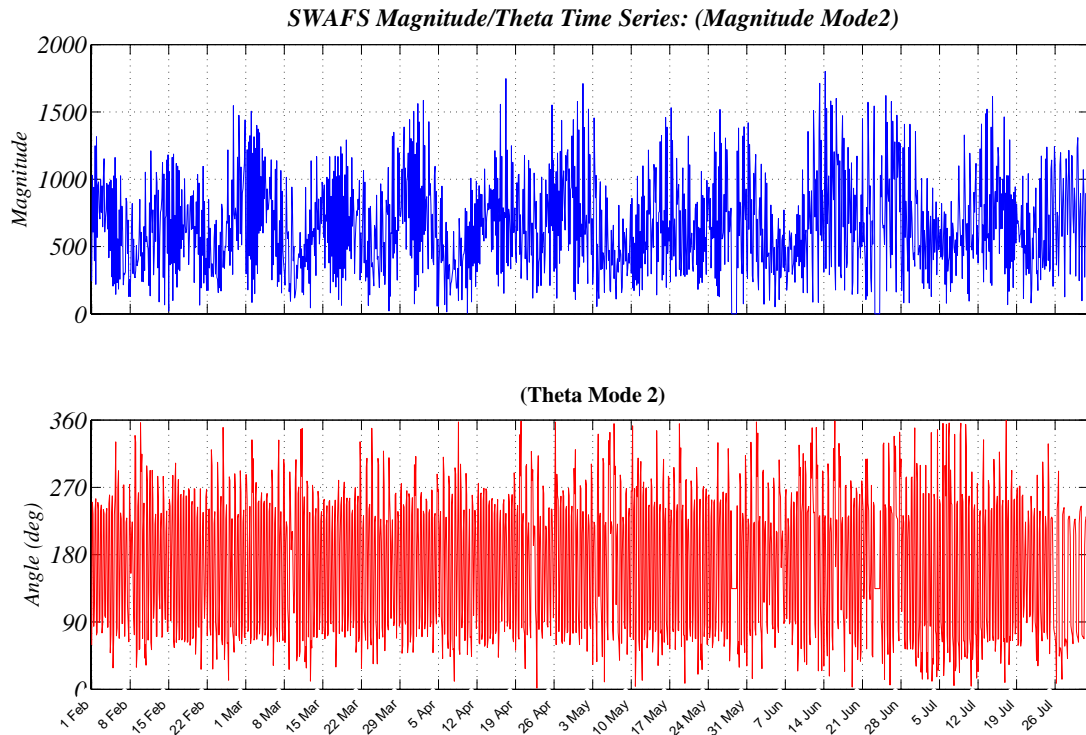


Figure 27. EOF-2 amplitude (top) and direction (bottom) for entire currents dataset in the Northern Persian Gulf.



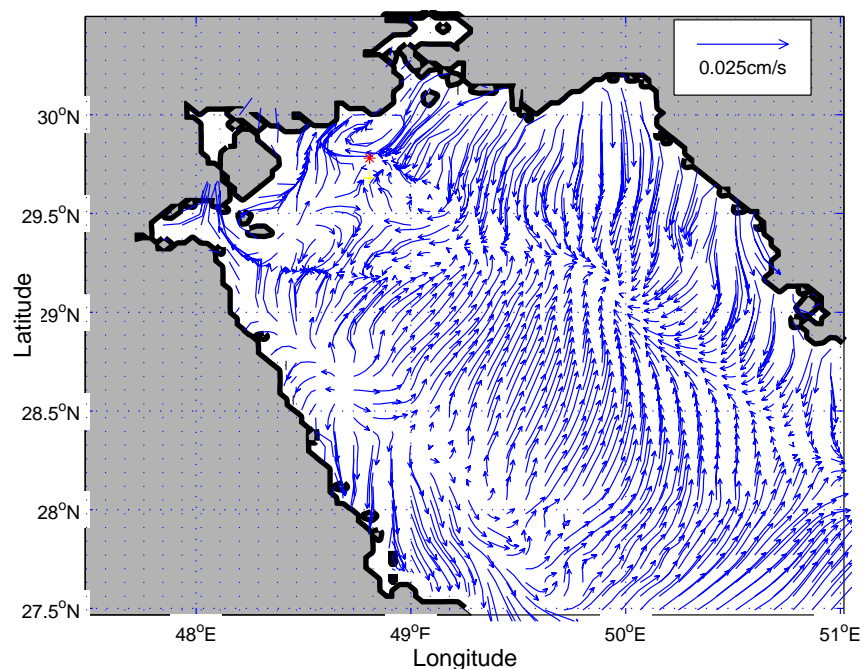


Figure 28. EOF-3 for entire currents dataset in the Northern Persian Gulf.

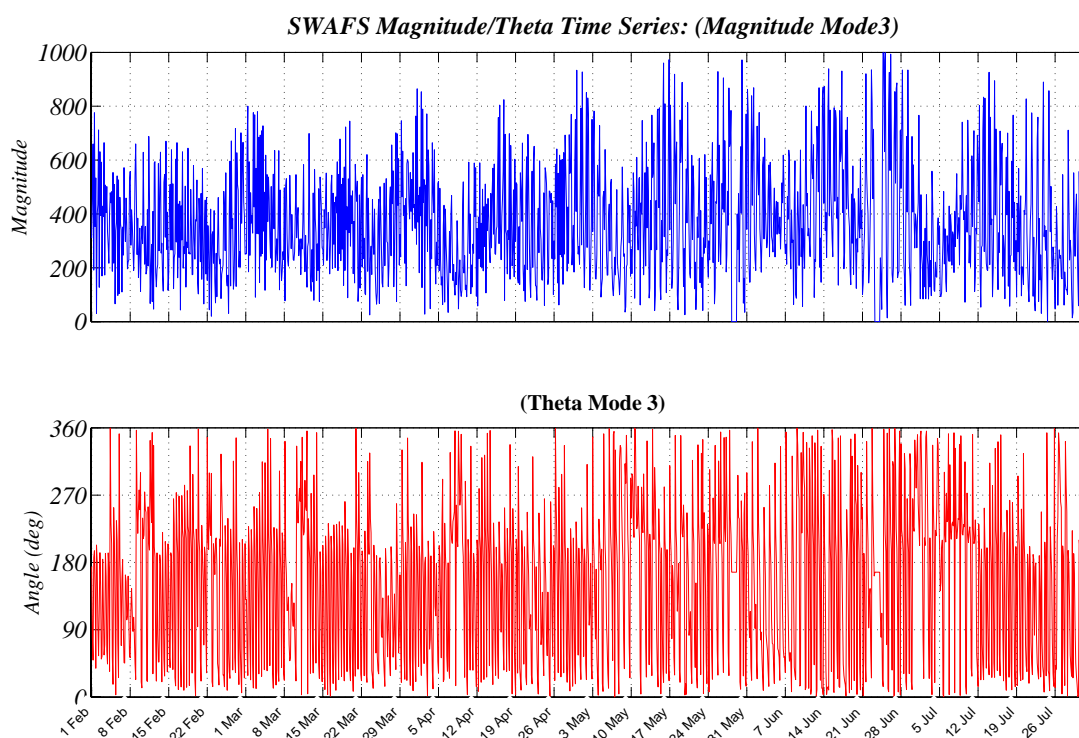


Figure 29. EOF-3 amplitude (top) and direction (bottom) for entire currents dataset in the Northern Persian Gulf.

### **3. Spatial Examining Raw Data**

As discussed in the winds section, when examining a possible oscillating pattern to determine appropriate times to run the models, the mean gives only a partial view. The same logic utilized in examining winds was also used to examine currents. To further examine the currents, looking at the raw data in time series format was beneficial. This was done in two steps. The first step also accomplished goal two. Specifically, the  $U$  and  $V$  components were converted to polar coordinates. This allowed the magnitudes and directions to be analyzed separately. The magnitudes were a significant factor when determining model run times. As discussed in the winds section, some of the criteria for the scenarios included having a: (1) minimal wind and weak current event, (2) maximum wind and weak current event, (3) maximum wind and maximum current event and (4) looking for some period that a weather phenomena occurred. Most of these criteria could easily be seen when looking at a time series of the magnitude of currents (Figure 30) and comparing it to that of winds (Figure 21).

Although when the term maximum current event is used several m/s currents often are thought of, in the low energy region of the northern Persian Gulf this is not the case. A high current event was defined as any event where currents repeatedly exceeded 40 cm/s, with a low current event being one that remained below 25 cm/s. The term repeatedly is used when defining currents due to the cyclic nature of currents. Several periods of maximum currents were found, primarily in late May and through July. Periods of weak currents were found through out the time period, including: (1) the last week in February, (2) the first week in April, and (3) the first week in July.

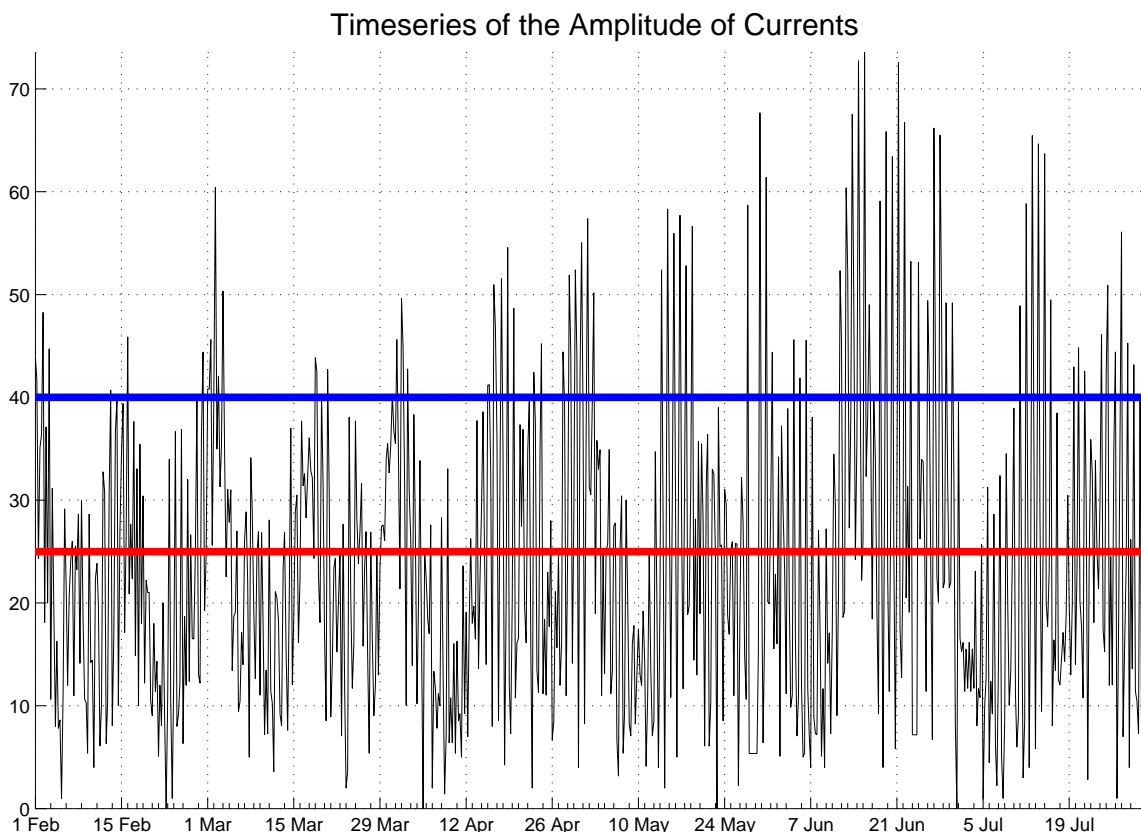


Figure 30. Time Series of the Magnitude of Currents (in cm/s). The red line corresponds to maximum value for the definition of low currents, while the blue line corresponds to the minimum value for high currents, in this thesis.

#### E. EXTRACTING TIMES FOR CHEMICAL MODEL RUNS

Comparing the wind and currents datasets was a relatively straightforward process. This was accomplished by creating a MATLAB file that overlaid the vector wind field over a currents field on a temporal domain of every six hours. An example of this is given in Figure 31. Once this was accomplished, a slideshow was created and run. This allowed a visual inspection of the wind and currents fields. Dates were then extracted that met model scenario criteria. These dates were then compared to the time series created earlier of winds and of currents (Figure 21 and 30). Once the chosen times were confirmed in both the time series analysis and temporal slideshow, model runs were commenced.

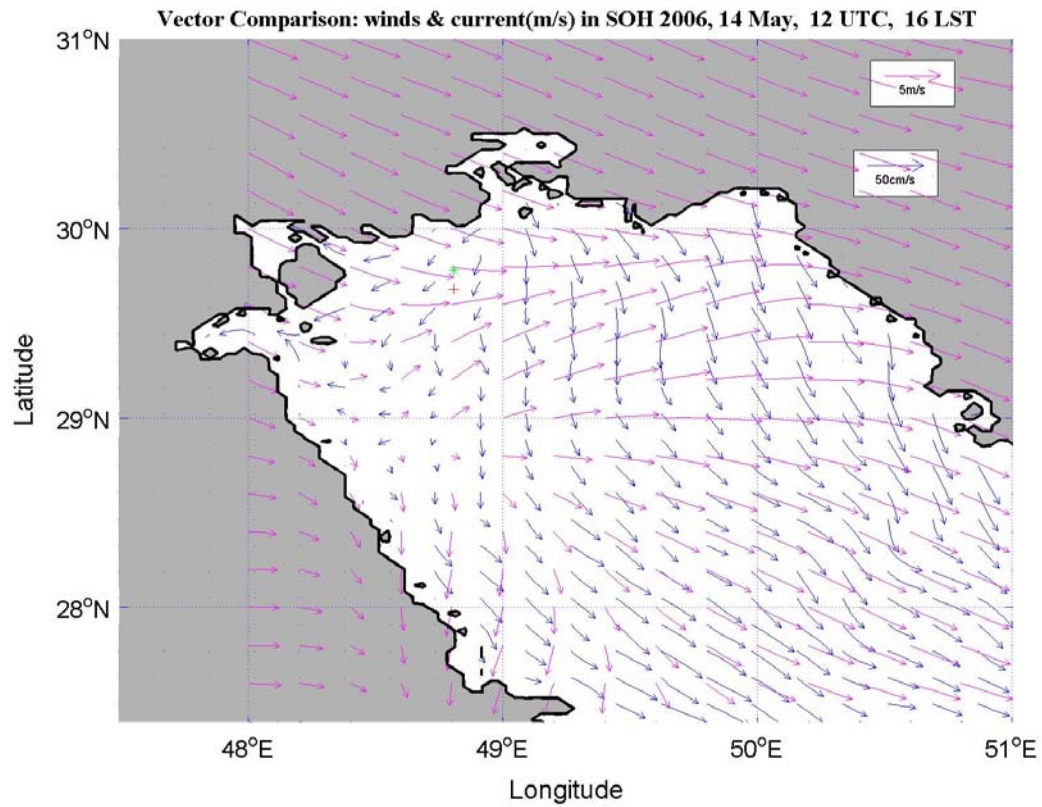


Figure 31. Comparison of Wind and Currents fields from 14 May at 12Z.

## VIII. CONNECTION BETWEEN PHYSICAL AND CHEMICAL MODELS

The process of taking the output of the physical models and using it as an environmental input for the chemical models was long and arduous. This section will detail the process by which COAMPS output was formatted to be ingested into HPAC. It will also describe how SWAFS data was formatted and ingested into CHEMMAP<sup>TM</sup>. Lastly, it will describe the process by which some of the COAMPS data was ingested into CHEMMAP<sup>TM</sup>.

To ingest COAMPS wind fields into HPAC the fields must be converted to a format HPAC recognizes. This process was done in Matlab. To start the process a header that followed the format in Table 3 was created. The lines following this header included the data from COAMPS for the times needed. Several files were made, one for each model runs time, using this technique. These files were then opened using the weather file editor and ingested the new file back into HPAC. The wind was then utilized as a surface wind over the region.

# CREATOR:	UniversalWeatherReader (Chuckles/172.20.69.105)					
# DATE:	2006-10-03 21:02:35 UTC					
# EDITED:	yes					
# REFERENCE:	agl					
# ANALYSIS:	2006	02	01	00.00		
# START:	2006	02	01	00.00		
# END:	2006	02	02	12.00		
# TIMEREERENCE:	utc					
# MODE:	obs all					
SURFACE						
8						
ID	YYYYMMDDHOUR	LAT	LON	Z	WDIR	WSPD
	HOURS	N	E	M	DEG	M/S
-9999						

Table 3. Example of HPAC file header required to ingest data into HPAC from archived COAMPS fields.

Ingesting the data into CHEMMAP was an entirely different problem. After trying to accomplish it by following the same methods to ingest COAMPS into HPAC, it was discovered that it was impossible to do from the Naval Postgraduate School. ASA was very helpful and offered to set-up a file transfer site and configure the datasets to a usable format for CHEMMAP<sup>TM</sup>. This assistance was the only way to get archived data

into the proper format in a timely manner. However, if CHEMMAP<sup>TM</sup> had been run real-time, the data could have been retrieved from the operational models directly, thereby eliminating the configuration problem. Due to time constraints, the winds entire wind field was not able to be converted to a spatially and temporally varying file. However, a time series of a location near Iraq's oil terminals was able to be processed and ingested into CHEMMAP<sup>TM</sup>. Once this field was ingested into CHEMMAP<sup>TM</sup> it was treated as a uniform wind field, thereby providing a wind vector for the entire region.

A drawback to the fields that were obtained via the physical models was in the limited variables archived. Although the chemical models would take more detailed inputs, the fields utilized were at only one depth, or height. There were several other possible inputs into the chemical models that could have been utilized if the fields were available. To fill these values climatology was used. The sea surface temperature (SST) and air temperature were variable in CHEMMAP<sup>TM</sup> that had large impacts on the outcome of the Ammonia and Mustard Gas scenarios. However, climatologic values had to be used. For simplicity, once those values were ingested they remained the same for every scenario. Based on climatology, a SST of 20°C was utilized (Walters and Sjoberg, 1988). In the northern Persian Gulf, SST's are almost always higher than this value, so it allowed for less evaporation than would normally occur.

The amount used in the scenarios was based on fields obtained from HPAC. When calculating the amount of Ammonia to be released in the HPAC, several options were listed, the best being 'industrial transportation. Of those options, the only sea option was a barge that contained Liquid Ammonia. Since Liquid Ammonia is the usual transportation method and the worst case scenario made the best scenario to study, 514 tons of Liquid Ammonia entering the atmosphere and 303 tons being pooled was utilized.

For Mustard Gas the options were less obvious. When articles discussed affects from Mustard Gas, no amounts were used. Since an amount was needed, the same amount used for the Ammonia scenarios were utilized. This would give an extreme example of a spill scenario. This scenario would be more from the aspect of transporting the chemical, rather than an actual chemical attack. This allowed for a larger amount than any chemical attack would ever likely be able to utilize. Although a chemical attack

could be in the form of an airborne attack, those particles would quickly land and the collision scenario would take effect.

The Mine Warfare (MIW) Scenario was relatively easy to design. As will be discussed later, the mines were created to have a 1.0 m diameter and density of  $1.0\text{ g/cm}^3$ . With some simple calculations, it was determined that a 1.0 m diameter mine with density of  $1.0\text{ g/cm}^3$  would equate to approximately a one ton mine. Using the same amount as the previous scenarios allowed for 303 mines to be laid for every scenario.

THIS PAGE INTENTIONALLY LEFT BLANK



## **IX. MIW: IMPACT OF DRIFTING MINES ON OIL PLATFORM OPERATIONS**

To first understand the results, the inputs used in the mine drift scenario have to be examined. The scenario started with a generic iron filings particle in CHEMMAP. The particle was then added to the personal database for modification. To simulate an actual mine the diameter of the particle was enlarged to 1.0 m. Since iron is much denser than water, the density of the particle had to be modified as well. To allow the particle to float on the surface and simulate a possible generic floating mine the density was changed to  $1.0 \text{ g/cm}^3$ . The scenario also included inserting numerous mines running the scenario and then changing location and repeating the process. Times for the model runs were longer for MIW scenarios than for the other scenarios. This was due to the fact that once a mine is placed in the water it does not degrade but remains until it is either hit, washed ashore, or sinks. As such scenarios length of the scenario was based more on operational planning than on anything else.

The primary scenario that was examined was for a newly laid drifting mine. This scenario could be examined in several different ways. Some of these could be: (1) if one mine was placed in the water, where is it likely to travel; (2) if a large amount of mines were placed in the water, where would they go and how much would they spread; and lastly (3) given that a mine is going to be placed in the water, where is the worst case scenario for Iraq's oil terminals, or is there a place that the oil terminals would be affected.

Drifting mine scenarios were run using different locations around the northern Persian Gulf (Figure 32). As can be seen in Figure 33, when the mines were released from locations south of the oil terminals the mines drifted away from them and never affected the oil terminal operations. For the climatological runs, no matter where the mines were placed, they followed the same pattern as will be discussed for the release near the oil terminals. This was primarily due to the nature of climatological forcing. When examining scenarios with COAMPS and SWAFS inputs, the worst case scenarios involved mines originating near the oil terminal. This is because mines the originated

south of the oil terminals frequently never reached the oil terminals and only mines around these terminals would influence operations there. Mines located away from these terminals would influence traffic coming to and from the terminals but not at the terminals.

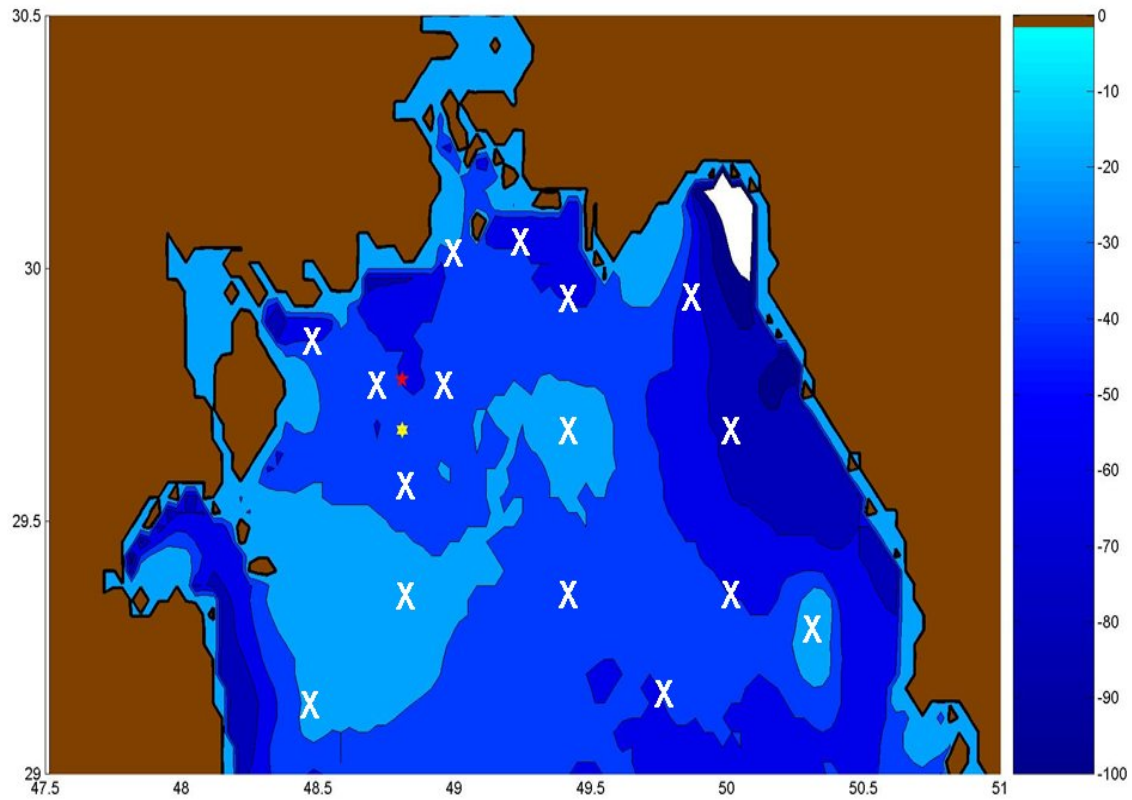


Figure 32. Drop-off points utilized during the drift mine scenario model runs. White X's mark mine drop locations, while the two stars represent oil terminal locations.

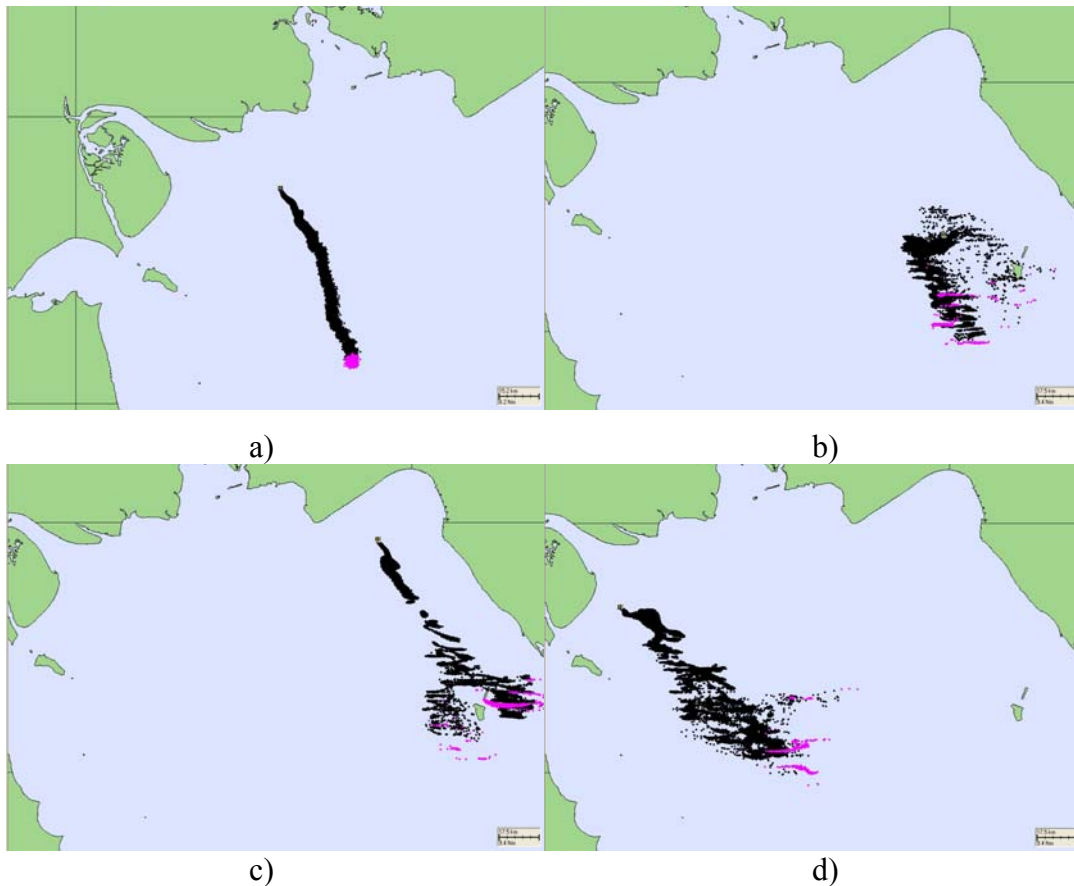


Figure 33. Drifting mine scenario with release from a) climatology and three different release locations (b, c, and d).

#### A. CLIMATOLOGICAL

In the Persian Gulf, as with most of the world, there is no climatological data for currents. To compound matters, there were no current meters readily available to verify the physical model output. Sporadic current observations are usually accomplished during set research studies. Operationally, this presents a problem when in the planning phase. What would the planners' tactics be to account for currents in the Persian Gulf, when none are available? The answer, use what they do know, tides. In all likelihood either a tidal model or a cyclic current would be used as inputs into the chemical models for planning purposes. With this concept in mind, several scenarios were used around the oil terminals and northern Persian Gulf to simulate planning scenarios.

The first scenario utilized a cyclic pattern of 10 cm/s to simulate a tidal pattern. This pattern did what was expected. The mines oscillated around the point where they

were dropped, not really spreading out much. When the climatological wind component, 7 m/s, was added the mines then drifted in a cluster in the direction of the climatological winds (Figure 34,). Of note, the drift would follow the current cycle. There were periods of faster drift with the wind, followed by periods of slower, sometimes even reversing direction, when the current opposed the climatological winds.

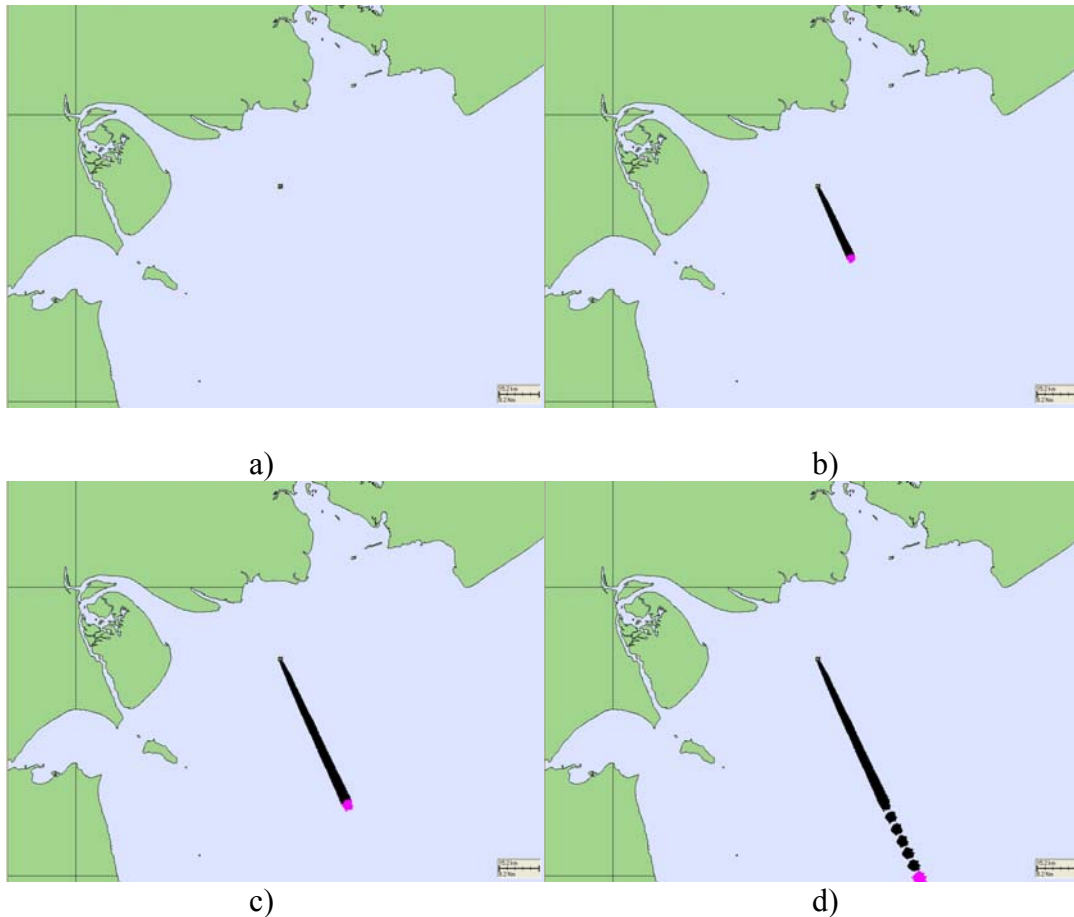


Figure 34. Results from the climatological MIW scenario, which included cyclic currents and climatological winds over a 5 day period. The panels are for a) initialization, b) day 2, c) day 4 and d) day 5.

When the climatological winds were used without any currents, the mines drifted in the direction of the winds. This scenario was done to ensure that winds were indeed a factor on the simulated mines. Although the mines drifted with the climatological winds, they did not travel at the same speed as the winds. The winds input were 7 m/s, whereas the mines drifted much slower than this. In five days time at 7 m/s the mines would have

drifted over 600 km. Since the Persian Gulf is approximately 990 km in length, if the mines were traveling at the same speed as the winds they would have traveled well over half the length of the Persian Gulf. The mines however, had just left the northern region at the end of day five.

## **B. SCENARIO SPECIFIC**

Utilizing modeled data was the next step. Several periods were used for the MIW scenario and subsequent scenarios. These periods were specifically chosen to meet one of the following criteria: (1) minimal wind and weak current event, (2) maximum wind and weak current event, (3) maximum wind and maximum current event and (4) looking for some period that a weather phenomenon occurred. The weak wind and low current period corresponded to 20 through 25 February. All other weak wind periods either did not correspond to any of the currents criteria or was too close to bad or missing data to be utilized. During this event, the chemical model transports the mine much slower than indicated by the climatological runs; however the dispersion is greater (Figure 35). The most likely reason for greater dispersion is the high resolution of currents allowing for more dispersion. With a uniform field in the climatological scenario, regardless of where the mines were placed they felt the same force. Under these conditions, little dispersion would be expected. In February's scenario, the mines felt different currents depending on where they were located. This meant if the starting point was shifted, mines would experience different forcing and therefore could be expected to disperse more. The fact the timeframe examined was a period of low currents, factored in to the amount of dispersion. As the other scenarios will illustrate, the minimal wind and weak current scenario had the least dispersion of all the scenarios. It also had the least movement, as would be expected.

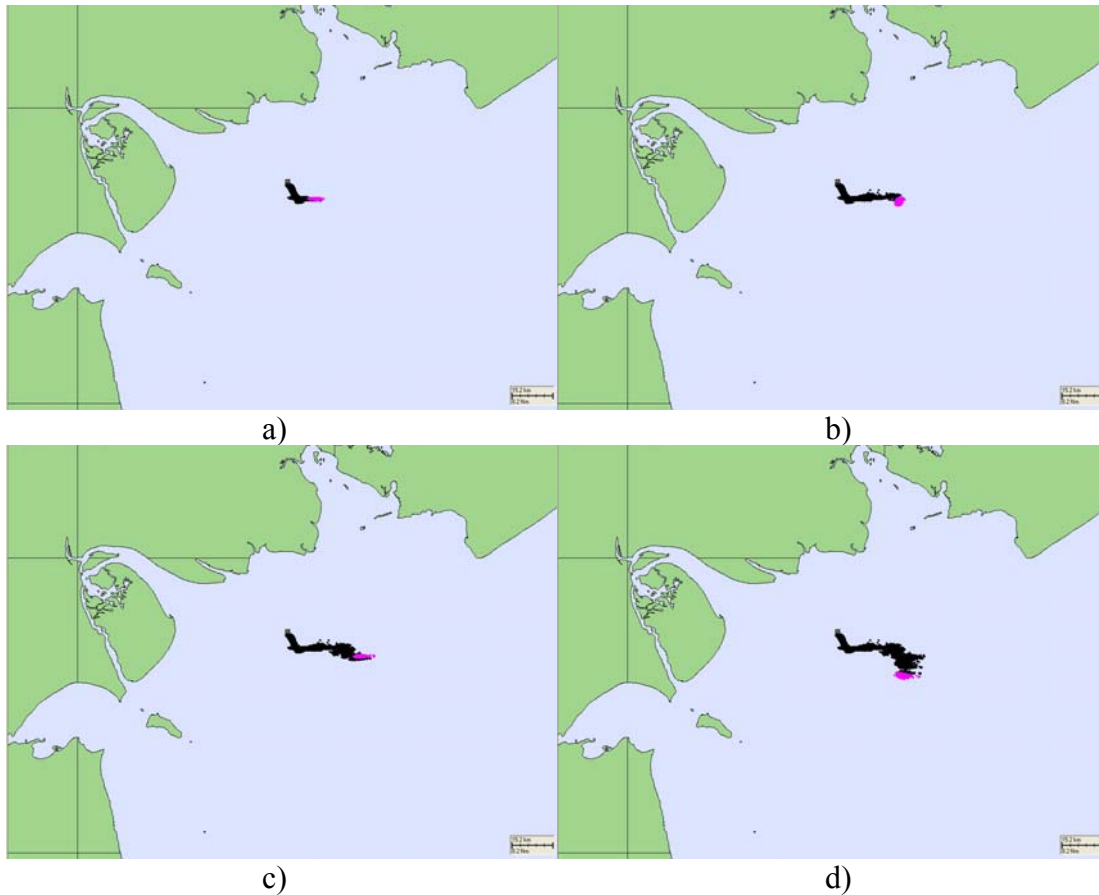


Figure 35. Results from the drifting mine scenario during a weak current and minimal winds event in February 2006. The panels depict elapsed time of a) 2 days, b) 3 days, c) 4 days and d) 5 days. Pink dots are the current location of the mines, while the black dots illustrate track history.

There were two events that met the low currents and maximum winds criteria. The first was from 7 through 12 April. In the April scenario the winds frequently met the high wind criteria, but would also repeatedly decrease below the threshold. The other event occurred between 3 and 10 July. The July event was significant because the winds were the highest seen during the entire period, while the currents continued to stay below the 25 cm/s criteria. What is observed from running the chemical model during these periods was significantly different from the climatological outputs from the previous section. Both periods depicted the mines dispersing further than climatology would suggest. When examining the results from the April scenario, Figure 36, the mines can be seen to disperse more than the climatologic scenario; however they did not travel as far. This is likely due to the winds in the scenario being less than what climatology suggests.

The winds in the July event are closer to the climatological means and traveled much further. The July scenario also saw a large amount of dispersion (Figure 37). Concentrations of mines spread in all direction, yet as the chemical model run progressed an East-West line reformed (Figure 37). The larger wind speeds likely contributed to the increased movement. However the eventual East-West spreading was an unexpected result. All other model runs tended to leave more of a circular or elliptical pattern. A possible reason for the outcome was the length of the run. All other model runs for the drifting mine scenario were for five days, the July event was run for ten days. The output at the five day point, Figure 37 was similar to the other events. A further study utilizing longer runs may be beneficial for operational planning.

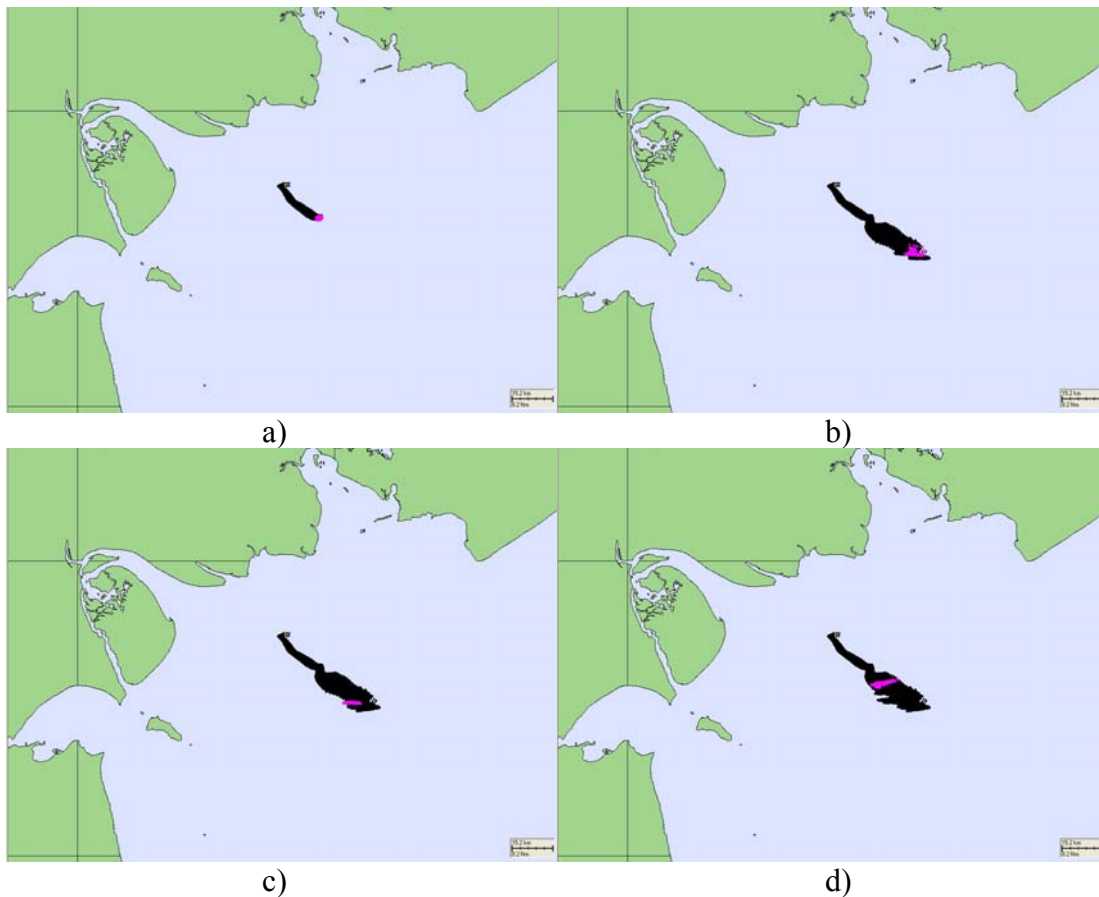


Figure 36. Results from the drifting mine scenario during a weak current and maximum winds event in April 2006. The panels depict elapsed time of a) 1 day, b) 3 days, c) 4 days and d) 5 days.

The criterion for high currents combined with high winds was seen once from 9 until 16 June. Although the high current criterion was met, the currents oscillated direction at high speeds and did not maintain one direction (Figure 38). This led to a shorter distance traveled with the same dispersion seen in the July scenario (Figure 37). This includes forming a line similar to the July event. The main difference is that the line would form, break apart and then reform.

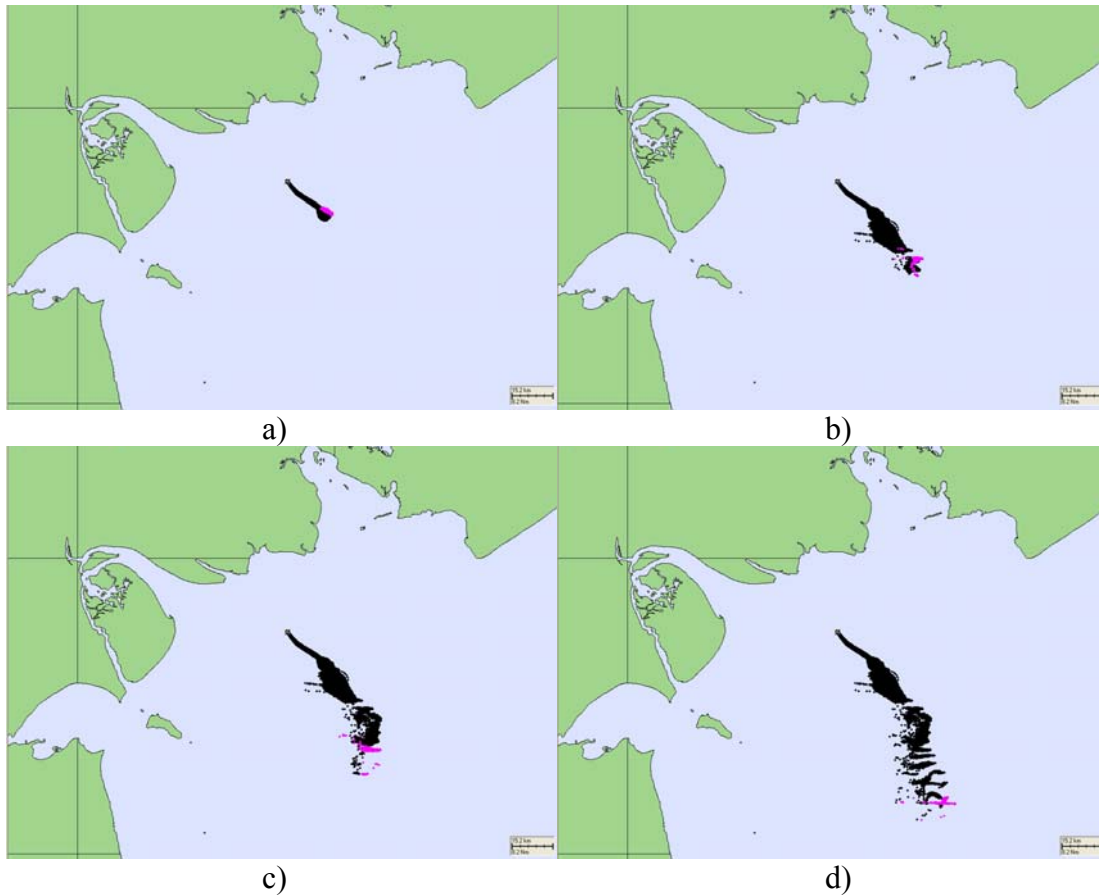


Figure 37. Results from the drifting mine scenario during a weak current and maximum winds event in July 2006. The panels depict elapsed time of a) 1 day, b) 3 days, c) 4 days and d) 5 days.

The primary conclusion from the drifting mine scenario is that regardless of where mines are placed in the northern Persian Gulf they tend to move away from the oil terminals. This fact means that while ships transiting to and from the terminals are affected, those around the terminals would not be affected. This result implies minimal



impact to the actual operation of the oil terminals; however, if ships could not reach the terminals operations would be limited.

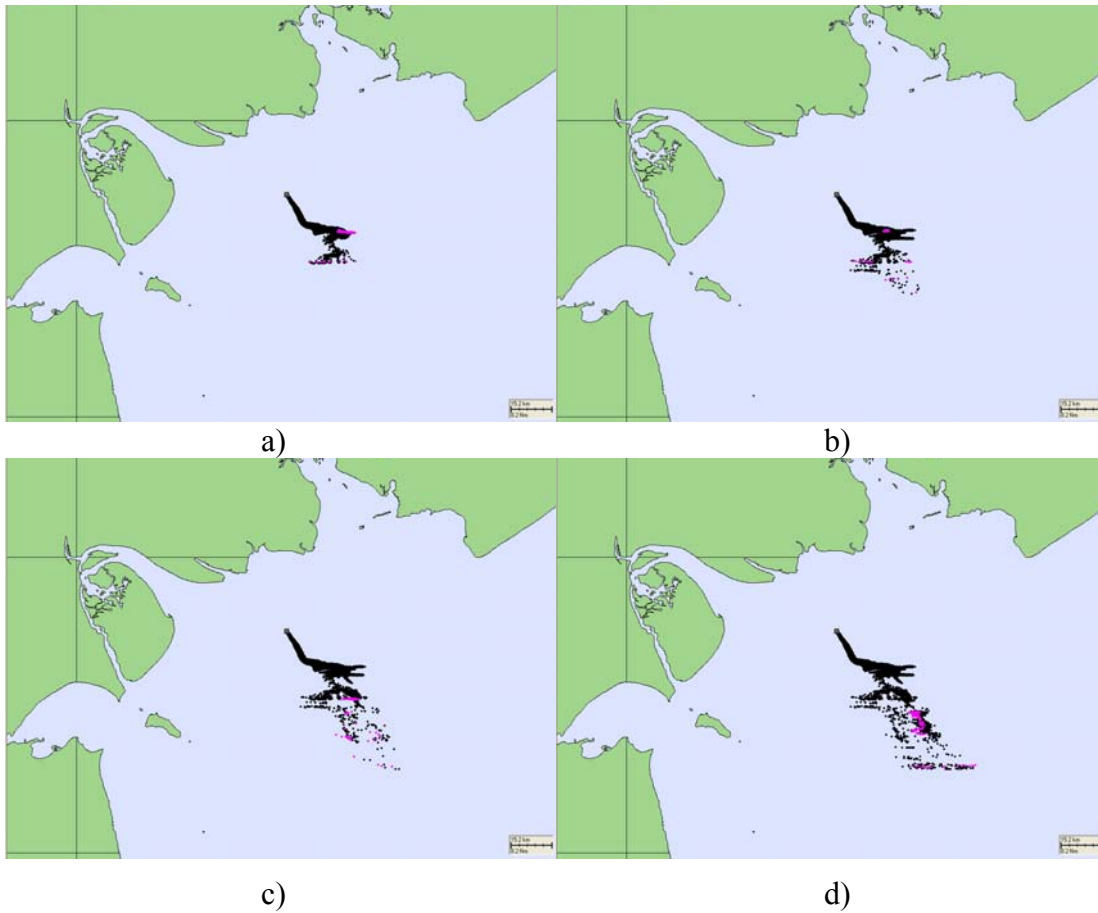


Figure 38. Results from the drifting mine scenario during a strong oscillating current and maximum winds event in June 2006. The panels depict elapsed time of a) 2 days, b) 3 days, c) 4 days and d) 5 days.

THIS PAGE INTENTIONALLY LEFT BLANK

## **X. IMPACT OF A CHEMICAL SPILL TO OPERATIONS: AMMONIA**

The Ammonia scenario included both an atmospheric portion and oceanographic portion. The Atmospheric portion involved running HPAC, while the oceanographic portion involved CHEMMAP<sup>TM</sup>. Although CHEMMAP<sup>TM</sup> contains an atmospheric model, the primary feature examined was oceanographic.

### **A. ATMOSPHERIC PORTION OF SCENARIO**

The atmospheric portion of the Ammonia scenario drove the amounts utilized for the oceanographic portion. Amounts were determined through release type. Since the goal was to look at a worst case, yet realistic, scenario, it was determined that a transportation scenario was the best choice. This option allowed for total damage of a Type 3 Barge carrying Ammonia. The scenario also automatically calculated the amount of the spill that entered the water and the water. The total viable airborne Ammonia was calculated to be 514 tons. Of this amount, 258 tons were in vapor form, while the remaining 257 tons were an aerosol. HPAC also calculated that 303 tons of Ammonia would be pooled in the water. The only changes that could be made to these values were to change the damage amount or the transportation type. Since the scenario was looking at worst case, total damage was most appropriate. With the intent of the scenario to affect Iraq's oil terminals, the only viable option was a waterborne vehicle. Within HPAC this left only a Type 3 Barge. Since the amount within HPAC was extremely rigid, and based on genuine values, the scenario was utilized for the oceanographic portion of the scenario.

#### **1. Climatological**

One of the features imbedded in HPAC is the ability to choose climatology for a given period rather than real-time or archived data. This climatological data allows the user to choose the month and that field is used for the model run. Some problems with this include: (1) what month to choose if the data covers the end of one month and the beginning of the next, and (2) trying to determine the values for the climatological wind field that is being used. The first issue was avoided since the times chosen never overlapped months. This was primarily done to allow currents data to be utilized within

CHEMAP™, however the desired criteria also occurred in such a manner as to avoid this issue altogether. Trying to extract the climatological winds proved futile. Although from the outputs an important conclusion could be made. The climatological winds were constant in both speed and direction.

As with the climatological MIW scenario within CHEMMAP™, all climatological times resulted in the same outcomes. Therefore, only one scenario will be illustrated. This scenario, top half of Figure 39, produced a cone-like dosage duration plume. This plume extended from near the oil terminals along the major axis of the Persian Gulf. Although this plume looks significant, the maximum time for duration was ten minutes. With this in mind, climatology indicated that a chemical spill would rapidly leave the area and transit south. Other methods of looking at the same scenario demonstrated chemical would also spread out quite rapidly. Within a days time the concentration had migrated away from the sight of interest and had spread so that the concentrations were not harmful to humans (lower half of Figure 49).

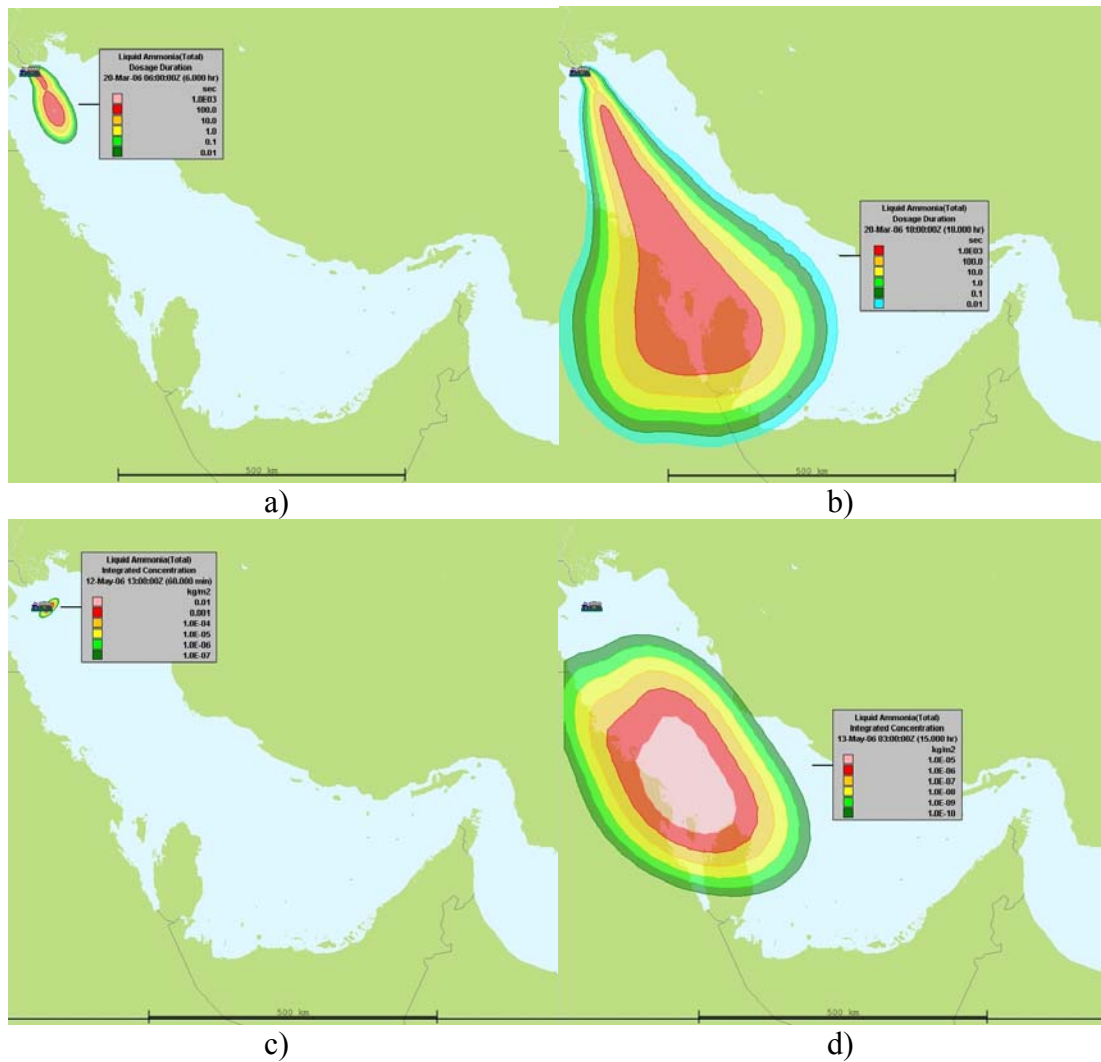


Figure 39. The upper portion depicts a) 50 minutes and b) 15 hours elapsed of 514 tons of Ammonia for the integrate concentration. The lower portion indicates c) 50 minutes and d) 18 hours elapsed for the duration of Ammonia in the atmosphere.

## 2. Specific Scenario

Utilizing modeled data was the next step. The same criteria utilized in the MIW scenario were initially utilized to determine model times periods for the atmospheric portion of the Ammonia scenario. In the end the atmospheric criteria were changed slightly. The criteria now became: (1) relatively constant onshore flow, (2) relatively constant offshore flow, and (3) include an event such as frontal passage in the analysis. Another difference was the timescale. Since the climatological runs demonstrated that Ammonia would leave the zone of interest much faster than in the MIW scenario, a

shorter model run was utilized. Therefore, the model was run over a 24 hour period. This shorter period allowed for more model runs. Since there were not large differences in the results, only the worst case scenario will be shown for each criterion.

Running the model in late March met the criteria of relatively constant onshore flow. The analysis of this criterion also included several times where frontal patterns were observed. These runs included a wind shift from an onshore flow to an alongshore flow. By the time the flow had shifted the scenario was complete, however the criteria for offshore flow would soon be met. A problem encountered when doing this was onshore flow rapidly approached, and left, the archived domain. Once this happened, the fate of the chemical could only be known to have left the modeled region. From Figure 40, it was determined that after 15 hours the majority of the chemical had traveled outside the modeled domain. It was also determined that after the first four hours levels were below threshold limits from ammonia, with possible injury no longer being a factor after two hours.

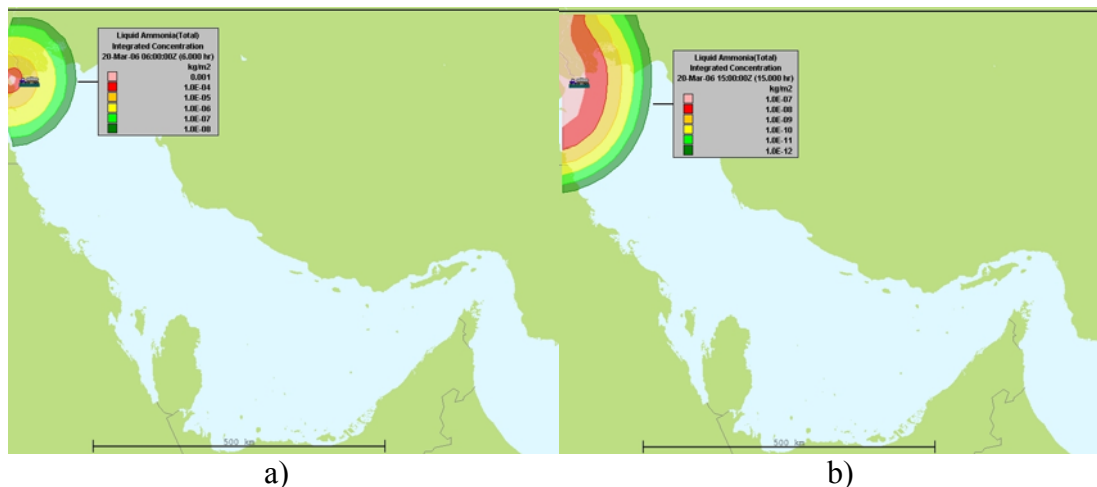


Figure 40. Trajectory of 514 tons of Ammonia at elapsed times of a) 6 hours and b) 15 hours during an onshore winds scenario in March 2006.

The other scenario involved offshore flow. This scenario occurred more often and was more inline with climatology. As seen in Figure 41, the offshore flow rapidly dispersed the chemical throughout the region. This also meant that the toxic levels dropped off almost immediately. From the results of these two scenarios it can be concluded that even a major Ammonia spill will not have very long lasting effects for

humans. Other studies, such as Claereboudt, et al. (2001), have suggested that higher Ammonia levels will drastically affect aquatic life in the region. However, this study focused on operational impacts, which lasted much less than a day.

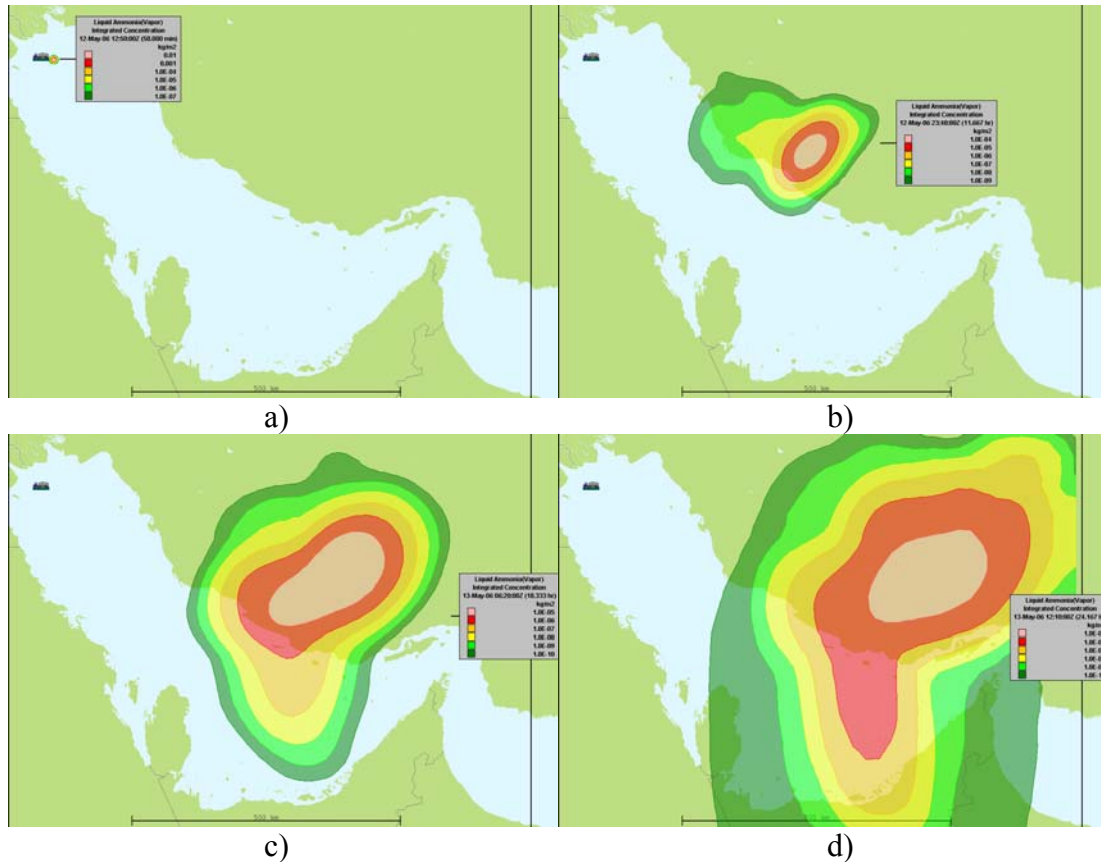


Figure 41. Trajectory of 514 tons of Ammonia at elapsed times of a) 6 hours, b) 12 hours, c) 18 hours and d) 24 hours during an offshore winds scenario in May 2006.

## B. OCEANOGRAPHIC PORTION OF SCENARIO

### 1. Climatological Input

The climatology utilized for the currents is the same as in the MIW scenario. Since no real climatology exists, the climatology utilized was in reference to what planners may consider during the planning phase. Not surprisingly, the results tended to mirror that of the MIW scenario. One of the only differences was in the time scale. Since mines do not degrade or evaporate a longer timescale was used for them, whereas for the Ammonia scenario degradation and evaporation had to be taken into account when running the scenario. After running several climatologically forced scenarios, it was

determined that the Ammonia decayed on the hour time frame, not the day time scale (Figure 42). Running the models for 48 hours produced the best results. After 48 hours the concentration was barely detectable. The scenario also produced a narrow plume that decreased in intensity over time. The climatology scenario moved the Ammonia farther away and in a straight line. This was due to the uniform forcing and lack of variability acknowledged previously in the mine drift scenario.

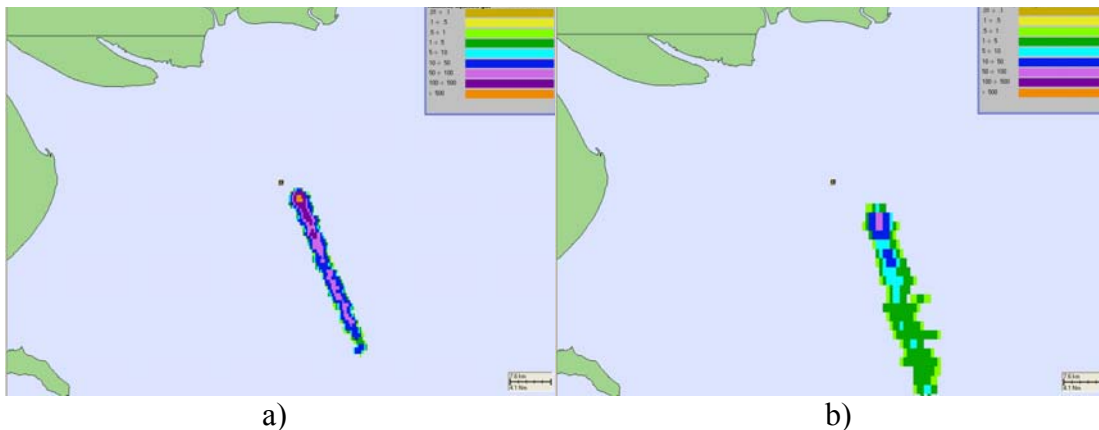


Figure 42. Two panel view depicting a) 24 hours and b) 72 hours elapsed time of Ammonia with climatological forcing.

## 2. Specific Scenario

Utilizing modeled data was the next step. While the climatological scenario was run for each month, the time periods for the archived data utilized the same philosophy as in the MIW scenario. The only difference was the timescale. As discussed earlier in this chapter, the influences of degradation and evaporation had to be taken into account when running the scenario. Furthermore, the time scale should match the runs utilized in the climatology portion. Therefore, 48 hours was used as the primary length. As can be seen in Figure 43, the majority of the liquefied Ammonia evaporated within 3 hours. Whatever did not evaporate quickly spread throughout the water column. The fact that the water column was around 30 m thick allowed this concentration to continually evaporate over the next 12 hours. There was also a small percent of Ammonia that decayed. The concentrations left after 12 hours remained near 10 percent of the total concentration spilled. This amount is the concentration depicted in Figure 44. The figure clearly shows low concentrations in the water and very little flow. The limited movement of Ammonia



was obtained due to currents being primary influence on Ammonia. Since the Ammonia quickly entered the water column, wind had little effect. Although the amount of the spill was designed to be worst a worst case scenario, the impact on the oil terminals were minimal. The fact is that although Ammonia is abundant in the region, alone it does not pose a long term threat to Iraq's oil terminal operations with in the Persian Gulf.

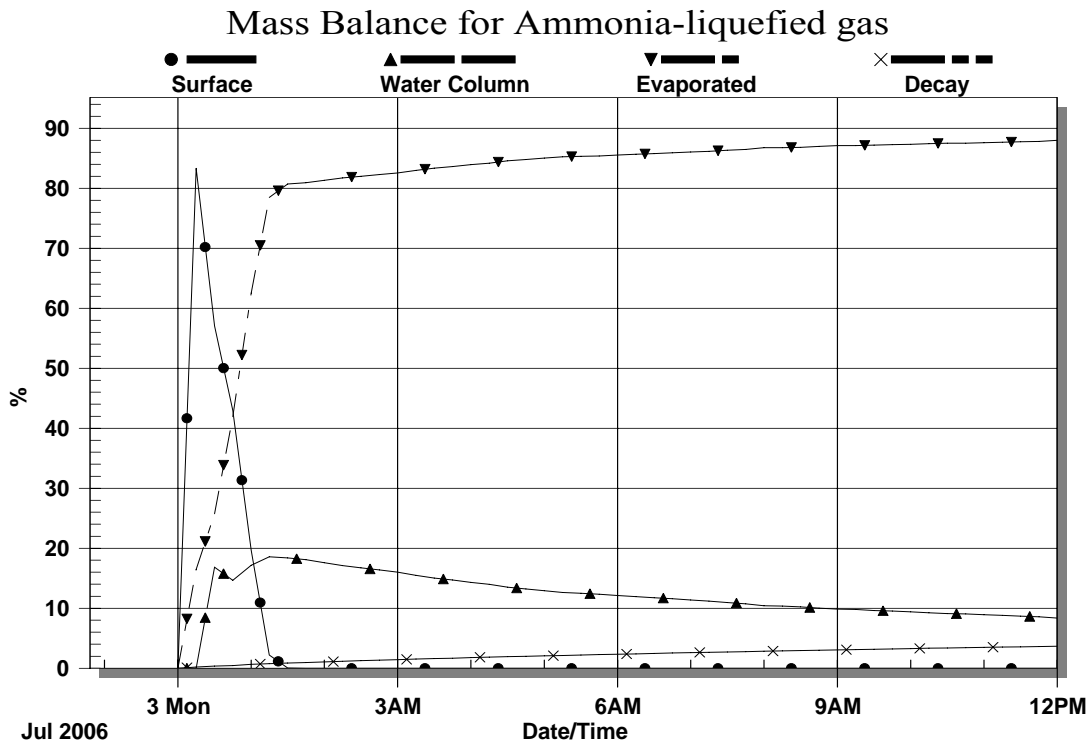


Figure 43. 12 hour mass balance graph of Liquefied Ammonia gas within CHEMMAP™.

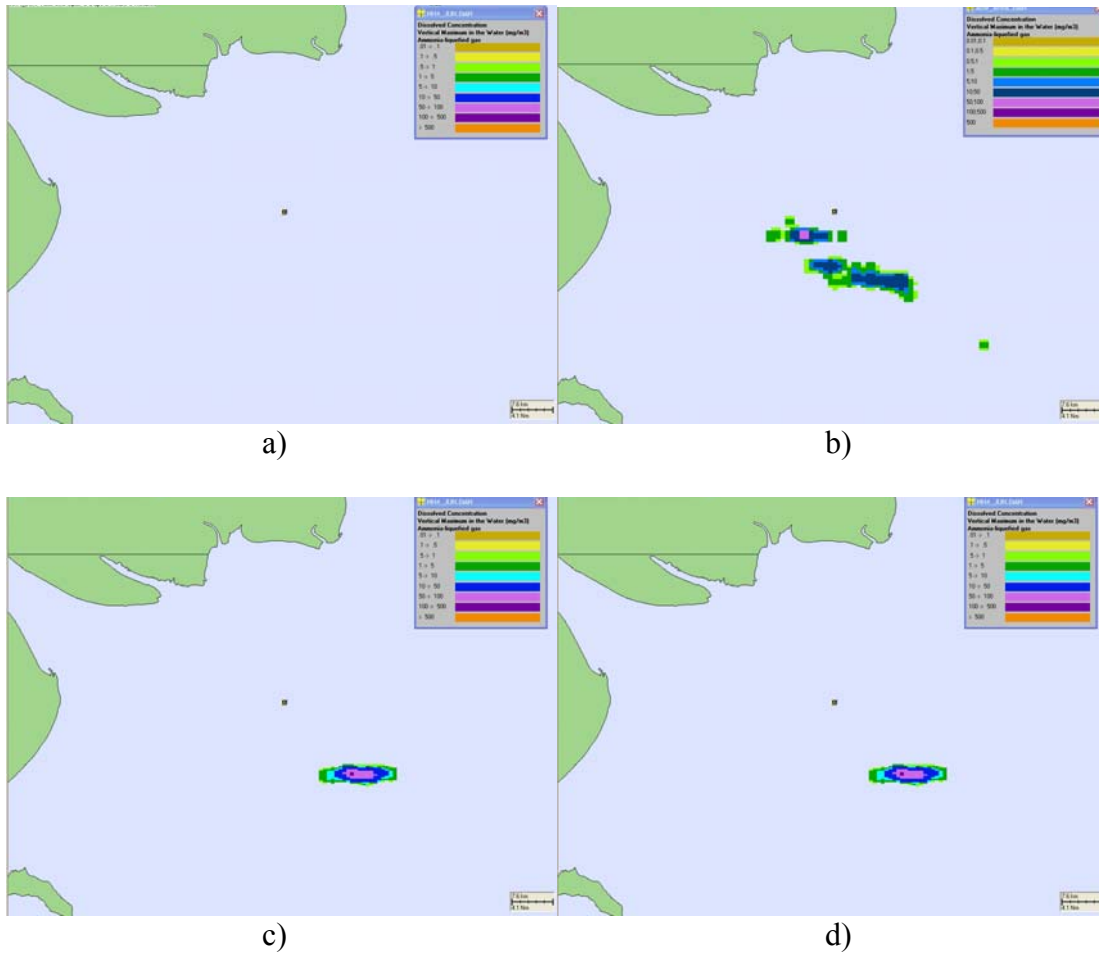


Figure 44. Four panel view depicting a) initialization, b) 72 hours elapsed during April 2006, c) 72 hours elapsed time during June 2006 and d) 72 hours elapsed time during July 2006 for the Ammonia spill scenario. The colorbar units are in  $mg / m^3$ . The labels are as follows: Tan = 0.01-0.1, Yellow = 0.1-0.5, Light Green = 0.5-1.0, Green = 1-5, Light Blue = 5-10, Blue = 10-50, Light Purple = 50-100, Purple = 100-500, and Orange > 500.

## **XI. IMPACT OF A CHEMICAL SPILL TO OPERATIONS: MUSTARD GAS**

The biggest influence in the Mustard Gas scenario was SST. With water temperatures being unavailable from the archived fields, climatological fields had to be used for all scenarios. This meant that no low values, which would have slowed the degradation, were available. It also meant that to get a worst case scenario, values lower than climatology would be used. In CHEMAP<sup>TM</sup>, values for water temperature would be set at 20°C. This value is lower than climatology suggests and therefore would be considered a worst case scenario for evaporation and degradation.

The high SST turned out to be the biggest factor in all Mustard Gas scenarios. Regardless of other inputs, the high SST combined with high air temperatures meant model runs were limited to a maximum of 12 hours (Figure 45). This figure was similar for every model run regardless of meteorological and oceanographic forcing or the time when it was run. To prove that temperature was indeed a major influence, several model runs were conducted using 30°C and 10°C. Although these values are not realistic in the northern Persian Gulf, they were valuable for proving the influence of SST on Mustard Gas duration. As Figure 46 illustrates, the colder temperature decreased the degradation rate and increased the time Mustard Gas remained in the area, whereas Figure 47 demonstrated the opposite effect. From Spectrum Laboratories (2007) and Lloyd (2007) most of the effects from Mustard Gas were from evaporation during World War II. The problem was that the chemical attacks would occur at night and then the chemicals would evaporate during the day. This is less likely to happen in the northern Persian Gulf due to the higher SST's and air temperature. With this in mind and the fact the scenarios run were for a major collision, it can be concluded that the initial impact to a Mustard Gas attack would not effect oil terminal operations longer than two hours. The additional delay would be due to clean-up, removal of injured personnel and bringing new personnel onboard. The additional time for clean-up would be minimal due to the rapid decay seen in Figure 45. The entire time from initial attack to a full operational oil terminal would be measured in hours. Therefore, the result of this study is that utilizing any other data

besides temperature does not have any perceivable value added. This is due to the short duration, which leads to minimal impact from other fields in the environment.

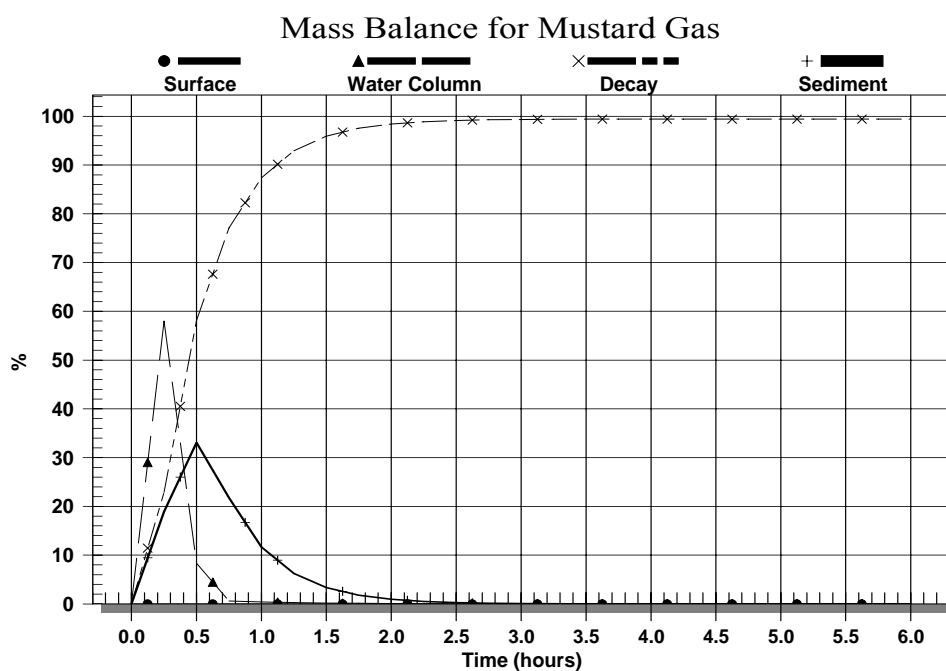


Figure 45. 6 hour mass balance graph of Mustard Gas at 20°C within CHEMMAP™.

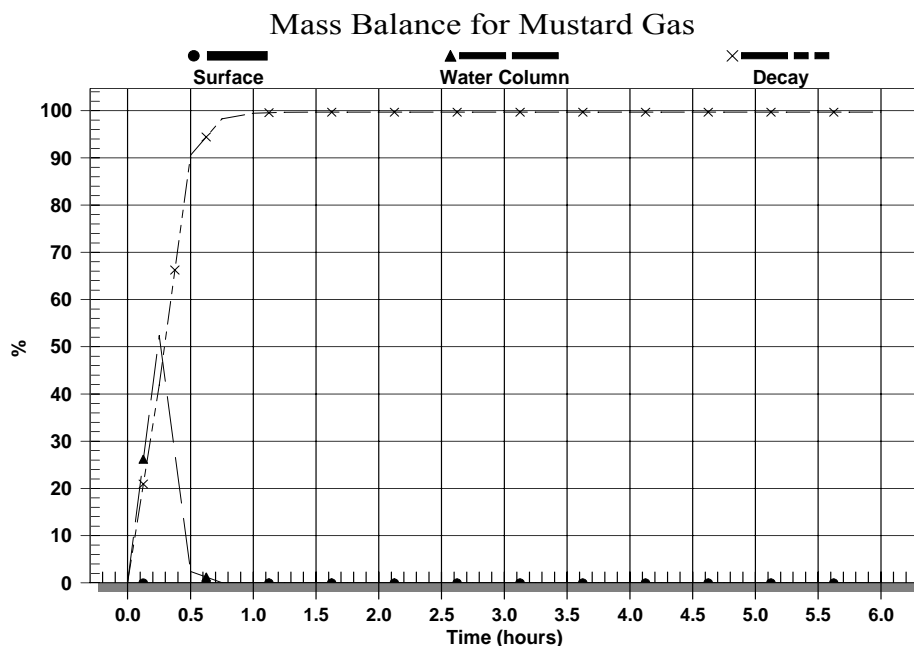


Figure 46. 6 hour mass balance graph of Mustard Gas at 30°C within CHEMMAP™.

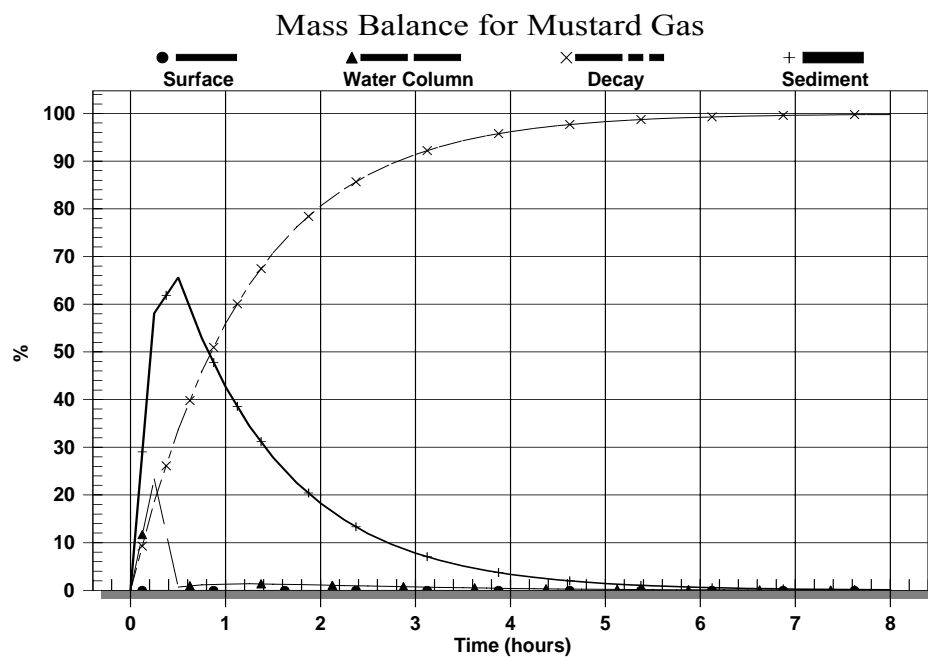


Figure 47. 6 hour mass balance graph of Mustard Gas at 10°C within CHEMMAP™.

THIS PAGE INTENTIONALLY LEFT BLANK

## **XII. SUMMARY**

Starting with six months of surface winds and currents data obtained from COAMPS and SWAFS, an analysis was completed to determine what the value added would be to a drifting mine scenario and two different chemical spill scenarios in the northern Persian Gulf. This region was determined to be a low-energy region. The region's primary wind influences were determined to be the Shamal and transiting low pressure systems. The primary influence of the currents corresponded to wind-driven currents and tides.

The drifting mine scenario included several hundred simulated mines placed in various locations throughout the northern Persian Gulf region. The worst case scenario was determined to be when mines were placed north of the oil terminals or near them. This scenario gave the best chance of mines to affect the oil terminals. If the mines were placed to the south, the current would normally carry them away. The mine scenario had significant value added using any real-time data, as opposed to trying to use climatology. It was also determined that climatological data is not available for currents and that, during a planning phase, either cyclic or tidal currents would be used. These currents did not disperse the mines as much as scenarios involving the archived data. In the end, even if a weak event was utilized, the dispersion was greater than climatological methods, and therefore more realistic.

The Ammonia scenario contained an entirely atmospheric portion as well as an oceanographic portion. This scenario utilized a collision scenario to provide the worst case for an Ammonia spill. The results clearly demonstrated that using real-time, or for this study archived, model data would drastically change the results from using climatological data. In the atmospheric portion, two events demonstrated a large discrepancy between climatology and modeled data. The event most like climatology, the offshore event, produced a greater dispersion of the Ammonia and allowed it to travel much farther as well. The other event had the flow in the opposite direction to climatology. This onshore event occurred primarily when transiting lows came through the area. Although this event produced results drastically different from climatology, the

results were limited by the Ammonia rapidly leaving the modeled area. Operational planners would have to create two scenarios. These two scenarios would cover the worst case events for the period analyzed. These events would be: (1) an offshore event that would quickly spread the Ammonia, and (2) an onshore event.

The other portion of the Ammonia scenario was conducted with in CHEMMAP<sup>TM</sup>. In this scenario the same spill amount was used but the oceanographic portion, the pooled 303 tons, was analyzed. The majority of the liquefied Ammonia evaporated within three hours. Therefore it was determined that Ammonia did not stay in the water long enough to have much of an operational impact, and that aquatic life would be the primary subject effected.

The last scenario analyzed was a chemical spill of Mustard Gas. This event used the same amount as in the Ammonia scenario. Although this amount is much larger than would be used in a chemical attack scenario, it could occur if there was a collision when chemical weapons were being moved. Although 303 tons of Mustard Gas were released, within one to two hours all the chemical had evaporated or decayed. This was due to the high SSTs and air temperatures found in the northern Persian Gulf. These high temperatures were determined to be the limiting factors for Mustard Gas. Since the data collected only included wind fields, no temperature data was available for further analysis. The temperature fields that were used during this study were kept below the climatological means to provide worst case scenarios. Even by using these lower values, there was little impact, beyond the initial strike/collision and those immediately effected, to oil terminal operations. The fact the operations would most likely be able to resume within a couple of hours meant that no value was added by using any wind values, either climatology or modeled.

As regards recommendations for future research, it should be mentioned that the mine drift scenarios utilized CHEMMAP<sup>TM</sup> to generate a generic mine. This mine was 1.0 meters in diameter and had a density of  $1.0 \text{ g/cm}^3$ . Since this size and density was not based on any real data, further study utilizing CHEMMAP<sup>TM</sup> with more realistic



floating mine density and sizes could prove beneficial. If ASA could add a drifting-mine database to CHEMMAP<sup>TM</sup>, the program could be useful for the MIW operations.

If archived temperature fields could be retrieved for the given timeframe, a detailed analysis of those fields could give a better picture of temperature ranges in the northern Persian Gulf. These ranges would assist in determining the exact duration of Mustard Gas and then if there are any impacts on operations.

THIS PAGE INTENTIONALLY LEFT BLANK

## APPENDIX

This appendix contains all relevant figures not referred to in the text.

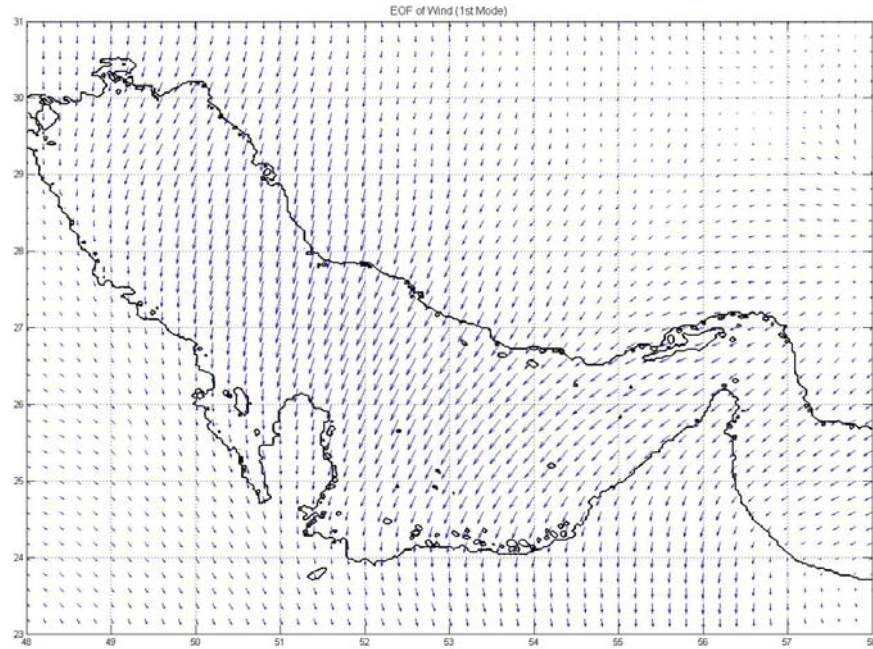


Figure 48. EOF-1 for winds of the entire Persian Gulf.

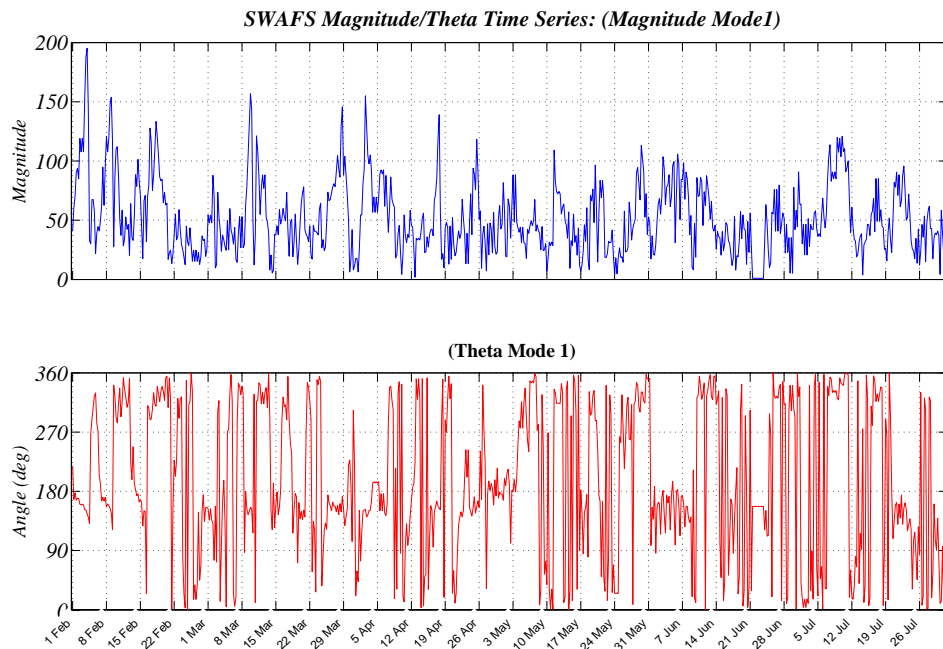


Figure 49. EOF-1 amplitude (top) and direction (bottom) for entire wind dataset in the Persian Gulf.

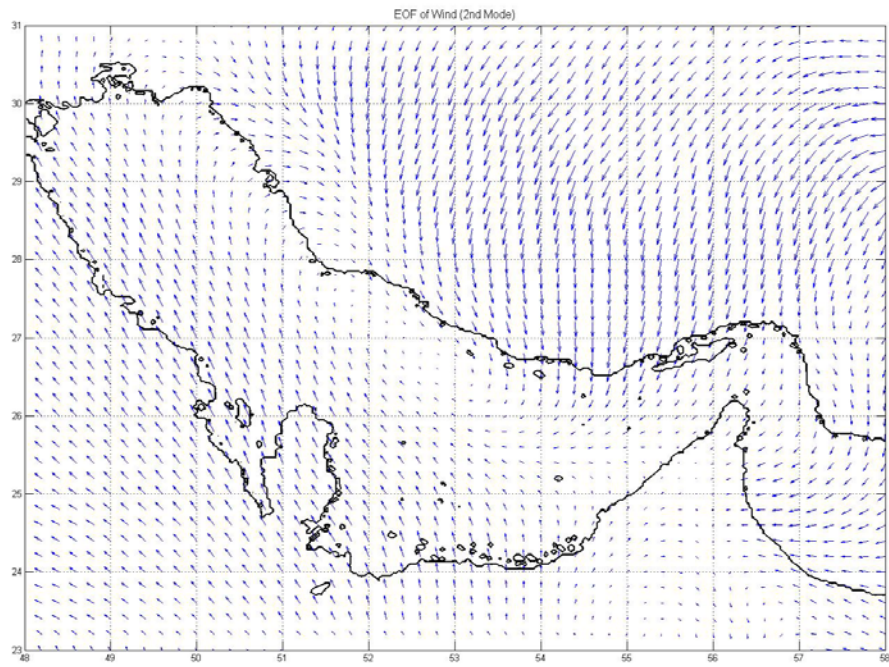


Figure 50. EOF-2 for winds of the entire Persian Gulf.

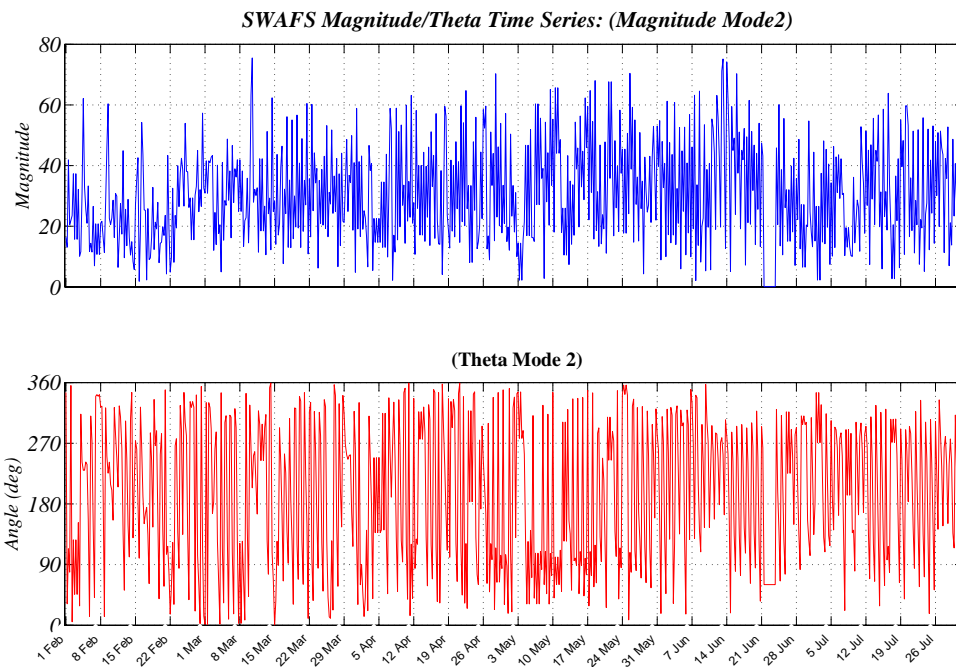


Figure 51. EOF-2 amplitude (top) and direction (bottom) for entire wind dataset in the Persian Gulf.

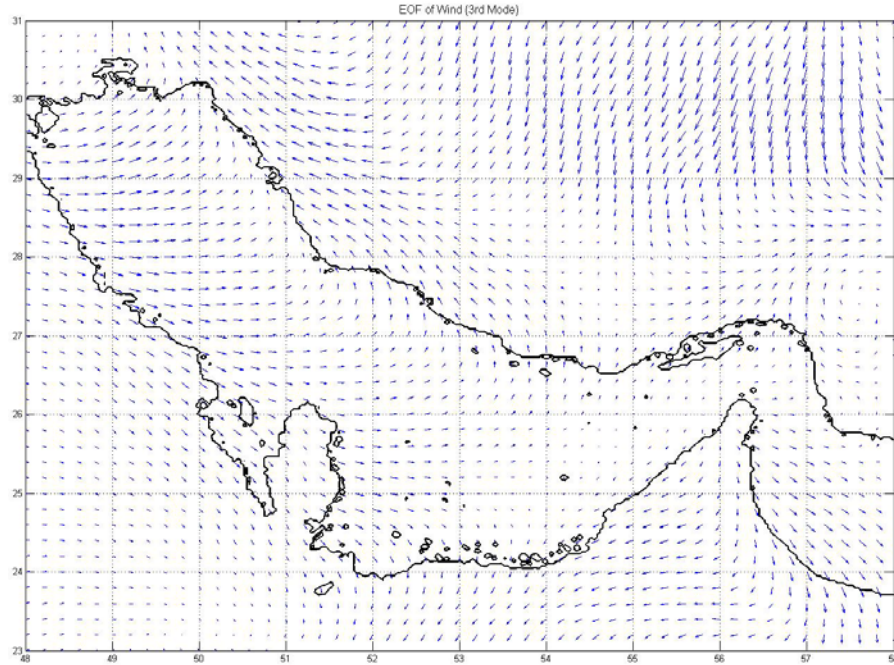


Figure 52. EOF-3 for winds of the entire Persian Gulf.

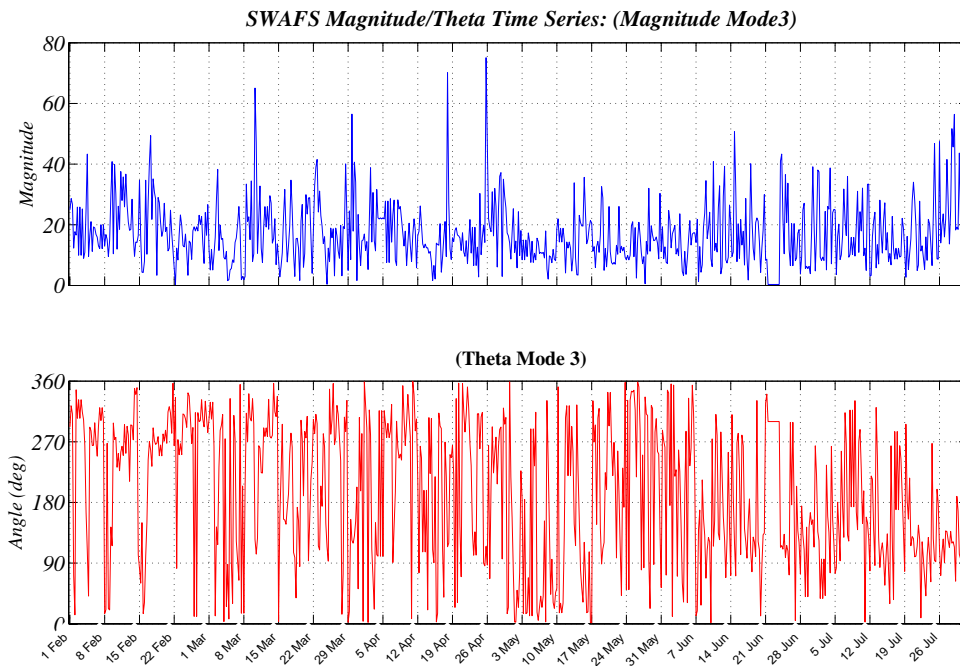


Figure 53. EOF-3 amplitude (top) and direction (bottom) for entire wind dataset in the Persian Gulf.

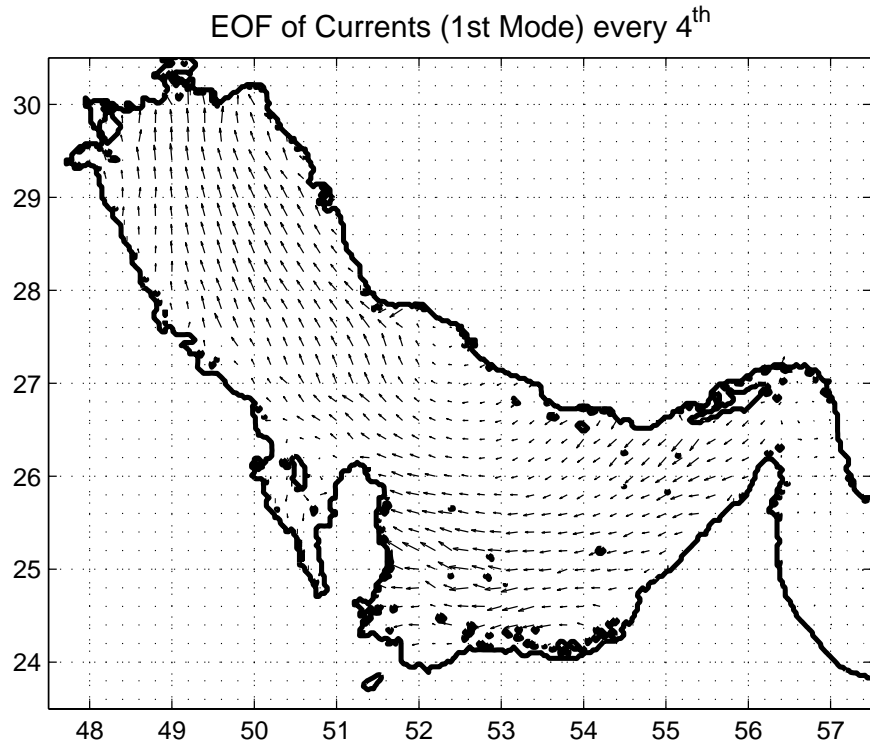


Figure 54. EOF-1 for currents of the entire Persian Gulf. Vectors are every fourth vector of the ones calculated, which equates to every eighth point.

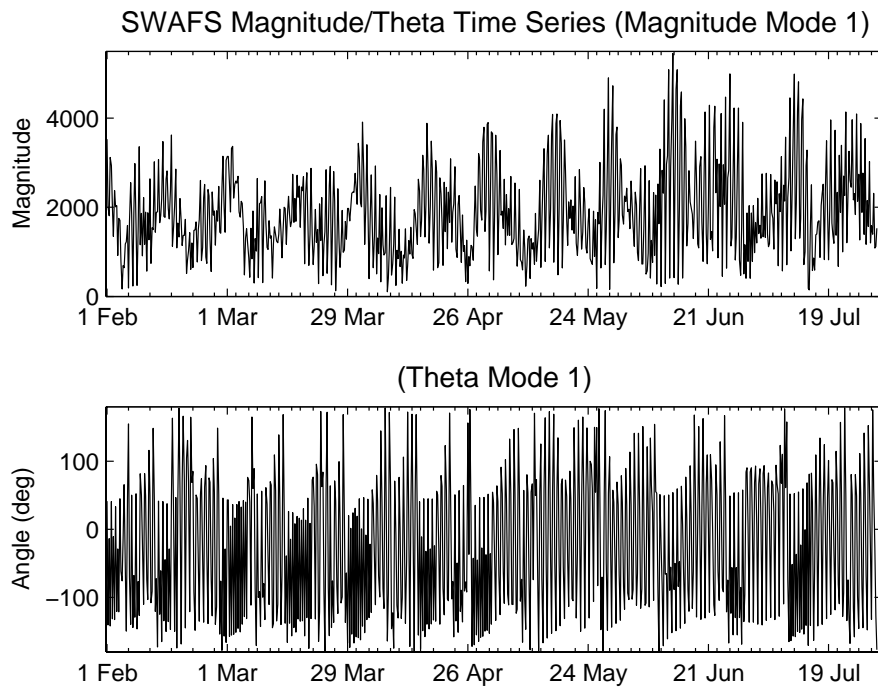


Figure 55. EOF-1 amplitude (top) and direction (bottom) for entire current dataset in the Persian Gulf.

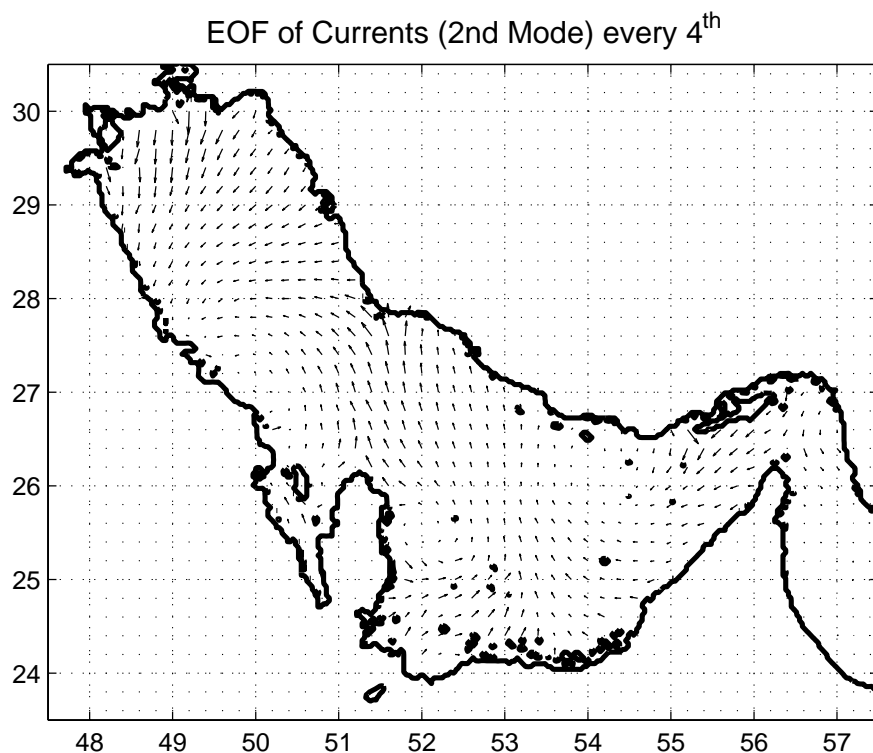


Figure 56. EOF-2 for currents of the entire Persian Gulf. Vectors are every fourth vector of the ones calculated, which equates to every eighth point.

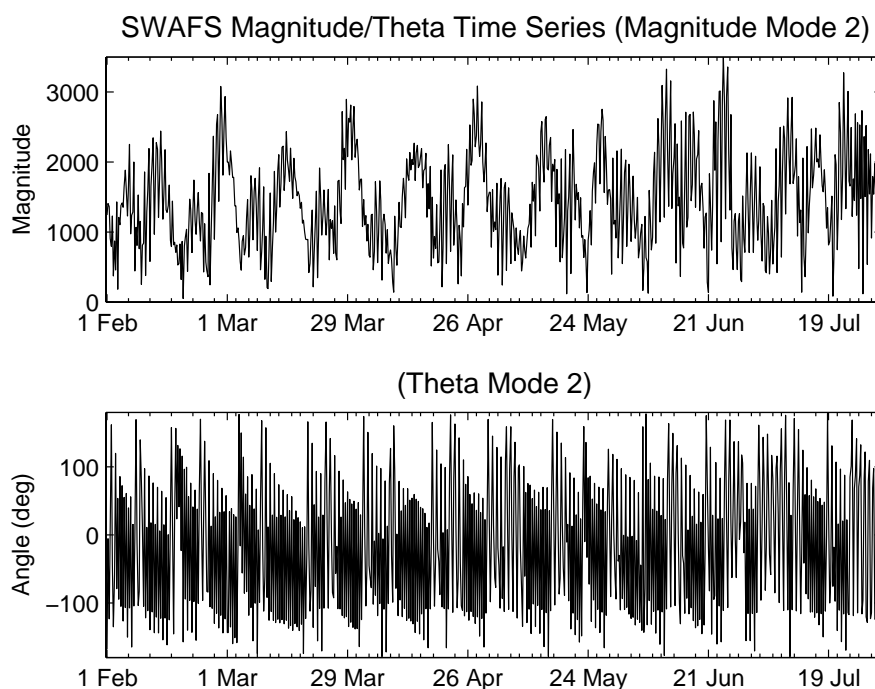


Figure 57. EOF-1 amplitude (top) and direction (bottom) for entire current dataset in the Persian Gulf.

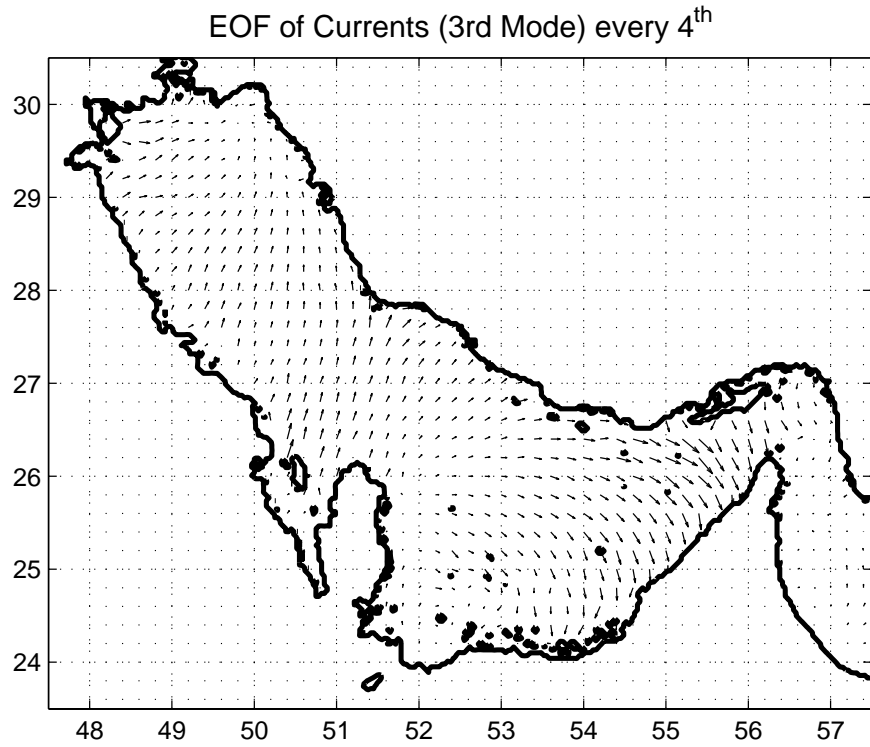


Figure 58. EOF-3 for currents of the entire Persian Gulf. Vectors are every fourth vector of the ones calculated, which equates to every eighth point.

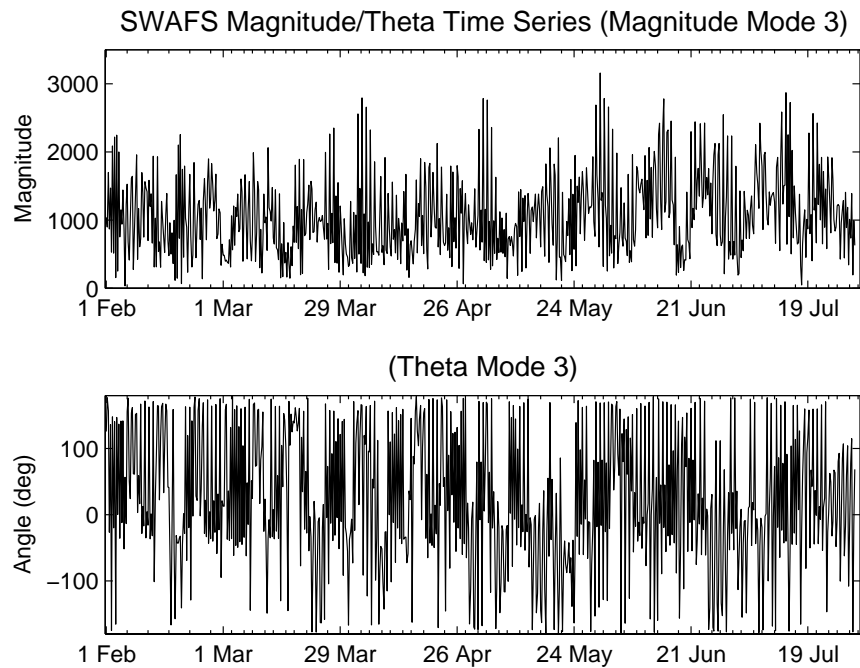


Figure 59. EOF-1 amplitude (top) and direction (bottom) for entire current dataset in the Persian Gulf.



## LIST OF REFERENCES

- Ackerman, S. A. and Cox, S. K, 1982: The Saudi Arabian heat low: Aerosol distribution and thermodynamic structure. *J. Geophys. Res.*, 87, 8991-9002.
- Arakawa, A. and V.R. Lamb, 1977: Computational design of the basic dynamical processes of the UCLA general circulation model. *Methods in Computational Physics*, 17, Academic Press, 173-265.
- Asselin, R.A., 1972: Frequency Filter for Time Integrations. *Mon. Wea. Rev.*, 100, 487-490.
- Baker, N.L., 1994: Quality control of meteorological observations at Fleet Numerical Meteorology and Oceanography Center. *NRL/FR/7531-94-9451*, Available from the Naval Research Laboratory, Monterey, Ca, 93943-5502.
- Baker, N.L., 1992: Quality control for the Navy operational atmospheric database. *Wea. Forecasting*, 7, 250-261.
- Barker, E., 1992: Design of the Navy's Multivariate Optimum Interpolation Analysis System. *Wea. Forecasting*, 7, 220-231.
- Blumberg, A. F., and G. L. Mellor, 1980: A coastal ocean numerical model, in *Mathematical Modelling of Estuarine Physics*. Proc. Int. Symp., Hamburg, Aug. 1978, edited by J. Sunderman and K.-P. Holtz, 203-214, Springer-Verlag, Berlin.
- Blumberg, A.F., and G.L. Mellor, 1987: A description of a three-dimensional coastal ocean circulation model, in *Three-Dimensional Coastal Ocean Models*. Vol. 4, edited by N.Heaps, 208, *American Geophysical Union, Washington, D.C.*
- Chao, S.-Y., T.W. Kao, K.R. Al-Hajri, 1992: A Numerical Investigation of Circulation in the Arabian Gulf. *J. Geophys. Res.*, 97 (C7), 11,219-11,236.
- Chen, S., J. Cummings, J. Doyle, R. Hodur, T. Holtt, C.S. Liou, M. Liu, J. Ridout. J. Schmidt, W. Thompson, A. Mirin, and G. Sugiyama, 2003: COAMPS<sup>TM</sup> version 3 model description - general theory and equations. *Naval Research Laboratory Technical Report, NRL/PU7500-04-448*, 141.
- Chu, P.C., H. C. Tseng, C.P. Chang, and J.M. Chen, 1997a: South China Sea warm pool detected in spring from the Navy's Master Oceanographic Observational Data Set (MOODS). *J. Geophys. Res.*, 102, 15,761-15,771.

- Chu, P.C., S.H. Lu, and Y. Chen, 1997b: Temporal and spatial variabilities of the South China Sea surface temperature anomaly. *J. Geophys. Res.*, 102, 20937-20955.
- Claereboudt, M.R.G., G. Hermosa, T.V. Jamir and E. McLean. 2001: Plausible cause of massive fish kills on the Al-Batinah coast, Sultanate of Oman. In Claereboudt, M.R., Goddard, S. Al-Oufi, H. and McIlwain, J. eds, Proc. *International Conference on Fisheries, Aquaculture and Environment in the NW Indian Ocean*, Sultan Qaboos University, Muscat, Sultanate of Oman.
- Clifford, M., Horton, C., Schmitz, J 1994: SWAFS: Shallow Water Analysis and Forecast System. *IEEE Oceans '94*, Brest, France, IEEE, 82-871994.
- Delvigne, G.A.L. and C.E. Sweeney, 1988: Natural Dispersion of Oil. *Oil and Chemical Pollution* 4: 281-310.
- Donaldson, C. du P, 1973: Atmospheric turbulence and the dispersal of atmospheric pollutants. *AMS Workshop on Micrometeorology*, ed. D. A. Haugen, Science Press, Boston, 313-390 .
- Egan, B. A. and J. R. Mahoney, 1972: Numerical modeling of advection and diffusion of urban area source pollutants. *J. Appl. Met.*, 11, 312-322.
- Evison, D., D. Hinsley, and P. Rice, 2002: Chemical Weapons. *BMJ* 324, 332–335.
- Ezer, T., H. Arango and A. F. Shchepetkin, 2002. Developments in terrain-following ocean models: intercomparison of numerical aspects. *Ocean Modelling*, 4, 249-267.
- Fairall, C.W., E.F. Bradley, D.P. Rogers, J.B. Edson, and G.S. Young, 1996: Bulk parameterization of air-sea fluxes for tropical ocean-global atmospheric coupled-ocean atmospheric response experiment. *J. Geophys. Res.*, 101, 3747-3764.
- Fackrell, J. E. and A. G. Robins, 1982: Concentration fluctuations and fluxes in plumes from a point source in a turbulent boundary layer. *J. Fluid Mech.*, 117, 1-26.
- Fay, J.A., 1971. Physical Processes in the Spread of Oil on a Water Surface. *Proceedings at Joint Conference and Control of Oil Spills*, Washington, D.C., June 15-17.
- French, D., M. Reed, K. Jayko, S. Feng, H.M. Rines, S. Pavignano, T. Isaji, S. Puckett, A. Keller, F. W. French III, D. Gifford, J. McCue, G. Brown, E. MacDonald, J. Quirk, S. Natzke, R. Bishop, M. Welsh, M. Phillips and B.S. Ingram, 1996: The CERCLA type A natural resource damage assessment model for coastal and marine environments (NRDAM/CME). Technical Documentation, Vol.I - V. Final Report, submitted to the Office of Environmental Policy and Compliance, U.S. Dept. of the Interior, Washington, DC, April, 1996, Contract No. 14-0001-91-C-11.

French, D., H. Schuttenberg, T. Isaji, 1999. Probabilities of Oil Exceeding Thresholds of Concern: Examples from an Evaluation for Florida Power and Light. *Proceedings: Proceedings of the 22nd Arctic and Marine Oil Spill Program Technical Seminar*, June 2-4, 1999, Calgary, Alberta, Canada, 243-270.

Fox, D.N., 2000: Confidence Level Assessment of MODAS, Appendix 1: Upgraded Altimetry Processing. NRL Code 7323, July 2000.

Gandin, L.S., 1988. Complex quality control of meteorological observations. *Mon. Wea. Rev.*, 116, 1137-1156.

Goerss, J. and P. Phoebus, 1992: The Navy's Operational Atmospheric Analysis. *Wea. and Forecasting*, 7, 232-249.

Haeger, S.D., 2006: Data Assimilation for Operational Models, PowerPoint Presentation utilized during teleconference at Naval Postgraduate School Monterey, CA. 2 February, 2007.

Hotelling, H, 1933: Analysis of a complex of statistical variables into principal components. *J. Edu. Psych.*, 24, 417-441, 498-520.

Johns, W.E., G.A. Jacobs, J.C. Kindle, S.P. Murray, M. Carron, 1999: Arabian Marginal Seas and Gulfs: *Report of a Workshop held at Stennis Space Center, Miss.* 11-13 May 1999.

Klein, P., 1980: A simulation of the effects of air-sea transfer variability on the structure of the marine upper layers. *J. Phys. Oceanogr.*, 10, 1824-1841.

Klemp, J. and R. Wilhelmson, 1978: The simulation of three-dimensional convective storm dynamics. *J. Atmos. Sci.*, 35, 1070-1096.

Launder, B. E., G. J. Reece and W. Rodi, 1975: Progress in the development of a Reynolds-stress turbulence closure. *J. Fluid Mech.*, 68, 537-566.

Lewellen, W. S., 1977: Use of invariant modeling, *Handbook of Turbulence*. ed. W. Frost and T. H. Moulden, Plenum Press, 237-280.

Lloyd, S., 2005: Mustard Gas - Chemical Warfare Agents. Updated: August 2, 2005, <[http://lungdiseases.about.com/od/chemicalwarfareagents/a/mustard\\_gas.htm](http://lungdiseases.about.com/od/chemicalwarfareagents/a/mustard_gas.htm)> Accessed March 7, 2007.

Louis, J.-F., 1979: A parametric model of vertical eddy fluxes in the atmosphere. *Bound. Layer. Meteor.*, 17, 187-202.

- Martin, P.J., 1985: Simulation of the mixed layer at OWS November and Papa with several models. *J. Geophys. Res.*, 90, 903-916.
- McCay, D.P.F., 2001: Chemical Spill Model (CHEMMAP<sup>TM</sup>) for Forecast/Hindcasts and Environmental Risk Assessment. *Proceedings of the 24<sup>th</sup> Arctic and Marine Oilspill (AMOP) Technical Seminar, Edmonton, Alberta, Canada, June 12-14* Environment Canada, 825-846.
- Mellor, G. L. and H. J. Herring, 1973: A survey of mean turbulent field closure models. *AIAA J.*, 11, 590-599.
- Mellor, G.L., and T. Yamada, 1974: A hierarchy of turbulence closure models for planetary boundary layers. *J. Atmos. Sci.*, 31, 1791-1806.
- Mellor, G.L., and T. Yamada, 1982: Development of a turbulence closure model for geophysical fluid problems. *Rev. Geophys. Space Phys.*, 20, 851-875.
- Mellor, G.L., and A.F. Blumberg, 1985: Modeling vertical and horizontal diffusivities with the sigma coordinate system. *Mon. Wea. Rev.*, 113, 1380-1383.
- Mellor, G. L., T. Ezer and L. Y. Oey, 1994: The pressure gradient conundrum of sigma coordinate ocean models. *J. Atmos. Oceanic. Technol.*, 11, 1126-1134.
- Mellor, G. L., L.-Y. Oey and T. Ezer, 1998: Sigma coordinate gradient errors and the seamount problem. *J. Atmos. Oceanic. Technol.*, 12, 1122-1131.
- Mellor, G. L., 2004: Users Guide for A Three Dimensional, Primitive Equation, Numerical Ocean Model. Princeton University, Princeton, NJ. Web site: <http://www.aos.princeton.edu/WWWPUBLIC/htdocs.pom/> Accessed December 20, 2006
- Oey, L.-Y., G.L. Mellor, and R.I. Hires, 1985a: A three-dimensional simulation of the Hudson- Raritan estuary. Part I: Description of the model and model simulations. *J. Phys. Oceanogr.*, 15, 1676-1692.
- Oey, L.-Y., G.L. Mellor, and R.I. Hires, 1985b: A three-dimensional simulation of the Hudson- Raritan estuary. Part II: Comparison with observation. *J. Phys. Oceanogr.*, 15, 1693-1709.
- Okubo, 1971: Oceanic Diffusion Diagrams. *Deep-Sea Research* 8:789-802.
- Pauley, Patricia M., 2003: Superobbing satellite winds for NAVDAS. *NRL Publication NRF/MR/7530--03-8670*, 102.

- Perrone, Thomas J., 1979: Winter Shamal in the Persian Gulf. Naval Environmental Prediction Research Facility, Monterey, California, August 1979.
- Phillips, N. A., 1957: A coordinate system having some special advantages for numerical forecasting. *J. Meteorol.*, 14, 184-185.
- Reynolds, R.M., 1993: Physical oceanography of the Gulf, Strait of Hormuz, and the Gulf of Oman (Results from the Mt. Mitchell expedition). *Mar. Pollut. Bull.*, 27, 35-59.
- Richman, M.B., 1986: Rotation of principal components. *J. of Climatol.*, 6, 293-235.
- Robert, A.J., 1966: The investigation of a low-order spectral form of the primitive equation models. *J. Meteor. Soc. Japan.*, 44, 237-245.
- Sidell FR, Takafuji ET, David RF, 1998: Textbook of Military Medicine. Part I. Medical Aspects of Chemical and Biological Warfare. Office of the Surgeon General, Walter Reed Army Medical Center, Washington DC, 1998:100±1.
- Skamarock, W.C. and J.B. Klemp, 1992: The Stability of Time-Split Numerical Methods for the Hydrostatic and the Nonhydrostatic Elastic Equations. *Mon. Wea. Rev.*, 120, 2109–2127.
- Sykes, R. I., *et al.*, 2000 : PC-SCIPUFF Version 1.3 Technical Documentation. *Titan Corporation, A.R.A.P. Report No. 725*, December 2000.
- Sykes, R. I., 1984: The variance in time-averaged samples from an intermittent plume. *Atmos. Env.*, 18, 121-123.
- Sykes, R. I., W. S. Lewellen and S. F. Parker, 1984: A turbulent-transport model for concentration fluctuations and fluxes. *J. Fluid Mech.*, 139, 193-218.
- Sykes, R. I., W. S. Lewellen, S. F. Parker and D. S. Henn, 1988: A hierarchy of dynamic plume models incorporating uncertainty, Volume 4: Secondorder Closure Integrated Puff. EPRI, *EPRI EA-6095 Volume 4, Project 1616-28*.
- Sykes, R. I. and D. S. Henn, 1992: An improved moment conservation method for the advection-diffusion equation. *J. Appl. Met.*, 31, 112-118.
- Sykes, R. I., W. S. Lewellen and S. F. Parker, 1986: A Gaussian plume model of atmospheric dispersion based on second-order closure. *J. Clim. & Appl. Met.*, 25, 322-331.
- Sykes, R. I., S. F. Parker, D. S. Henn and W. S. Lewellen, 1993: Numerical simulation of ANATEX tracer data using a turbulence closure model for long-range dispersion. *J. Appl. Met.*, 32, 929-947.

Titley, D.W., 2007: Achieving Battlespace On Demand, PowerPoint Presentation utilized during lecture on Battlespace On Demand at Naval Postgraduate School Monterey, CA. 26 January, 2007.

U.S. Hydrographic Office, 1960: Sailing directions for the Persian Gulf. *HO Publ. 62*, 158, Washington, D.C.

Vidan, A., S. Luria, A. Eisenkraft, A. Hourvitz, 2002: Ocular Injuries Following Sulfur Mustard Exposure: Clinical Characteristics and Treatment. *IMAJ*, 4, 577-578.

Weare, B.C., A.R. Navato, and R.E. Newell, 1976: Empirical orthogonal analysis of Pacific sea surface temperature. *J. Phys. Oceanogr.*, 6, 671-678.

Walters K.R., W.F. Sjoberg, 1988: The Persian Gulf Region: A Climatological Study. USAFETAC/TN-88/002, May 1988.

Youssef, M. and M.L. Spaulding, 1993: Drift Current Under the Action of Wind and Waves. *Proceedings of the 16th Arctic and Marine Oil Spill Program Technical Seminar*, Calgary, Alberta, Canada, 587-615.

Zhu, M., B.W. Atkinson, 2004: Observed and Modelled Climatology of the Land-Sea Breeze Circulation over the Persian Gulf. *Int. J. of Climatol.*, 24, 883-905.

Zwolski, Mark, 1998: History of Mining. *Surface Warfare*, 20-21, May/June 1998.

- 2006: Applied Science Associates (ASA), CHEMMAP™ Version 5.1.40, March 2006, Chemical database.

- 2007: "ammonia: Properties." *The Columbia Electronic Encyclopedia*. © 1994, 2000-2006, on Fact Monster. © 2000–2007 Pearson Education, publishing as Fact Monster. <<http://www.factmonster.com/ce6/sci/A0856597.html>> Accessed 07 Mar. 2007.

- 2007: BP (British Petroleum) Shipping Marine Distance Tables: Ports in End, 31 January 2007 Release, Version 1.0.5.128, <<http://www.atobviaonline.com/public/downloads/PortListC.pdf>>, Accessed 11 February 2007.

- 2005: CHEMMAP™: ASA's Chemical Spill Model System, Technical Manual.

- 2003: Energy Information Administration, International Energy Outlook 2003.

- 2006: Country Analysis Briefs: Iraq. Energy Information Administration, <<http://www.eia.doe.gov/emeu/cabs/Iraq/pdf.pdf>> Accessed 07 March 2007.

- 2007: Mustard Gas: essential data  
<<http://www.cbwinfo.com/Chemical/Blister/HD.shtml>> Accessed 28 February 2007
- 2007: Spectrum Laboratories: Chemical Fact sheet – CAS # 505602,  
<<http://www.speclab.com/compound/c505602.htm> 2007> Accessed 28 February 2007
- *Pub. 172*, 2006: Sailing Directions (Enroute) Red Sea and the Persian Gulf, Eleventh Edition.

THIS PAGE INTENTIONALLY LEFT BLANK



## INITIAL DISTRIBUTION LIST

1. Defense Technical Information  
Center Ft. Belvoir, Virginia
2. Dudley Knox Library  
Naval Postgraduate School  
Monterey, California
3. Mr. Edward Gough  
CNMOC Technical Director  
Stennis Space Center, Mississippi
4. CAPT David W Titley  
CNMOC, COO  
Stennis Space Center, Mississippi
5. CAPT Jim Berdeguez  
CNMOC DOO for ASW/MIW
6. CAPT Robert E. Kiser  
CNMOC DOO Stennis  
Space Center, Mississippi
7. Professor Mary L. Batteen  
Naval Postgraduate School  
Monterey, California
8. Professor Peter C. Chu  
Naval Postgraduate School  
Monterey, California
9. LT Charles Williams  
Naval Postgraduate School  
Monterey, California
10. Mr. Ronald Betsch  
MIW Program Manager  
Naval Oceanographic Office  
Stennis Space Center, Mississippi
11. Mr. Steve Haeger  
Naval Oceanographic Office  
Stennis Space Center, Mississippi

12. Mr. Matthew Ward  
Applied Science Associates, Inc.  
Narragansett, Rhode Island
13. Professor Curtis Collins  
Naval Postgraduate School  
Monterey, California